Photon-Number Resolving by Superconductive Devices

POLITECNICO DI TORINO

SCUOLA DI DOTTORATO

Corso di dottorato in Metrologia: Scienza e Tecnica della Misura – XXIV ciclo

Tesi di Dottorato

Photon-Number Resolving by Superconductive Devices

Lapo Lolli

Tutore
Dr. Mauro Rajteri
Prof. Renato Gonnelli

Coordinatore del corso di dottorato

Prof. Giulio Barbato

Marzo 2012

elegance, an affair of mind.

Summary

Strong interests on optical quantum based metrology, quantum information and particularly in quantum cryptography are continuously growing. The main limitations to the developments in these fields are due to non-ideal devices: both single photon sources and single photon detectors.

In these field of applications, detectors require to be able to resolve the number of photons in a light pulse. Presently state of the art indicates that classical semiconductor light detectors (i.e. avalanche photodiode or single photon avalanche diode) are not able to discriminate the number of photon arriving at the same time. In the meanwhile, superconducting devices have shown the possibility to resolve single photon pulses.

One of the most promising superconducting detectors is the Transition-Edge Sensor (TES): a microcalorimeter that takes advantage of the sharp transition (few millikelvin) from the superconducting to the normal phase; for this reason it is sometimes called Superconductive Phase Thermometer (SPT). In the ultraviolet (UV) to infrared (IR) wavelength range, the photons are absorbed directly by the superconductive thin film and the absorbed energy induces an increase of the TES resistance. Thanks to the applied bias voltage, which maintains the device in the transition region the photon absorption induces a decrease of the TES current, measured by a dc-SQUID amplifier, and the pulse integral of the bias power reduction corresponds to the absorbed energy. This means that TESs have the very interesting properties to be able to detect single photons with an intrinsic energy resolution, without filters or gratings, that limit the quantum efficiency. By contrary of classical detectors, if monochromatic light irradiates TESs, as usually happens in communication systems, they show the photon-number resolving (PNR) capability and due to the good signal to noise ratio TESs are almost free from dark counts. Moreover, in the superconducting detector family, TESs are the only true photon-number resolving detectors operating in the VIS-NIR range.

Together with quantum information science, the PNR property results useful even for optical radiometry too. In the optical community, the candela – the International System (SI) unit for the luminous intensity – has not a common consensus whether its present definition fully satisfies the current and future needs of growing

associated technology. Furthermore, actually there are substantial efforts directed toward a new definitions of four base SI units: the proposal wants to link the SI units to fundamental constants, leaving f.i. material artifact.

Considering the recent advances in optical radiometry and in quantum technologies, for the candela world it means redefine its unit linking to the Planck constant and consequently expressing the luminous intensity unit in terms of photon number rather than optical power.

This challenge has been accepted by several national metrology institutes to demonstrate the feasibility of redefining the candela. Inside this research project called 'qu-candela', the TES PNR capability has been considered to build the bridge between the quantum and classical world of radiometry: i.e. the detector possibility to measure optical powers from one single photon per second to the lower limits of cryogenic radiometry, 10^4 photons per second.

The theme of this work of thesis is to investigate both optical and electrical characterization of different kind of TESs based on a titanium/gold multilayer film, produced and developed at the National Institute of Metrological Research (INRIM) of Torino.

Thanks to the proximity effect, the multilayer allows to lower with continuity the critical temperature from that of the Ti bulk ($T_c \simeq 390$ mK) to those of interest: ~ 300 mK and ~ 100 mK.
Detectors with higher T_c have shown a faster response pulse with a relaxing time constant of the order of 200 ns, while for the lower T_c sensors, the time constant is about 10 μs.

By contrary to the response time, the detector intrinsic energy resolution is proportional to its film critical temperature. Our sensors work to discriminate incident photon from UV wavelengths to those typical of the telecommunications, 1310 nm and 1550 nm. Irradiating a TES with an active area of 10×10 μm^2 by incident photons of 0.79 eV (corresponds to a wavelength 1570 nm), the best energy resolution obtained has been 0.18 eV.

Detectors with higher active area 20×20 μm^2 have a worse energy resolution, because it is also proportional to the material film heat capacity. In the meanwhile due to the same reason these kind of sensors present a bigger saturation energy. This has allowed to investigate on the TES capability to discriminate up to 29 incident photons simultaneously. Until now, such count represents the bigger amount of photons discriminated by single photon detectors, without reaching the device saturation, with a linear behavior. From this count it has been estimated 12 photons on average, per pulse, at 9 kHz repetition rate; this results in a photon flux of about 10^5 photons/s, demonstrating the possibility of having a detector able to work from low flux regime to 1 photon/s to flux measurable by conventional semiconductor device (f.i. single photon avalanche detector SPAD).

An innovative absolute calibration technique for PNR detector has been demonstrated. The absolute technique is based on the Klyshko's efficient solution to measure detection efficiency in photon counting rate and well know for common click-no-click detector. In fact, exploiting the recent developments in quantum state world, it is possible to work with quasi single photon state, by using a parametric down conversion heralded single photon source, and calibrate PNR detectors without requiring reference standards.
The best detection efficiency, of ca. 50%, has been reached by coupling the smaller active area detectors with a 9 μm core optical fiber, single mode at telecom wavelengths.

Acknowledgements

I would like to thank:

- √ Dr. M. Rajteri as my Ph. D. supervisor at the *Instituto Nazionale di Ricerca Metrologica* (INRIM) and also Dr. E. Monticone for their scientific support during these three years.
- √ Prof. R. Gonnelli as my Ph. D. supervisor at *Dipartimento di Scienza Applicata e Tecnologia* of *Politecnico di Torino*.
- √ Dr. E. Taralli of INRIM who has spent many hours working with me; Dr. C. Portesi and F. Delpiano for their technological contribution.
- √ Dr. D. Fukuda as my supervisor at AIST (Advanced Industrial and Science Technology) institute during the fellowship time by Japan Society for Promotion of Science.
- √ The quantum optics group of INRIM for their moral and scientific support: especially Dr. M. Genovese and Dr. I.P. Degiovanni.

I also would like to thank all friends who have welcomed me here in Turin, in some way they have contributed to this thesis work: thanks to Alice, Bujo, Claudio, Gabbro, Ela, Elsa, Iacopo, Peo, Sele ...

A Special thank goes to Dr. S.A. Carboni of *Istituto Nazionale di Fisica Nucleare di Firenze* for his scientific contribution and his heralded lucky despite the long distance.

Finally, special thanks to my family.

Contents

List of Tables

List of Figures

Part I

the pledge

Chapter 1

Introduction

The luminous intensity, in a given direction, of a source that emits monochromatic radiation of frequency 540×10^{12} *hertz and that has a radiant intensity in that direction of* $1/683$ *watt per steradian.*

This is the current definition of the candela, that was adopted in 1979 [1]. The seventh sister within the family of the International System of Unit (SI), as base for a fundamental biological process: the human vision.

The dates of adoption of the present seven definitions (of the SI units) range from 1889, for the kilogram, to 1983, for the definition of the meter [2]. The SI system was adopted in 1960 and in these last five decades its evolution reflects both the science and technology advances, both industry and society needs for a uniformly realizable system of measurements. As consequences, changes in definition have been accepted only when this would represent a significant step forward for the community of users. Following the science and technology progress, starting from 2005 to nowadays, there are substantial efforts directed toward a brand-new definitions of four of these base units. The recommended proposal would redefine kilogram, ampere, kelvin and mole by fixing the values of Planck constant h, elementary charge e, Boltzmann constant k and Avogadro constant N_A, respectively, eliminating as in the kilogram example the last definition in term of material artifact or providing a more realizable definition of the SI unit, as in the case of ampere [3].

About the candela world, optical radiation community has not a common consensus whether this definition fully satisfies the current and future needs of growing associated technologies. Timely with the recommendations for the reformulation of those four units, even the words for the definition of the candela were redrafted to match the standard format suggested for all seven base units, but without changing the meaning of the definitions [4]. Such that, considering the recent advances in optical radiometry, in the development of quantum technologies (detector, source and measurement techniques) [5], and linking to the fundamental constant h, in the

future the luminous intensity unit might be expressed in terms of photon number rather than optical power:

the luminous intensity, in a given direction, of a source that emits monochromatic radiation of frequency 540×10^{12} *hertz and that has a photon intensity in that direction of* $(683 \times 540 \times 10^{12} \times 6.62606896 \times 10^{-34})^{-1}$ *photons per second per steradian.*

To respond to this challenge several national metrology institutes joint into the european research project "qu-candela" (candela: towards quantum-based photon standards) [6], with the aim of demonstrating the viability of redefining the candela in terms of a countable number of photons. Such project, lead by INRIM, had the objective to link optical power measurements at the 100 μW level to those at the level of one or more photons per second, i.e. looking at the energy scale, build a bridge from the classical to the quantum world [7].

In the classical world of radiometry [4], the primary optical radiation scales are generally based on cryogenic radiometry and linked to the SI units of electricity, both for sources and detectors. In the visible range, these scales are established at discrete wavelengths in the 0.1 mW to 1 mW regime with an uncertainties around the 0.005%. In the radiometry quantum world at very low flux levels, the conventional photon counting techniques present a degradation in accuracy. To improve these uncertainties quantum optics techniques are needed: predictable or quasi-single photon sources and photon number resolving detectors are the main tools to advance in the metrological challenge at photon counting regime.

The present definition of the candela is not connected to the concepts of modern physics which underpin the technology developments of quantum optics. On the other hand, the reformulation must be demonstrably capable of being realised at, and better than, the current accuracy of around 50 ppm. The qu-candela project objective [7] was the demonstration of a traceable linkage of the SI to the single photon regime and the development of techniques to scale from high to low photon flux regimes, with relative uncertainties approaching 100 ppm.

In order to realize this aim, the project proposed to use a predictable quantum efficient detector (PQED) [8] to transfer the SI scale to a single photon avalanche detector (SPAD), operating in the few photon regime, $10^6 \div 10^3$ photons/s. The range from this level to the single photon counting regime, $10^3 \div 10^0$ photons/s could be covered by a transition-edge sensor (TES), which is able to distinguish between one or more photons arriving simultaneously, with respect to a conventional single-photon counting detectors.

The work behind this dissertation is included inside the qu-candela project: TES development, in the optical spectral range, started at INRIM several years ago. A transition-edge sensor is typically a thin superconducting film kept within its narrow region between normal and superconducting phase. A TES is a very versatile device

that can be used to detect radiation in a wide energy range from gamma-rays to sub-millimeter [9]. In principle, it operates as a basic thermometer: the absorption of a single photon causes the rise of temperature of the TES, which is observed as a change in the electrical resistance. For this reason sometimes it is called superconducting phase thermometer (SPT). When a thermal detector is used to measure the energy of individual photons, it is called a calorimeter. This intrinsic capability to measure the energy of the photons absorbed and the possibility to resolve the number of photons absorbed distinguish a single photon detector to a photon number resolving (PNR) device.

The PNR property is useful even for other many scientific fields like astronomy, material analysis, quantum information and quantum computation, together with metrology. All of these scientific areas need detectors with high quantum efficiency (QE) and high energy resolution for the measurement of single photons in a broad range of the electromagnetic spectrum.

TES development has been driven by dark matter search and neutrino experiments [10, 11] and both by x-ray microcalorimeters [12] and microanalysis [13]. Subsequently the detection of individual photons from the ultraviolet through the optical to the mid infrared have also been demonstrated [14]. The superior performances of TESs with respect to semiconductor based detectors, in terms of quantum efficiency, dark counts, intrinsic energy resolution and photon number discrimination, lead to applications of TESs for optical astronomy [15], for the x-ray astronomy missions [16] and also for applications where it is fundamental the PNR capability, like quantum key distribution, quantum optics and linear optical quantum computation [17].

For x-ray applications TESs based on different superconducting materials like Al, Ir, Mo, Ti, W and their bilayer with a proximizing normal metal have been applied. For optical applications, extremely good results have been obtained with W at Stanford [18] and NIST [17], with Hf at Stanford [19] and with Ti [20] at AIST. These results have been obtained with single superconducting films, that means that the transition temperature is not easily controlled.

This dissertation shows the results obtained with TES based on titanium/gold film [21]. Thanks to the proximity effect, the multilayer allows to lower with continuity the transition temperature of bulk Ti ($\sim$ 390 mK) and consequently to control the detector characteristics. Our TESs have been developed as photon number resolving detector for the visible spectral range enlarged to cover near infrared wavelengths. The reason of this spectral widening of interest is due to the recent involvement of high performance superconducting single photon detector in a variety of applications of the information, computation and technology quantum field.

I present, in Chap. 2, a brief summary of the prevailing methods of detecting

optical radiation and, in Chap. 3, a detailed look at the physics of the Transition-Edge Sensor. Chap. 4 explains the experimental apparatus used to reach the needed low temperature, the coupling technique to irradiate the TES and read out system; Chap. 5 summarizes specific details on the used detector and the procedure to reach our proposal of detecting incident photons. In Chap. 6, I expose the main results obtained with an accurate analysis on the uncertainty and a new absolute calibration technique to estimate the detection efficiency in photon number resolving detector; in Chap. 7, thanks to a collaboration with the Japan AIST institute, I show the properties of improved detectors focused for telecommunication applications. Ending in Chap. 8 a summary of the outcomes are reported with short view of the on-going work and future prospects.

Chapter 2

Optical Photon Counters

The order of magnitude of the energy of a single photon in the visible or near-infrared spectral range is 10^{-19} J ($\sim$ 1 eV). So an optical single photon counter must be an extremely sensitive device to discriminate these quantum objects.

Conventional single photon detectors are based on photomultipliers and avalanche photodiodes and are used in a wide range of applications [22]. However, these conventional detectors have the limit to only distinguish between incident radiation and no-incident radiation. Their behavior is like a binary response, because a multiphoton pulse gives the same output signal as single photon. The ability to resolve the number of quantum of light reaching the detector simultaneously distinguish the photon number resolving (PNR) detectors inside the single photon counter family.

The major reason that drives the development of PNR detectors is the rapidly expanding interest in optical quantum information applications [9]. Quantum information technologies use individual quantum objects (such as photons) to encode and manipulate information. The two most important quantum information innovations are the optical quantum key distribution and the optical quantum computation [23]. In both of these applications the ability to resolve the incident photon number covers a fundamental role.

Optical quantum cryptography is based on the use of Fock states [5] which unfortunately, are difficult to prepare experimentally. Nowadays, practical implementations of single photon emitters rely on faint pulsed lasers, atoms or ions in resonant cavities [24], organic molecules [25], color centers [26, 27], semiconductor nanocrystals or quantum dots [28] and entangled photon pairs [29]. Unfortunately all of these produce coherent states whose probability obeys Poisson statistic. Hence, single photon sources result imperfect because the probability to have a multiphoton emission is non zero[1]. In quantum cryptography, multiphoton states represent a

[1]The normalized intensity correlation function, $g^{(2)}(\tau)$ [5], is an index that can reveal the quantum nature of light and can be used to determine the degree of nonclassicality of quantum state of light: for a single-photon Fock state $g^{(2)}(0) = 0$, for a thermal state $g^{(2)}(0) = 2$.

security loophole that can be exploited by eavesdroppers [9], from here the importance to develop single photon sources on demand[2] and photon number resolving detectors to well characterize the sources.
The same discussion remains valid in optical quantum computation too. A real production of photons on demand and an efficient detection of all photons are crucial to reduce errors of processing quantum bits [23].

As more accurately described in Chap. 1, the ability to resolve the number of photons is an important property in metrology too. The PNR devices are fundamental tools in the future project to realize the SI unit of luminous intensity, the candela, based on the well defined number of photon emitted by a source. Their role is necessary to cover the range from the optical quantum particle unit (the single photon) to the power detectable by a single photon avalanche detector (SPAD): $\sim 10^3$ photons/s [7].

After introducing the importance of this detector figure of merit (the ability to resolve more than one photon) and keeping in mind the PNR detector's development reason, let's look now at how to discriminate photons and the state of art of prevailing technology in the optical counter field, integrating what recently reviewed in [9].

2.1 Detection Mechanism

The detection of incident photon is based on the interaction of the radiation with material. They can be categorized as photon effects, thermal effects and wave interaction [30].

2.1.1 Photon Effect

One possibility to detect photons is observing their interactions with material electrons and subdivide in internal and external interplays.

In the internal one, photons excite charge carriers: electrons or holes remain within the sample. Internal effects could be subdivided in two subclasses: incident photons interact with bound electrons and produce free electron-hole pairs (a); incident photons interact with already free charge carries (b).

(a) **Photoconductivity** is the most widely employed effect, in which radiation may release an electron-hole pair or an impurity-bound charge carrier and thereby

[2] In this case 'on demand' refers to the ability of a source to produce single photons upon request.

changing the electrical conductivity of the materials. In most cases this change in conductivity is measured by means of electrodes linked to the sample. Such photosignal is detected either as a change in voltage or as a change in current through the sample. Depending on their spectral responsivity function, photoconductive detectors can be distinguished by their working spectral range: visible wavelength, near infrared and far infrared.

(b) **Photovoltaic effect** is the second detection method of general utility. This effect requires an internal potential barrier and an electric field usually across a simple $p - n$ junction even in absence of radiation. Photons incident on the junction producing free hole-electron pairs which are separated by the internal electric field. This effect doesn't give information about the energies of the incident photons.

In the external photon effect, also called photoemission, an incident radiation causes the emission of an electron from the surface of the absorbing material, known as photocathode.

Photoemission is activated by the incident radiation which causes the emission of an electron from the photocathode surface into the surrounding space. An electric voltage between the cathodes drives the electron to the anode.

2.1.2 Thermal Effect

The method based on the thermal effect exploits changes in the material's properties: typically, temperature variations caused by the heating effect of the incident power. Because at low temperatures, materials have special properties like low heat capacity, low thermal and electrical noise, devices have been developed at cryogenic temperature to detect directly single photon events. Moreover some materials, at certain temperatures, become superconductive, allowing the use of their specially and unique electrical and thermal behaviors.
Even if it is not a method we point out the characteristics of a quantum calorimeter to better understand the thermal effect.

Quantum Calorimeter is simply a calorimeter that measures energy[3], and the word "quantum" refers to the fact that we are measuring the energy of quanta of light. With reference to Fig. 2.1, it is composed by an absorber that absorbs the

[3] A calorimeter is "any of several apparatuses for measuring quantities of absorbed or evolved heat or for determining specific heats. From Latin *calor*". If the flux of incident photons is too large to separate individual photons, the detector is used to measure changes in the flux and is called a bolometer.

incident power P_γ, a perfectly coupled thermometer that measures the temperature $T(t)$ increase of the absorber and a weak thermal conductance links to heat sink that allows the absorber to return to the bath temperature. A calorimeter is characterized by the heat capacity $C(T)$ of the absorber's material, the thermal conductance $G(T)$ of the thermal link and by the temperature of the heat sink T_b.

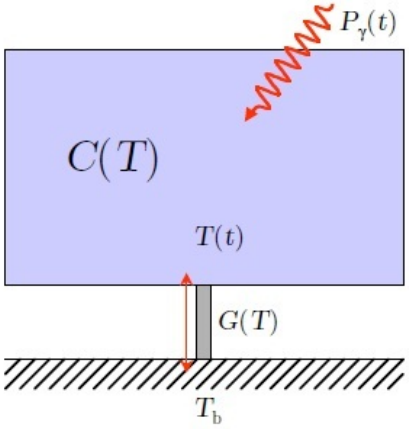

Figure 2.1. A simple calorimeter scheme characterized by the heat capacity $C(T)$ of the absorber's material and the thermal conductance $G(T)$ of the link between the absorber and the heat sink at temperature T_b.

2.2 Technology

Photon number resolution could be achieved in two ways. The first method, multiplexes conventional detectors [31]. This can be achieved either by combining the output signals of an array of detectors (spatial multiplexing) or by splitting the multiphoton pulse via a cascade of beam splitters and then delaying the signals so that they can be detected sequentially by a single detector (time multiplexing).
The second method is based on true PNR detector that intrinsically produce a pulse proportional to the number of absorbed photons [32]: such as Superconducting Tunnel Junctions (STJ) device [33], Kinetic Inductance Detector (KID) [34] and superconducting Transition Edge Sensor (TES) [36]. One of the main goal of these thesis work is to show TES behavior under simultaneously incident photon. Both STJ and KID devices have been developed especially for astrophysical applications, even if multiphoton discrimination has been obtained in optical wavelengths; here we limit to review the more commonly used optical detectors [9, 35], classified under their working temperatures.

2.2.1 Room Temperature Devices

Human eye is the most ubiquitous optical detector with which we are familiar. The retina is composed of around 10^8 rods and over 10^6 cones, the eye has a good imaging resolution with a large field of view. The rods are more sensitive to incoming light requiring as few as one, up to as many as ten photons. The photosensitive device has chemical nature, the rhodopsin or visual purple. Upon the absorption of light, undergoes a structural change which culminates in an electrical signal sent from the cell. The structural change of rhodopsin occurs in only a few picoseconds, with a relaxation time on the order of milliseconds. The combined absorption properties (of rods and cones) give the definition of the visible band of 380 nm to 780 nm, varying a bit by person. The quantum efficiency of a dark adapted human eye has a maximum at 510 nm of 3%.

Photomultiplier tubes (PMTs) were born in 1949 and are the most long time established photon counting technology. They consist of a vacuum tube with a photocathode able to absorb light and to emit electrons through the photoelectric effect. PMTs offer large active areas (diameters > 10 mm) and cover the spectral range of 115 nm – 1700 nm: the maximum efficiency of around 40% is at 500 nm, while at in telecommunication wavelengths is ca. 2% [37]. In certain types of PMTs, the excess noise of the multiplication process is sufficiently low to allow some discrimination between one or multiple photons [38].

Single photon avalanche photodiodes (SPADs) are used in quantum optics laboratories and in free-space quantum key distribution experiments. These solid-state devices are based on an avalanche photodiode structure (f.e. $p-n$ junction): carriers generated by photon absorption undergo avalanche gain triggering a macroscopic breakdown of the diode junction; at the end the avalanche is stopped and the device reseted by a quenching circuit. These detectors offer single-photon sensitivity in the 400 nm – 1 μm range and achieve a peak efficiency of 65% around 650 nm. Photon number resolution has been made indirectly by exploiting timing walk effects [39] or through spatial [40] or temporal-multiplexing [41] schemes.

Frequency up-conversion is a technique to convert a telecommunication wavelength photon to a shorter wavelength that can be more efficiently detected by a commercial single-photon detector. The mechanism exploits sum-frequency generation in a nonlinear optical crystal: weak signal is combined with a strong pump signal at different frequency, to yield an output signal at the sum of the frequencies [42]. There are several technical challenges in achieving high-efficiency up-conversion: in combination with the previous one detector, an efficiency of 46% at 1550 nm has been shown [43].

2.2.2 Cryogenics Devices

Visible-light photon counters (VLPCs) are low-temperature semiconductor-based photon detectors [44]. They operate on recent concept know as solid state photomultiplier maintained at liquid helium temperature: a blocked impurity band device gives single photon sensitivity, in the spectral range 400 nm – 1000 nm, and a controlled single-carrier multiplication process gives a rising signal proportional to the photon number. Detection efficiency is up to 88% at 694 nm and 93 % in the infrared; devices present dark count rate $>$ 20 kHz and the dead time limits the counting rate at $\sim$ 100 kHz.

Superconducting single photon detectors (SSPDs) works in the temperature range of 1.5 K – 4 K, well below the superconducting transition temperature of their constituting material: typically a 100 nm wide wires of niobium nitride film [45]. Nanowires are biased just below its critical current; when a photon strikes the wires a local resistive hotspot is formed, perturbing the current distribution and thus triggering a fast voltage pulse. Devices consist of a meander wire that can covers an area up to 20 μm $\times$ 20 μm. The intrinsic efficiency of a smaller area SSPD is around 20 % at 1550 nm, but with an order of magnitude faster than conventional photon counters. The device photon number ability is provided by spatial multiplexed technique [46].

Quantum dots and semiconductor defects are the bases for a new class of photon detectors. One working scheme could be: the absorption of a photon by a quantum dot alters the tunneling probability in a resonant tunnel diode structure [47]. A second scheme is based on a photoconductive gain mechanism that involves trapping charge, in semiconductor defect or quantum dot layer, which alters the conductance in a field effect transistor [48]. Working around 4 K, an internal efficiency of 68 % at 805 nm with a discrimination of up three photons are already demonstrated, for the second scheme [49].

Superconducting Tunnel Junction (STJ) detectors exploit a type of Josephson junction. A photon absorbed in the superconductor breaks Cooper pairs and creates quasiparticles. The quasiparticles tunnel across the junction in the direction of the applied voltage, and the resulting tunneling current is proportional to the photon energy [50]. STJ devices have been employed as single-photon detectors for photon frequencies ranging from X-rays to the infrared [51]. It has been demonstrated that they can detect individual photons at rates up to 10 kHz in the wavelength range 200-500 nm, with energy resolution $\sim$ 100 nm at a wavelength of

300 nm with a detection efficiency of > 45 % and an operating temperature of 0.37 K [33].

Transition edge sensors (TESs) are the main character of this thesis work, here there will be only a short review of state of art, leaving a complete device explanation in the following chapters. TES is the very high efficiency optical single photon detector with photon number resolving capability [36]. The absorption of incident photons heats the device, which is biased between the superconducting to normal phase, causing a change in resistance; this variation is read out by a SQUID amplifier. The output signal results proportional to the energy of the photon or, at fixed wavelength, the photon number. High temperature devices (i.e. critical temperature $T_c \sim 300$ mK) covered by antireflection coating, have shown a detection efficiency of 98 % at 850 nm and a dead time around 100 ns [20]. Low temperature TESs (i.e. $T_c \sim 100$ mK) have presented a 95 % of efficiency at 1550 nm, embedded in an optical cavity [18]. The photon number resolving capability is excellent: up to twenty nine photons can be clearly resolved [21].

Kinetic Inductance Detectors (KIDs) work on the principle that incident photons change the surface impedance of a superconductor ($T_c \sim 300$ mK) through the kinetic inductance effect [52]. This change can be accurately measured by placing this superconducting inductor in a lithographed resonator extremely versatile. Multiplexing detectors into large arrays are able to cover the ultraviolet, optical, and near infrared (0.1-5 mm) wavelength range. In the optical range the energy resolution results are not so good as in the others and the response time limits the counting rate at few kHz [53].

Chapter 3

Transition Edge Sensor

In the superconducting detector's field, Transition Edge Sensors recently met with success. They have been used to achieve the best energy resolution from the near infrared to gamma rays and detect photon fluxes out to millimeter wavelengths [36]. At INRIM, in collaboration with Dr. E. Monticone's group, we have developed and characterized a TES system optimized for single photon spectroscopy at telecom - visible energies.

This chapter introduces the theory of a superconducting transition edge sensor. It describes the TES thermal-electrical model summarizing the main equations that predict its behavior, analyzing the bias circuit for a TES and its electrical and thermal response.

3.1 Thermodynamic Behaviour

Fig. 3.1 reports the thermal model of a transition-edge sensor [36]. In the model we can distinguish the electronic component (e) and the phonon component (ph) of a generic superconducting material with their temperature T_e and T_{ph}, respectively. These two components are thermally connected one with each other by means of the conductance $g_{e,ph}$. Another conductance, indicated as $g_{ph,sub}$ connects the phonon component of the superconducting material with the substrate. Through the $g_{sub,b}$ conductance, the substrate is connected to the thermal bath, at temperature T_b.

Below one kelvin, the system is in the electron-phonon decoupling regime and the temperature of phonon system and the substrate phonon system will be at the temperature of the bath. In the meanwhile the thermal conductance $g_{e,ph}$ (being much smaller than $g_{ph,sub}$ and $g_{sub,b}$) will behave like a thermal bottleneck for the heat of the electron region.

Following this thermal model, if an incident photon power (P_{inc}) hits the device, the electronic temperature T_e will rise until the system dissipates the heat (P_{s}) to

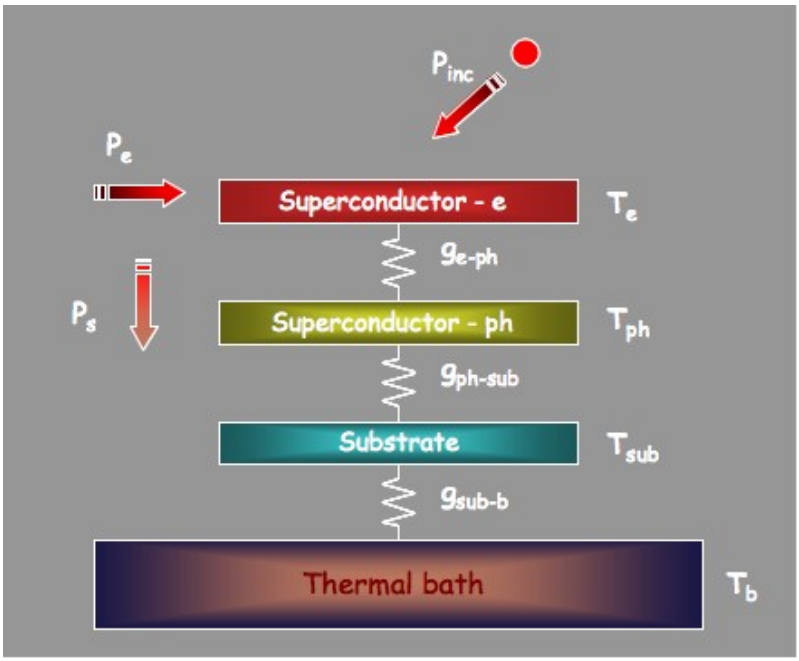

Figure 3.1. Thermal model of a Transition-Edge Sensor. $P_{\rm inc}$ is the incident photon power, $\rm P_e$ is the Joule-heating bias power and $P_{\rm s}$ the power dissipated in to the system through the weak thermal link $g_{e,ph}$. At critical temperature $g_{e,ph} << g_{ph,sub}$ and $g_{e,ph} << g_{sub,b}$.

the thermal bath, through the phonon system. The thermal recovery time needed to unclench the entire system to the initial state is $\tau_{\rm th} = C/G$: the ratio between the heat capacity of the superconducting material and the dominant thermal conductance G, i.e. being below 1 K, it corresponds to $g_{e,ph}$. Looking at the thermal power balance equation the temporal behavior of the system can be studied by:

$$C\ \dot{T}(t) = P_{\rm inc} - P_{\rm s} \tag{3.1}$$

For temperature close to T_b, $P_{\rm s}$ is approximated by:

$$P_{\rm s} = G\ (T(t) - T_b)$$

Substituting $P_{\rm s}$ in Eq. 3.1 and solving for $T(t)$ produces:

$$T(t) = T_b + \Delta T(t) \qquad \text{where} \qquad \Delta T(t) = \Delta T_0\ e^{-\frac{t}{\tau_{\rm th}}},$$

the exponential decay starts from the temperature[1] ΔT_0 and goes down to T_b, with the time constant $\tau_{\rm th}$.

In order to lower this thermal recovery time, we require the use of injecting power ($P_{\rm e}$) directly into the electron system of the TES. Exploiting the thermal impedance between the electronic region and the phonon system and providing the $P_{\rm e}$ power, the electronic temperature T_e can be thermalized at an higher value than the phonon one's: $T_e > T_{ph}$. In such a way, after the photon absorption, the electronic system relaxes to a working temperature (T_0) higher than T_b, maintaining the isolation from the phonon system. The importance of having this isolation between the two systems means that the excitation, due to the photon absorption, can be completely read out by the current through the sensor, instead of loosing it through the phonon system.

Several different ways of providing $P_{\rm e}$ to the TES have been developed [54]: Galeazzi [55] Irwin [56], Meier [57]. The most used is the one proposed in 1995, by K.D. Irwin: a bias technique which uses resistive heating in the electron system of the TES itself as a bias heater. The most significant benefit of using such self-heating in biasing the devices is the self-regulation which each device performs within its own electrothermal system greatly easing the temperature-regulation: some theoretical results are discussed below.

3.2 Electro-Thermal Feedback

In order to understand qualitatively how this self-regulation works, let's assume the TES biased in its superconducting transition and consider the electrical circuit used to bias the device of Fig. 3.2 (used also to read out the signal).

By starting with the TES in its superconducting state, all the bias current $I_{\rm bias}$ passes through the TES until its critical current value is reached. After that, an increasing of the bias current produces an increase of the TES resistance.
In order to have a constant voltage across the parallel (between the TES branch and shunt resistance), $R_{\rm sh}$ is chosen tens time lower than the TES normal resistance. In such a way, the increase of the TES resistance drives $I_{\rm bias}$ through the $R_{\rm sh}$. This also leads to control the TES resistance, maintaining its value in a determinated working point, only varying $I_{\rm bias}$.

The voltage across the device $V_{\rm bias}$ will apply a power $P_0 = V_{\rm bias}^2/R_0$, where R_0 is the resistance value at the working point. Since in a superconducting material $\mathrm{d}R/\mathrm{d}T$ has positive slope, any increase in temperature will increase the resistance

[1] Ideally, the energy is deposited instantaneously, leading to an initial temperature increase $\Delta T_0 = E_\gamma/C$. Experimentally we have to consider the collection efficiency ε, that we will introduce in Chap. 6, which is the fraction of photon energy deposited in the electron system following the photoelectron cascade: such as the previous equation becomes $\Delta T_0 = \varepsilon E_\gamma/C$.

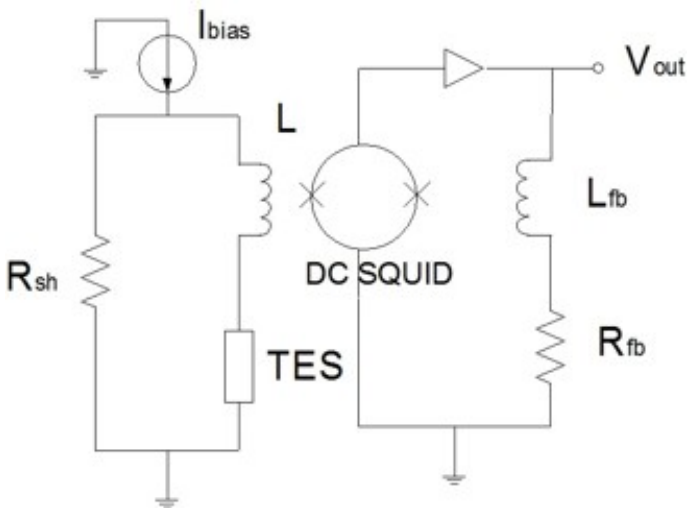

Figure 3.2. TES bias circuit with SQUID read-out.

and, due to the constant voltage applied to the device, P_0 will drop proportional to $1/R$. This decrease in Joule power acts to cool the sensor back toward the bias point. Correspondingly, a decrease in temperature will decrease the resistance and heat the sensor. This self-regulating "electrothermal feedback" (ETF) [56] obviates the need for precise thermal control, allows to work with $T_b < T_c$ and simplifies device operation greatly.

As a consequence, when an incident photon is absorbed, the TES temperature increases with an increment of the TES resistance, as we can see in Fig. 3.3. As explained before, this further increase of the TES resistance drives I_{bias} through the R_{sh} until the TES will not return to its superconducting state. Since V_{bias} is constant and considering the increase of the resistance, we have a lower value of dissipated power by the TES, and most of the I_{bias} passes through R_{sh} due to the increment of TES resistance. The current I_{sensor} through the device results much lower than before and the TES can come back to its initial state, ready to detect another event. The inset of the Fig. 3.3 shows the corresponding negative current pulse measurable using a DC SQUID.

To understand ETF and its consequences to device operation it is convenient to review the details of TES physics [36]: the standard differential equation of the thermal balance is

$$C_e \frac{\mathrm{d}T}{\mathrm{d}t} = \frac{V_{\text{bias}}^2}{R(T)} - k\,(T_e^n - T_b^n) \tag{3.2}$$

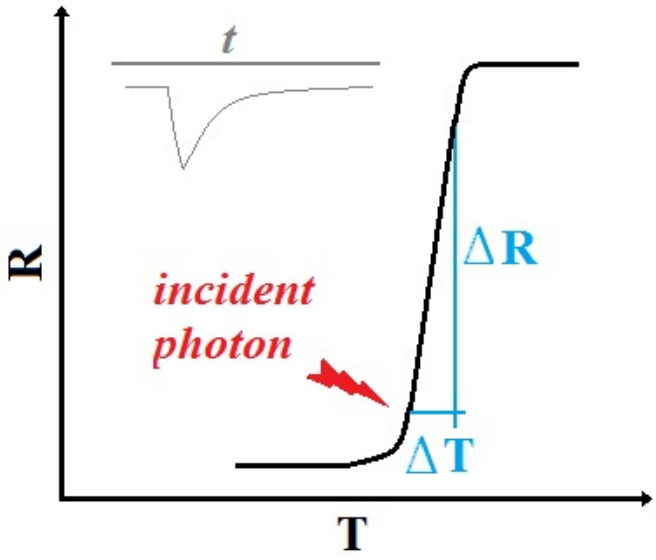

Figure 3.3. Plot of a resistance vs. temperature for the superconducting to normal transition. The inset shows a typical current pulse of the detector output corresponding to the absorption of a photon. For ease of representation the ΔR effect reported in this figure is not in scale.

C_e is the electronic heat capacity of the superconductive material and k is the thermal coupling constant; n is the thermal coupling power-law exponent in the range of $4-6$ depending on the coupling model and on the transition temperature of the superconducting material [58].
In steady-state, the power input provided by the voltage bias balances the flow of power out of the sample into the bath, that is

$$\frac{V_{\text{bias}}^2}{R_0} = k\ (T_0^n - T_b^n) \tag{3.3}$$

with T_0 and R_0 respectively the steady-state temperature and the resistance.

When an incoming photon with energy E_γ is absorbed, all the energy is very rapidly distributed to the entire electron system and, as we have already explained, the temperature increases by $\Delta T_0 = E_\gamma/C$. The expansion of Eq. 3.2 to the first order in ΔT is

$$C_e \frac{\mathrm{d}\Delta T}{\mathrm{d}T} = \frac{V_{\text{bias}}^2}{R_0} - k\ (T_0^n - T_b^n) - \frac{V_{\text{bias}}^2}{R_0^2}\frac{\mathrm{d}R}{\mathrm{d}T}\ \Delta T - n\ k\ T_0^{n-1}\Delta T \tag{3.4}$$

In Eq. 3.3 the first two terms can be deleted and with the definitions below:

$$G = n\ k\ T_0^{n-1}, \qquad \alpha = \frac{T_0}{R_0}\frac{\mathrm{d}R}{\mathrm{d}T} \qquad \text{and} \qquad P_0^2 = \frac{V_{\text{bias}}^2}{R_0}$$

it is easy to obtain the follow differential equation

$$\frac{\mathrm{d}\Delta T}{\mathrm{d}t} = -\left(\frac{P_0}{T_0 C_e}\ \alpha + \frac{G}{C_e}\right)\Delta T \tag{3.5}$$

where α gives information on the sharpness of the transition curve of devices and in general it is a positive number $>> 1$. Eq. 3.5 has exponential solution with time constant

$$\tau_{\text{eff}} = C_e\left(\frac{P_0}{T_0 C_e}\ \alpha + G\right)^{-1}$$

Remember that $\tau_{\text{th}} = C_e/G$ is the intrinsic thermal recovery time without bias power, so from previous equations we reach the equivalent form

$$\tau_{\text{eff}} = \tau_{\text{th}}\left(1 + \frac{\alpha}{n}\left(1 - \frac{T_b^n}{T_0^n}\right)^{-1}\right)$$

In case of the strong electrothermal feedback regime, $T_b << T_0$, the effective response time constant τ_{eff} becomes

$$\tau_{\text{eff}} \approx \frac{n}{\alpha}\ \tau_{\text{th}} \tag{3.6}$$

The effect of ETF on pulse recovery time is now quite apparent. It is clear that in presence of ETF bias, the effective recovery time τ_{eff}, is lower than the thermal recovery time τ_{th} on the rise of α.

The full solution of Eq. 3.5, for the exponential decay of a small impulse increase in temperature becomes

$$\Delta T(t) = \frac{E_\gamma\ \varepsilon}{C_e}\ \exp\left(-\frac{t}{\tau_{\text{eff}}}\right)$$

where ε is the fraction of photon energy deposited in the electron system following the photoelectron cascade.

3.3 Energy Resolution

One of the most important figure of merit for a TES calorimeter is the energy resolution: the intrinsic device resolution. In [56], [59] – [61], a detailed analysis shows that the energy resolution depends strongly on the temperature because of the temperature dependence of the heat capacity, thermal conductance, thermal noise, and other parameters.
In chapters 6.1.2 & 7.2 this parameter will be estimated to fully characterize our TES devices, in this section there is only a short review to point out the main contributes to the intrinsic device resolution.

The energy resolution of a generic calorimeter can be expressed as [36]

$$\Delta E = \left(\int_0^\infty \frac{4}{S_{P_{\rm tot}}(f)} \, \mathrm{d}f \right)^{-\frac{1}{2}} \tag{3.7}$$

where $f = \omega/2\pi$ and $S_{P_{\rm tot}}(\omega)$ is the power spectral density of the total noise: the sum of the contributions from Johnson noise, current-fluctuations noise, due to thermal fluctuations, and current-referred amplifier noise.

Let's try for a while, to express the main contributes to the total noise as considered in [36]. The TES voltage Johnson noise referred to a power S_V is obtained by the power spectral density of the current noise due to Johnson noise voltages in the TES S_I and power-to-current responsivity s_I

$$S_{\rm V}(\omega) = 4k\ T_0 I_0^2 R_0 \frac{\xi(I_0)}{\ell_I^2}(1 + \omega^2 \tau_{\rm th}^2)$$

where we have introduced the low frequency loop gain under constant current $\ell_I \equiv P\alpha/GT_0$ and power spectral density with current-dependent nonlinearity $\xi(I_0)$. Similarly, the power noise refers to the current noise due to Johnson noise voltages in the load resistor can be found as

$$S_{\rm L}(\omega) = 4k\ T_L I_L^2 R_L \frac{(\ell_I - 1)^2}{\ell_I^2}(1 - \omega^2 \tau_I^2)$$

The term due to the thermal fluctuation noise can be expressed as

$$S_{\rm TFN} = 4k\ T_0 G \times F(T_0, T_b)$$

where the form of the unitless function $F(T_0,T_b)$ depends on the thermal conductance exponent and on whether phonon reflection from the boundaries is specular or

diffuse. $F(T_0,T_b)$ is defined as function of the temperature of the TES, and typically lies between 0.5 and 1 [62].
A final noise term that is routinely encountered in an ideal linear TES is the noise of the SQUID amplifier. DC-SQUID amplifiers have both noise referred to an input current and voltage noise due to the back action of the SQUID. Correlations in these two noise sources are important. Fortunately, for TES applications, the impedance of the TES is generally much higher than the noise impedance of the used SQUID [63, 64]. Thus, we can neglect the correlated voltage noise terms. The current-referred amplifier noise is $S_{I_{amp}}(\omega)$, which makes the power-referred amplifier noise:

$$S_{amp}(\omega) = \frac{S_{I_{amp}}(\omega)}{|s_I(\omega)|^2}$$

In the important limit that the amplifier noise $S_{I_{amp}}$ is negligible with $\ell_I >> 1$ and zero load resistance R_L, the integration of these noise contributes in Eq. 3.7 gives

$$\Delta E = \sqrt{\frac{\tau_{\rm th} I_0}{\ell_I}\sqrt{S_{\rm TFN}\cdot S_{\rm V}}} \tag{3.8}$$

Let's remember our TES model: a heat capacity C_e at temperature T_0 connected to a thermal bath (the substrate) at temperature T_s through a thermal link with conductance G $g_{e,ph}$. The electron system exhibits temperature fluctuations due to power fluctuations through the thermal conductance to the phonon system. This "phonon noise" can be shown to be the dominant intrinsic noise in a TES with electrothermal feedback due to the suppression of Johnson noise [36].

In the approximation of a dominant gaussian phonon noise[2] (i.e. neglecting the noise contributions from the other sources), in the frequency band over which ETF operates (i.e. $\omega < 1/\tau_{\rm eff}$), taking for example a high-α device (i.e. $\alpha/n > 1$), the effect of the phonon-noise fluctuations on the energy resolution reduces the formula of Eq. 3.8 to the simple form [56]:

$$\Delta E_{\rm fwhm} \approx 2\sqrt{2\ ln(2)}\sqrt{4\ k\ T_0^2\ \frac{C_e}{\alpha}\sqrt{\frac{n}{2}}} \tag{3.9}$$

for $F(T_0,T_b) = 1/2$, $T_b << T_0$ and $\xi(I) = 1$.

From Eq. 3.9 the electronic heat capacity plays a crucial role in determining the device behavior. A heat capacity that is too high will result in a temperature

[2] If there are nonlinear elements, such as nonlinear TES resistance or thermal conductance, the noise is non-Gaussian and the energy resolution calculations are not rigorously applicable.

change during an event that is too small to be accurately measured above the thermal fluctuations in the device. A heat capacity that is too low will cause the temperature excursion during an event to exceed the width of the superconducting transition, causing device saturation.

We could define the maximum energy saturation $E_{\rm sat} \equiv P_0 \tau_{\rm eff}$ as the maximum energy that the ETF mode can remove during the effective recovery time $\tau_{\rm eff}$. In the limit of strong electrothermal feedback ($T_c >> T_b$ and $\alpha > n$) we find that $E_{\rm sat} \simeq C_e T_0 \tau_{\rm eff}$ and Eq. 3.9 becomes

$$\Delta E_{\rm fwhm} \approx 2.355 \sqrt{4\ k\ T_0\ E_{\rm sat} \sqrt{\frac{n}{2}}}$$

This last equation shows how a device working point temperature, T_0, plays an important role in the energy resolution determination. For example, changing only T_0 from 0.3 K to 0.1 K means to gain about a factor 2 in the intrinsic device resolution.

Since our energy collection is not complete, as discussed at the end of previous section (Chap. 3.2), our effective energy resolution drops proportionally with the collection efficiency ε. Our effective resolution for such a device is thus $\Delta E_{\rm eff} = \Delta E_{\rm fwhm}/\varepsilon$. Fortunately, as it is shown in chapters 6.1.3 & 6.2, for our Ti/Au devices, ε value is close to 0.9, reducing the difference between $\Delta E_{\rm eff}$ and $\Delta E_{\rm fwhm}$.

Part II

the turn

Chapter 4

Experimetal Apparatus

4.1 Dilution Refrigerator

The critical temperature of our Ti/Au TESs goes down from about 400 mK (of Ti bulk) to 130 mK $\div$ 70 mK (see section 5.1). Due to this reason and to take advantage of the negative Electro-Thermal Feedback (see section 3.2), we require a refrigeration system which allows to reach temperatures down to 50 mK. The used cryostat is an Air Liquide MINIDIL OD70 - 30 mK dilution refrigerator, with a nominal cooling power about 25 μW at 100 mK. This cryostat [65] is able to reach a base temperature of 40 mK using a mixture of ^{3}He -^{4}He. By the contrary of all other refrigerators that are so called 'one shot', dilution units can maintain such very low temperature for months (theoretically for ever), because the mixture of Helium flows inside a closed circuit without losses.

Looking at Fig. 4.1, the lowest temperature is reached into the Mixing Chamber (MC) where the experimental apparatus is placed: the MC is made of Cu because of its good thermal conductance at low temperature. Here the ^{3}He -^{4}He mixture is liquid and there is a separation between the ^{3}He concentrated phase and the^{3}He diluted phase.

Starting from here the lower diluted phase goes up and reaches the 'still' chamber through the counterflow heat exchangers. The concentrated 'hot' phase flows in the inner tube towards the MC, whereas the 'cold' diluted phase coming from the MC flows in the outer tube. The cooling of ^{3}He (which comes back to the MC) by means of the out coming diluted phase is fundamental: the temperature of the concentrated phase is higher than the MC and without a precooling of hot phase the dilution process doesn't work.
The counterflow heat exchanger is made by means of two concentric capillaries (diameters ranging between 0.5 mm and 1 mm, walls 0.1 mm $\div$ 0.2 mm) with length of a few meters. The capillary material must have low thermal conductivity as Cu-Ni

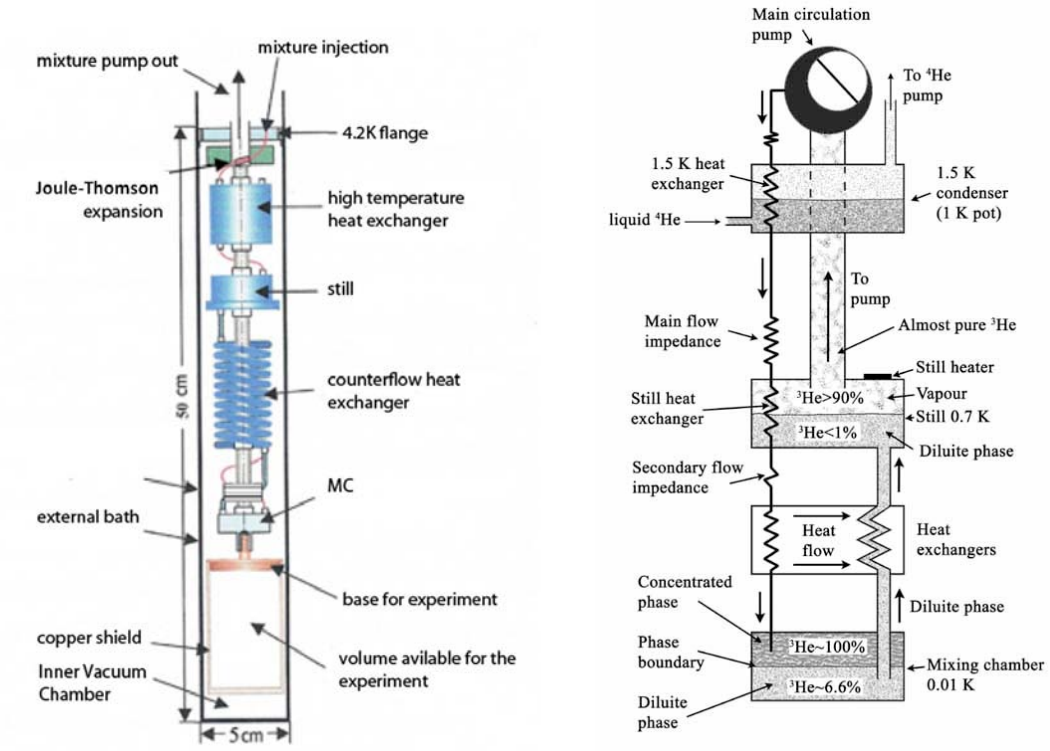

Figure 4.1. On the left a component scheme of our Dilution Refrigerator (without the so called '1 K pot'); on the right a working scheme of a DR.

alloy, stainless steel or brass. They are wound in coil form for space reasons. In this type of heat exchangers, the temperature continuously changes along the coil: heat is exchanged between the two liquids through the separation wall, while the heat conduction along the capillaries must be negligible. In order to increase the contact surface, especially in the lower temperature part, the inner capillary is wound in a spiral form.

The diluted phase after having passed through the heat exchangers, reaches the still. This consists of a chamber where the diluted liquid phase is in equilibrium with a vapor that is practically only ^{3}He. In fact, at the typical working temperature of the still (0.7 K), the ^{4}He vapor concentration is only a few percent.
The ^{3}He evaporated in the still is pumped by an external circulation pump. The still temperature is kept between 0.6 K $\div$ 0.8 K, sometimes by means of a heater. Changing the temperature within this range allows to control the ^{3}He vapor pressure, while a low ^{4}He concentration in the vapor is keeping. In fact, the DR efficiency critically depends on the ^{3}He -^{4}He ratio in the circulating mixture. The still cooling

power due to the ^{3}He evaporation process, can be relatively large (about 1 mW in more common DR). It is thus possible to thermally connect a thermal shield to the still and also to fix and thermalize capillaries, wires and fiber optics.

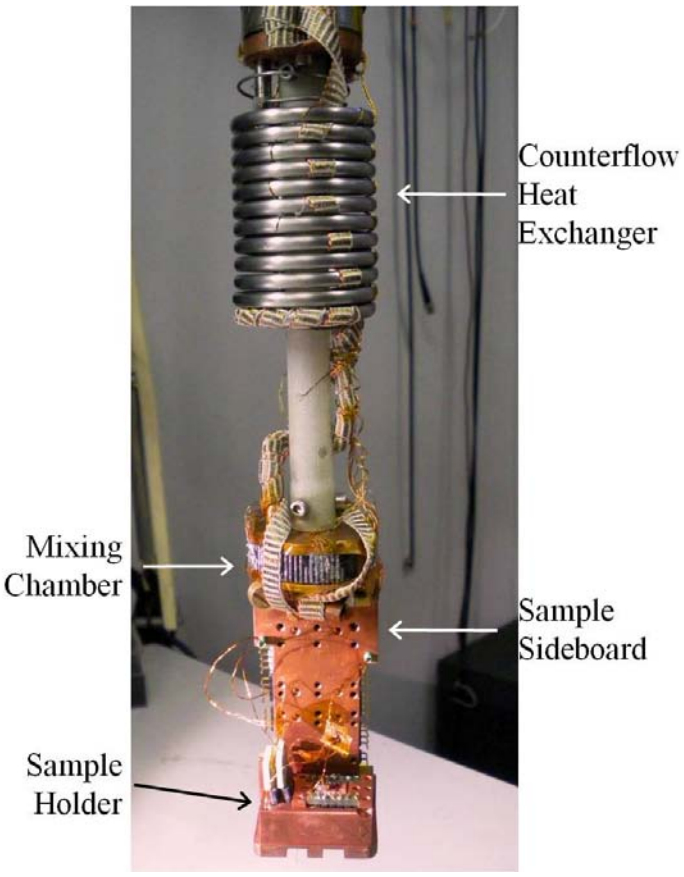

Figure 4.2. The end part of the DR where is placed the experimental apparatus.

The gaseous ^{3}He, removed from the still by the external pumping system at room temperature, is purified in a N_2 liquid trap and again cooled at 4.2 K by the ^{4}He bath in which the dilution unit is immersed. After the cooling at 4.2 K, the mixture undergoes a first condensation produced by a Joule-Thomson (J-T) expansion which takes place after a precooling in a J-T heat exchanger. Then continuous heat exchanger inside the still provides the recondensation of the fluid partially evaporated in the expansion through the impedance. Finally, the concentrated liquid phase undergoes cooling processes in the heat exchangers before reaching the MC where the cycle is accomplished.

The experimental apparatus is mounted under the mixing chamber to ensure

adequate thermal contact (Fig. 4.2). The sample sideboard has been designed and made with OFHC copper to maximize the material conductivity and to shield the 4 K radiation from the thermal bath. It is linked to the mixing chamber by brass screws.

The TES chip carrier is placed upon a little parallelepiped OFHC copper holder (Fig. 4.3, developed by Dr. E. Taralli) and with Al wire bonding it was joined to the connector. This connector is used to link the TESs with both the R_{bias}, made by 100 μm thick gold wire, and the dc-SQUID current amplifier. The OFHC copper holder has an inside cavity where are placed the R_{bias} and the SQUID, (Fig. 4.3). This latter is linked to the connector by Al wire bonding. The sample holder can be placed both on the vertical or horizontal wall of the sample sideboard using brass screws.

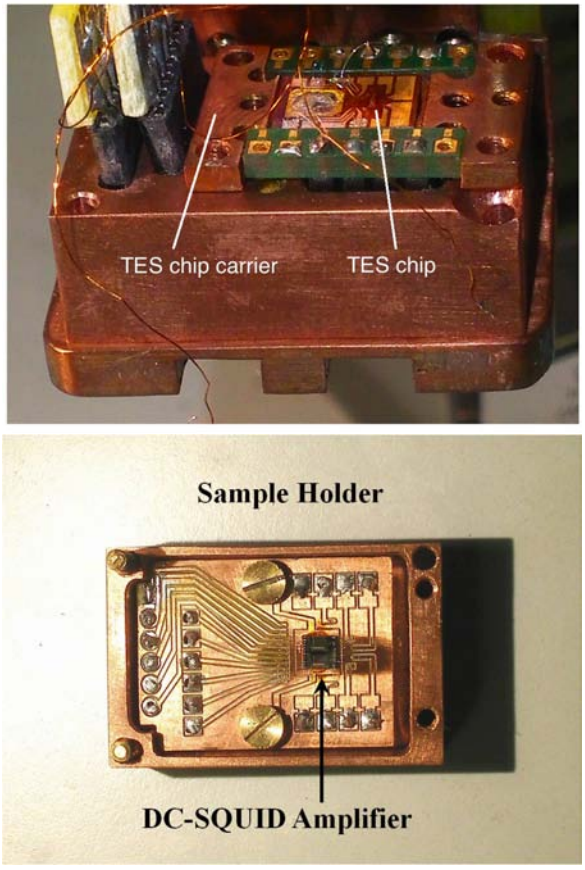

Figure 4.3. The sample OFHC copper holder: (top) the TES chip carrier mounted over the parallelepiped holder; (bottom) the inside cavity of the parallelepiped holder where is placed the dc-SQUID amplifier.

On the three stages of the dilution, 4 K, still and mixing chamber, there are three thermometers to check the temperatures of the cryostat during its function. The last one is also used to measure the critical temperature[1]. The resistance of the thermometers are read out by our LakeShore 370 AC resistance bridge. This instrument reads out the resistance through a four wire measurement: it applies a small current to the resistive thermometer through two wires, and it measures the potential difference via the other two. The sensitivity of the temperature measurements is limited by electronic noise in the thermometer. We typically obtain measurements as good as tens of μK.

4.2 Alignment System

To better understand the optical assembly here presented, let's consider for a moment the picture of Fig. 5.2, where a top view of our typical TES chip is reported. As we will explain (Chap. 5.1), on each substrate there are four TESs, two 20 μm $\times$ 20 μm and two 10 μm $\times$ 10 μm, and a big gold area.

The coupling system [67] consists of a fiber optics array, assembled on a Si V-groove; it can be glued to a copper bracket or a glass prism, which can be soldered onto the gold pad of the TES chip (silicon substrate in Fig. 4.4). On one side of the glass prism, a thin gold deposition is present to allow the soldering between the prism and the TES chip.

The fiber optics are single mode at 1550 nm due to our interest in the telecommunication wavelengths. The tips of the fibers are polished at an angle of 10 degrees to avoid the back reflections from the detectors into the fibers. The eight fibers array, assembled on the Si V-groove, has been produced by OZ Optics [68], on our design. The distance between neighboring fibers is 250 μm, the last fiber is 1750 μm from the first. Since the distance between TES 1 and 3 or between TES 2 and 4 (see Fig. 5.3) is 1750 μm, we can easily align two TESs.

The V-groove assembly is fixed on the vertical side of a copper 90 degree angle bracket by using a two component silver filled epoxy glue. Due to its high thermal conductivity this glue is ideally suited for thermal management applications [69]. Using a stereomicroscope, a self-made clamp and an hot plate, we glue the bracket and the V-Groove Assemblies together. The hot plate is necessary to heat the assembly at 120 °C to harden the glue.
In order to solder the copper bracket–V-groove assembly over the gold area (see

[1] To have a better control of the temperature device, a thermometer should be placed as near as possible to the sample holder: in [66] has been already demonstrated that the temperature difference between the two thermometers is negligible with respect the temperature measurement accuracy.

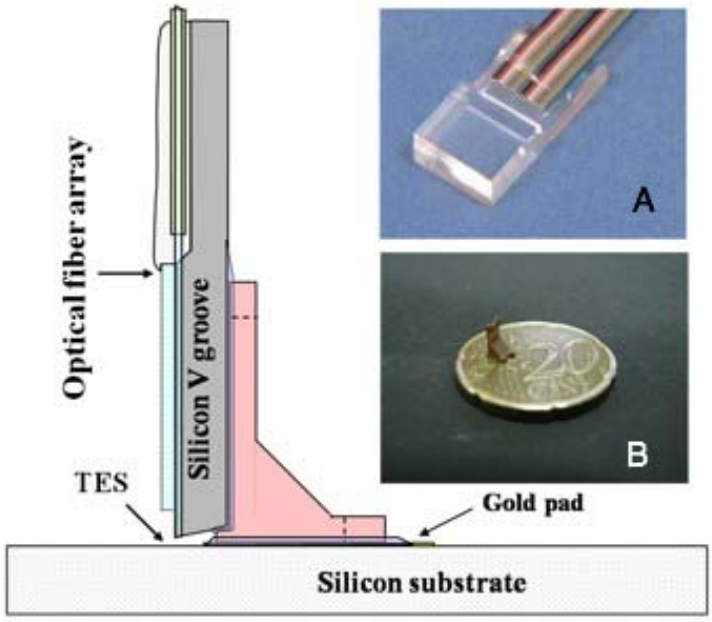

Figure 4.4. Design of the copper bracket and silicon V-Groove assembly, mounted on TES chip (silicon substrate). Inset: (A) Pigtailed V-groove array with 8 channel fibers; (B) copper bracket compared with a 20 cent euro coin.

Fig. 5.2), the TES chip is mounted on a copper holder. To bond the copper bracket to the gold area of the TES chip, we use a solder and a soldering flux. The solder is an alloy from Indium Corporation of America, with a low melting temperature of 58 °C, in order to avoid the diffusion between the gold and titanium layers in the TESs [76]. The soldering flux is formulated to remove oxide films from the metal and to allow solder and metals to dissolve into each other. Heating the copper holder, by using a hot plate, we are able to uniformly melt the solder on the area where we are going to fix the bracket and therefore the V-Groove Assembly.

To align the system we drive the copper bracket–V-groove assembly on the chip bracket area with a 3-axis stage controlled by DC stepper motors. We continuously monitor, using a stereomicroscope, the position of the spots, produced by the illuminated fibers, relative to the TESs. The white light from the illuminator can be regulated in order to see the detector and the light beam. This is fundamental to be sure to reach a good alignment. When the alignment has been reached, the solder, placed on the bracket area, is heated to its melting point and the bracket placed in contact with the chip carrier [70].
The stereomicroscope is a Leica M125, fully apochromatic, magnification of 8× – 100× (12.5:1 zoom range), that allows a wide sample overview and structural detail

down to 1.15 μm resolution. It is mounted to look the chip under 45 degrees with respect to the fibers. In this way it is possible to see if all the light is on the TESs and decide when the bracket is ready to be fixed.

To evaluate the geometrical coupling between the spot diameter and the TES, let's assume a Gaussian profile for the fundamental mode of propagation in the fiber optic [71]. In this way, looking at Fig. 4.5 we estimate the spot diameter on the TES using the relation:

$$d(z) = 2w_0\sqrt{1+\left(\frac{\lambda z}{\pi w_0^2}\right)^2} \tag{4.1}$$

where z is the fiber–TES distance along the beam axis, λ is the wavelength and w_0 is the radius of the $1/e^2$ irradiance contour at the plane where the wavefront is flat.

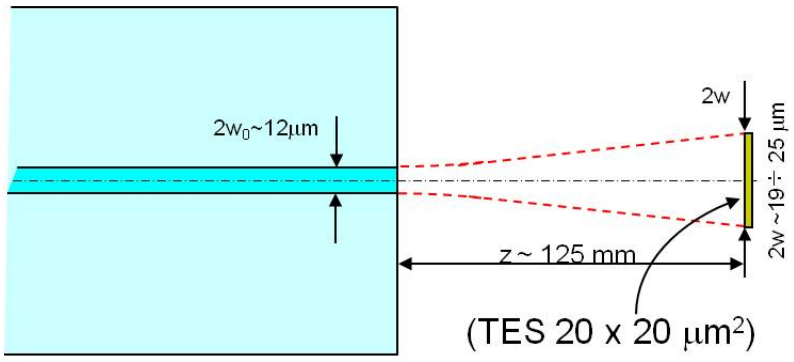

Figure 4.5. Evaluation of the geometrical coupling between the spot diameter and a 20 μm$\times$ 20 μm TES.

For a 9 μm single mode fiber core at 1310 nm w_0 is 4.75 μm and we obtain a geometrical coupling $\eta_{acc} \sim 80\%$ at z= 125 μm and $\eta_{acc} \sim 100\%$ at z= 100 μm. Using the source at 1570 nm w_0 is about 10 μm and we have $\eta_{acc} \sim 65\%$ at z= 125 μm and $\eta_{acc} \sim 80\%$ at z= 100 μm.

In practice, the distance between fibers and detectors is usually close to 150 μm, implying a geometrical coupling $\eta_{acc}(\lambda = 1310\text{ nm}) \simeq 60\%$ and $\eta_{acc}(\lambda = 1570\text{ nm}) \simeq 50\%$. This effect is due to the solder thickness and to defects in the bracket fabrication.

An improvement of this alignment technique will be obtained by using the glass prism instead of copper bracket and spherical lensed fiber. In fact, the production in the workshop of the tiny bracket made of copper, a soft metal, presents both many difficulties and always small imperfections. On the contrary, glass prism can

be obtained with control of the order of λ, that allows a better control of the fiber positioning.

For a gaussian beam propagating in free space, lensed fibers are able to focus the spot, called beam waist w_0 and defined as previously for flat fiber, at fixed distance z between w_0 and the fiber tip (Fig. 4.6).
Still following the Eq. 4.1 and using single mode lensed fiber at $\lambda = 1.55$ μm, with a lens radius of 14 μm, we estimate $w_0 = 2.5$ μm at 22 μm from fiber tip. The spot dimension ratio $2w_0/d(z)$ increases of 10% at $z = \pm 8$ μm around the beam waist. In the case of a 10×10 μm^2 active area TES, a complete geometrical coupling would be obtained in the range $0 \div 50$ μm from the fiber tip. With a 20×20 μm^2 TES, this distance could increase still maintaining a good coupling.

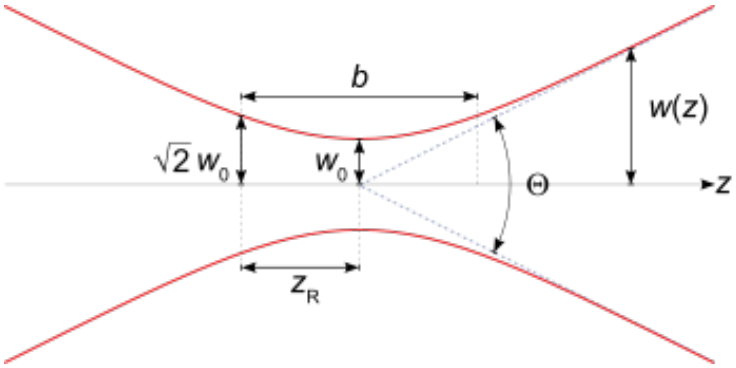

Figure 4.6. Gaussian beam width of a lensed fiber as a function of the axial distance from the beam waist.

4.3 DC-SQUID: Readout and Biasing

A dc Superconducting QUantum Interference Device (SQUID) [72] is a magnetic field sensor converting the flux Φ threading the SQUID loop into a voltage V across the device. In many applications SQUIDs are used as a low noise current amplifier rather than a magnetic field sensor, e.g. to sense the current in a superconducting pickup coil or to read out cryogenic detectors.

To read out TES microcalorimeter signals, a large bandwidth and low noise amplifier is necessary.
The bandwidth of the electronic amplifiers should exceed the bandwidth of the microcalorimeter in this way all the frequency components of the signal are measured. Furthermore, the rise of the pulse, which is typically less than a microsecond, can be used by used to trigger the pulse measurement: so in order to accurately measure the shape of the pulses, a fast amplifier is essential.

The low noise property is necessary because the TES energy resolution is affected by the SQUID noise, that must be much lower than the detector's phonon and voltage noises.

Details of SQUID array testing, noise performance, and optimization of working point are covered thoroughly in other sources, [73, 74], so only a brief overview about characteristics of some used devices will be provided here.

The readout system applied in this work is based on a XXF-1 room temperature electronics made by Magnicon GbR and the dc-SQUID chips are provided by the Physikalisch-Technische Bundesanstalt (PTB) of Berlin. Fig. 4.3 shows a picture of

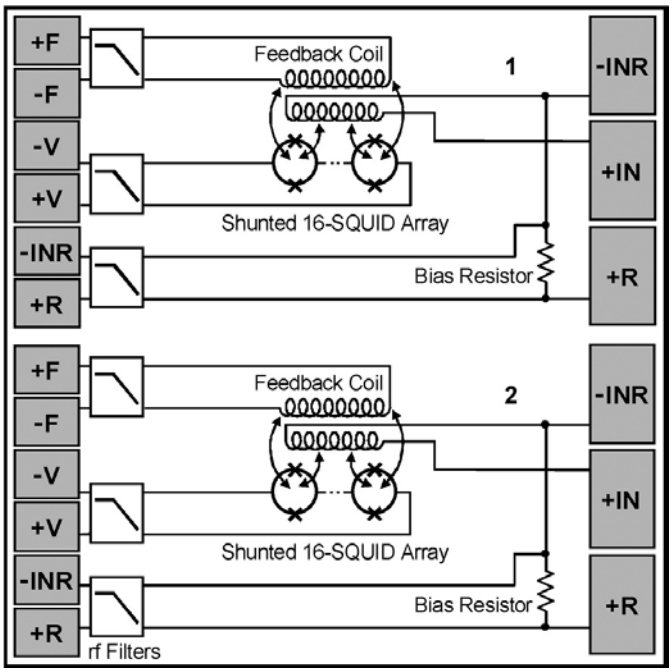

Figure 4.7. Basic circuit diagram of the 3 mm × 3 mm sensor chip 4X16F. The chip contains two independent 16-SQUID arrays. [73]

one of the low inductance dc-SQUID used in the experimental apparatus; while in Fig. 4.7 the corresponding basic circuit diagram is reported: it is a 4X16F 3 × 3 mm^2 size sensor chip which contains two independent 16-SQUID arrays. Each array has a feedback coil and an input coil with L_{in} <3 nH. The rf filters, as well as the bias resistors for detector operation, were integrated into the chip, even if for our applications we used an external R_{bias}, due to a necessary different resistance value needed.

The other SQUID amplifier applied in this thesis is a 5X114W two-stage sensors without input transformer and with a lower input inductance of about 2 nH. In

Tab. 4.1 the main characteristics are summarized.

Parameter (by developer)	4X16F	5X114W
Chip size	3 mm × 3 mm	
Input coil inductance L_{in}	∼3 nH	∼2 nH
Input coupling M_{in}^{-1}	24.9 $\mu A/\Phi_0$	5.4 $\mu A/\Phi_0$
Feedback coupling M_f^{-1}	34.0 $\mu A/\Phi_0$	40.7 $\mu A/\Phi_0$
Noise level at 0.1 kHz	0.40 $\mu\Phi_0/Hz^{1/2}$	1.3 $\mu\Phi_0/Hz^{1/2}$
Noise level at 1 kHz	0.32 $\mu\Phi_0/Hz^{1/2}$	0.65 $\mu\Phi_0/Hz^{1/2}$
Noise level at 10 kHz	0.31 $\mu\Phi_0/Hz^{1/2}$	0.40 $\mu\Phi_0/Hz^{1/2}$
Noise level at 100 kHz	0.31 $\mu\Phi_0/Hz^{1/2}$	0.36 $\mu\Phi_0/Hz^{1/2}$

Table 4.1. Main properties of the PTB dc-SQUIDs: values are released at 4.2 K by PTB.

Both of them can be cooled down in the Earth magnetic field and are mounted directly in the Cu sample holder on the colder stage of the Dilution Refrigerator, without degradation in noise. The very small distance, between TES and dc-SQUID, allows to reduce the parasitic inductance effect of the wires.

The SQUID pads (9 for each channel, Fig. 4.7) are connected by Al wires bonding to Cu strips on a PCB board and via these to the connectors of the copper sample holder (Fig. 4.3). Three connector pins, for each channel, are used to join the TES with the SQUID and R_{bias}. All the 18 connectors are linked with the room temperature readout electronic by using copper–nickel alloy wires, of 200 μm thick and with $\sim$ 5 $\mu\Omega$·m resistivity at 300 K. The SQUID wires pass along the inner vacuum chamber (IVC) of the DR and thermalize at different cold points before arriving on the sample holder connectors: at 4 K stage, at the still level, through the heat exchanger and at the mixing chamber.

The signals from the XXF-1 electronics were addressed to a LeCroy 400 MHz digital oscilloscope, performing the data acquisition, first elaboration and storage. The SQUID room temperature readout electronic limits the achievable system bandwidth to about 6 MHz: this is enough for the response time of the TESs measured in this dissertation.

The standard method to operate the SQUID array amplifier is using a closed-loop constant-flux feedback system (FLL) [72]. Referring to Fig. 4.8, a voltage biasing is accomplished using a current source I_{bias} (typically from SQUID electronics) followed by a small cold bias resistor R_{bias} in parallel with the TES. In order to create a stiff voltage bias across the SQUID input coil and the TES sensor, R_{bias} should be much smaller than R_{tes}. Since the input coil is superconducting it has no dc voltage drop;

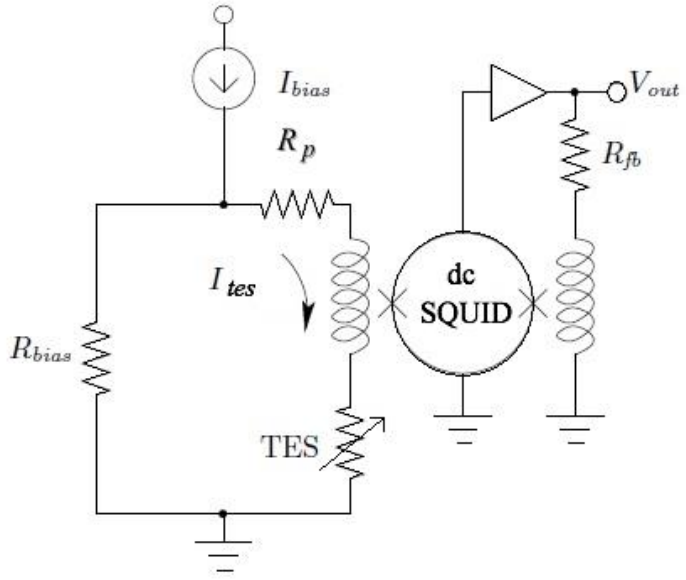

Figure 4.8. TES bias circuit with SQUID readout. I_{bias} is applied from XXF-1 room-temperature electronic and is shunted through a small R_{bias} to voltage bias the TES. The signal I_{tes} is read out using the 16-SQUID arrays or the two-stage sensors amplifiers run in flux-locked feedback mode through feedback resistor R_{fb}.

Fig. 4.9 shows an example of the oscilloscope's screenshot during the SQUID bias operation.

By running in flux-locked mode, the sensor current I_{tes} induces a flux through the SQUID via the input coil. The resulting voltage across the array is amplified and fed-back, by room-temperature electronics, through a feedback resistor R_{fb} to a feedback coil integrated on the SQUID chip.

This allows the linearization of the SQUID signal and an adjustable and calibrated gain (via selection of R_{fb}). Typically values of obtained amplification gain G are of hundreds thousand of V/A. To know the real amplification value we can proceed in several ways, in the following two methods are shown.

The first value to be calculated is the reciprocal of the mutual inductance[2] M_f^{-1} [75] in the feedback coil: it is expressed by the voltage for one period of the SQUID modulation (V_{period} of Fig. 4.9), divided by 1 V and multiplied by the peak-to-peak

[2] Theoretically, we could use the value dealt by the sensor developer, at 4.2 K, of Tab. 4.1: but since we worked at 40 mK we preferred to estimate the correct value, even if the difference is not so significant. The same appends for the input coupling value.

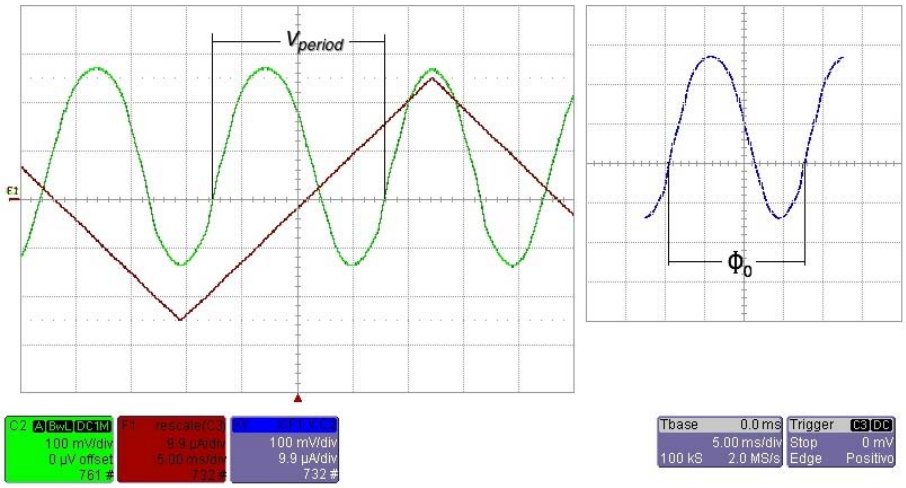

Figure 4.9. Oscilloscope's screenshot shows on the left the voltage across the dc-SQUID (V_{squid}, green line) for a triangular input signal (V_{bias}, red line); on the right V_{squid} as a function of V_{bias}.

value of the generator gives the current per flux quantum (I_{source}).
Imposing in the control software $I_{\text{source}} = (169.20 \pm 0.06)$ μV, we measured using the oscilloscope several values and after an average we had $V_{\text{period}} = (194.72 \pm 0.07)$ mV, in such away we estimate $M_f^{-1} = (32.9 \pm 0.5)$ μA/Φ_0.
Following a similar procedure, but giving current to the input coil, we are able to calculate the reciprocal of the mutual inductance $M_{in}^{-1} = (23.91 \pm 0.02)$ μA/Φ_0.

The SQUID amplification gain G, also know as trans-resistance, is derived by the formula [73]:

$$G = \frac{M_f^{-1} R_{fb}}{M_{in}^{-1}} \tag{4.2}$$

where R_{fb}, the feedback resistor, is chosen by the operator on the SQUID control software. In this case with $R_{fb} = (100.0 \pm 0.2) \times 10^3$ Ω, provided by the developer, we estimate $(G = 138 \pm 2) \times 10^3$ V/A.

A second way to have a value for G, is to close off the dc-SQUID on itself, i.e. without the TES mounted on the circuit of Fig. 4.8. After the SQUID has been biased by means of its software, we switch the SQUID to work in FLL mode. We supply a triangular I_{bias} and measure by the oscilloscope the voltage across the SQUID, V_{squid}: with $I_{\text{bias}} = (10.00 \pm 0.06)$ μA, a mean estimation gives $V_{\text{squid}} = (1.369 \pm 0.001)$ V.
The trans-resistance amplification factor results by the V_{squid} to I_{bias} ratio: (136900$\pm$ 83) V/A. In accordance with the previous G result, this latter one could appends

more accurate, but we have to consider that to proceed with this method we have to remove the TES by the circuit: so it is a measurement in a complete different experiment setup (and different cooling run), necessary to well characterize the SQUID amplifier. In fact we need this value to check up the SQUID's regular operation when it is mounted in the photon counting setup.

4.4 Laser Sources

A general scheme of experimental setup, applied for the measurements of Chap. 6.1 & 6.2 is reported in Fig. 4.10. A function generator is used to generate an electrical pulse to trigger the diode lasers used as photon sources. The light intensity is controlled by an optical attenuator connected to the detector through fiber optic patch cards.

The photon number discrimination measurements here presented cover, by four different wavelengths, the spectral range between visible and near infrared wavelengths: 406 nm, 690 nm, 1310 nm and 1570 nm. All these sources are pulsed diode lasers, but any other photon source can be employed, as the heralded single photon sources of Chap. 6.3.

List of applied laser sources:

⊙ Coherent CUBE diode laser system, $\lambda = 407$ nm, $\sigma_\lambda = \pm 5$ nm;

⊙ PPMT3109, $\lambda = 690$ nm, $\sigma_\lambda = \pm 5$ nm ;

⊙ NEC NDL7408P2, $\lambda = 1310$ nm, $\sigma_\lambda = \pm 2$ nm;

⊙ OCLARO LC 25WC157-AG, $\lambda = 1570$ nm, $\sigma_\lambda = \pm 4$ nm;

The optical attenuator box, reported in Fig. 4.10, summarizes a cascade of several attenuators. A calibrate Agilent 8156A allows to choose the different attenuations, in the range of $0 \div 60$ dB of the input power, with a 0.01 dB resolution at the telecommunications wavelengths ($1.25\ \mu\text{m} \div 1.60\ \mu\text{m}$). Before the 'TES detection system', two FC/APC connectors, with attenuation of 10 dB calibrated at 1.55 μm, are mounted.
Telecom sources (Fig. 4.11) are coupled with a beam splitter which divides the beam in two branches: the 90% of the beam continues through the next step to the TES, the 10% addresses to a fast semiconductor photodiode.

Infrared wavelength lasers are coupled with FC/APC covered optical fibers, with 9 μm of inner core, single mode at 1550 nm and 1310 nm. By using a calibrated optical power meter for telecom wavelengths, setting the attenuator at 0 dB, we

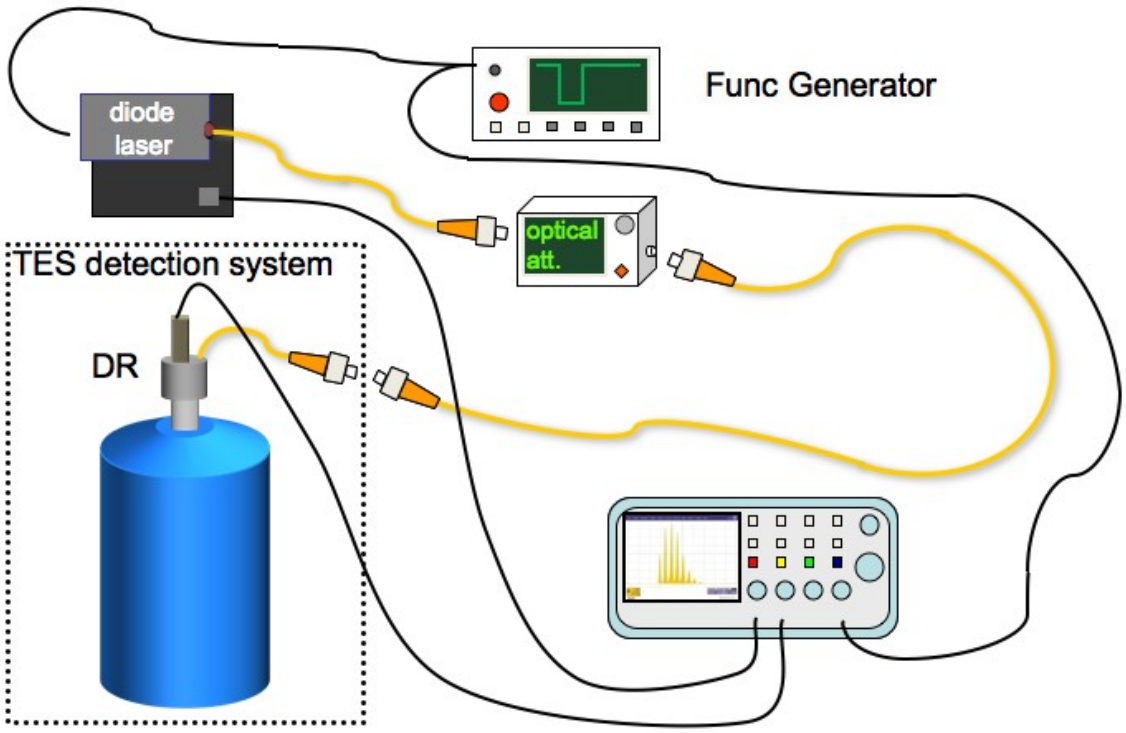

Figure 4.10. Laser source scheme.

estimate an overall attenuation of about 32 dB, from the laser to the 'TES detection system', due to fibers, connectors, beam splitter and attenuators.

The photodetector response signals represent the trigger for the LeCroy 400 MHz oscilloscope. In this way we could focus our attention on the temporal window where the TES response should be found.

The pulse shape to excite the laser is prompted by a function generator[3] which typically provides a pulse of 70 ÷ 90 ns width, with an amplitude of few Volts at repetition rate of ca. 10 kHz. A faster value is not necessary because of the slow response time of the device considered.

[3] An Agilent 33120A - 15 MHz Function/Arbitrary Waveform Generator.

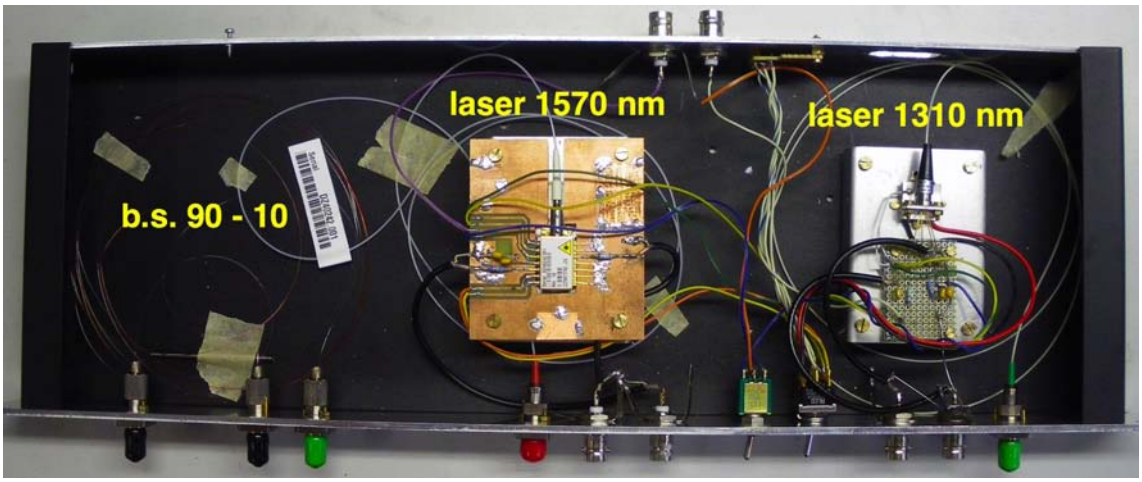

Figure 4.11. Hand made setup for telecom lasers and beam splitter.

Chapter 5

TES Details

5.1 TES Production

The research has been focused toward the development of transition-edge sensor microcalorimeters to discriminate radiation from visible to near-infrared. This device consists of a thin-film titanium/gold bilayer thermometer deposited on a silicon nitride substrate.

For the substrate, we use 500 μm thick layer of double polished Si wafers covered on both sides by 500 nm thick SiN layer grown by LPCVD; the nominal electrical resistivity is 50 Ω cm. Optical properties comparison, by using ellipsometric analysis, of this substrate with respect to one with different electrical resistivity, is shown in the appendix (see Chap. A).

Our microcalorimeters are deposited on top of the substrate in a Ultra High Vacuum film deposition systems [66, 76]. This system has a load lock for loading samples and a main chamber for electron beam deposition. The load lock is brought up to atmospheric pressure when samples are loaded into it. Then it is pumped down to 10^{-7} mbar. The sample surface is sputter-cleaned by ion gun system at an Ar pressure of 10^{-3} mbar for one minute. The main chamber is kept at lower pressure (10^{-9} mbar $\div$ 10^{-10} mbar), except during the deposition or when the sample is loaded. An e-flux Mini E-Beam Evaporator allows evaporation of small and small quantities of several materials in the temperature range of 400 K to 3100 K. A highly efficient watercooling system ensures negligible outgassing during operation and an integrated flux monitor allows maximum deposition control.
A coiled tungsten filament (ground potential) is placed in the immediate vicinity of an electrically conducting crucible or target (high positive potential) and provides electrons which are accelerated towards the evaporant rod (or crucible) producing extremely high heating-power densities. In our case, for the deposition of the Ti we use the rod and for the deposition of the Au we use the crucible.

Fig. 5.1 shows an example of the structure of TiAu TES film (not in scale): it consists of a first thinnest titanium layer (about 10 nm), then the gold layer ($\sim$ 45 nm) and, on top, the titanium layer (25 nm $\div$ 35 nm). In this way, the approximately final thickness of the films results in 80 nm $\div$ 90 nm. The first titanium deposition is necessary only to improve the adhesion between SiN substrate and the following gold layer.

Figure 5.1. TiAu film on SiN substrate.

After the deposition of the thin films, the area of the TES and its wiring are defined by means of photolithographic processes. A photoresist, a mixture of an organic polymer and a photosensible compound, is applied on the surface of the sample using a spin-coating. This coating is selectively irradiated with UV light through a positive photolitographic mask, transmitting the light only in the desired regions. The light causes a chemical changing in the irradiated photoresist and it reacts with a chemical substance called developer. To remove the Ti we use H_2O : HF : H_2O_2 and to remove Au we use KI/I_2. At the end of the process, on the silicon nitride substrate we obtain the area of the TES covered by the remained photoresist. The area of the TES masks can be both 20 μm $\times$ 20 μm and 10 μm $\times$ 10 μm.
To define the Al wirings of the TES, we use a photolithographic lift-off process to avoid a chemical etching which could damage the TES film. The Aluminum layer are deposited on the sample through a photoresist stencil in a RF magnetron sputtering system, at the base pressure of about 2×10^{-7} mbar.
Before the deposition, the titanium/gold layer is cleaned by light sputter etching to remove natural oxide and impurities. This step is a fundamental process to prevent residual resistances between TES area and Al wirings. The Al film is deposited at rate of 1 nm/s, at Ar pressure ranging from 5×10^{-3} to 2×10^{-2} mbar and at RF voltage of 1 kV. The typical Al thickness is 100 to 150 nm checked by a profilometer.

At the end of this process, the sample is placed in acetone bath to dissolve the photoresist. The metal that is deposited on top of the photoresist flakes off, but the metal that is deposited directly on the substrate sticks to the surface. Thus, the lift-off process leaves the film (TES and wiring) on the surface of the substrate with the same shape as the pattern on the masks.

After the deposition of the thin films, photolithographic processes, sputtering of

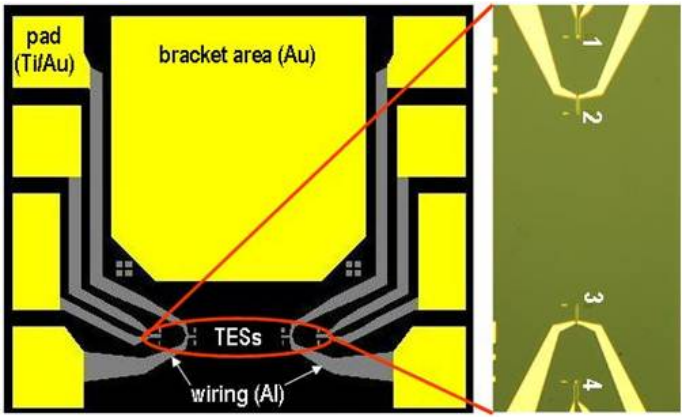

Figure 5.2. On the left a picture of a TES chip is reported. On the right there is a TES magnification where TES 1 and 4 have the same area, 20 μm $\times$ 20 μm, while TES 2 and 3 are 10 μm $\times$ 10 μm. The distance between TES 1 and 4 is 2250 μm and the one between TES 2 and 3 is 1250 μm.

the aluminum, to create the wirings, and the lift-off process, the device is ready: a picture of the complete TES chip is shown in Fig. 5.2 (left).
On the TES chip (typically dimension of 2 cm $\times$ 1 cm) there are four separated TESs, with respective wires and pads, a test strip, made during the deposition process of the sensors, and a wide gold pad, to allow the fiber optics positioning on the sensor (see section 4.2). Fig. 5.3 shows two magnifications of the TESs area: the outer sensors (number 1 and 4) have the same active area of 20 μm $\times$ 20 μm, while the inner ones (number 2 and 3) are 10 μm $\times$ 10 μm. The distance between TES 1 and 4 is 2250 μm, between TES 2 and 3 is 1250 μm and between the number 1 and 3 (or 2 and 4) is 1750 μm.

At the end of this long production process, the critical temperature characterization is the first check to know the properties of the new TESs. The transition temperature from the superconducting to normal phase is obtained measuring the TES electrical resistance, at constant current by the four–wires technique, changing the device temperature.

The resistance ($R_{\rm tes}$) curve as function of temperature (T) for the 20 $\times$ 20 μm^2 active area TES, characterized in the following chapters, is shown in Fig. 5.4. The curve has been obtained with a constant sinusoidal current of 0.5 μA applied to the TES.
This sample, that for simplicity we will call TIC, shows a critical temperature $T_c \approx$ 121 mK, a transition width of $\Delta T_c \approx$ 2 mK and a normal resistance of $R_n \approx$ 0.220 Ω.

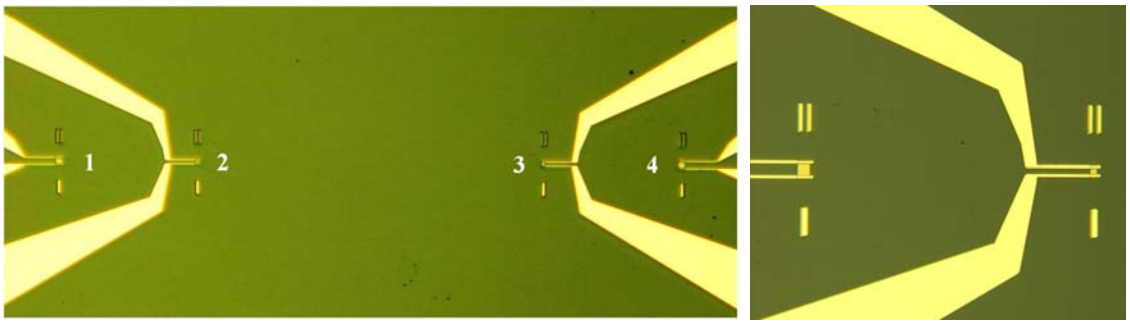

Figure 5.3. Optical microscope pictures of the TES region. On the left, four TESs: the distance between TES 1 and 4 is 2250 μm and between TES 2 and 3 it is 1250 μm. On the bottom, magnification of TES 1, 20 $\times$ 20 μm^2 area, and TES 2, 10 $\times$ 10 μm^2 area.

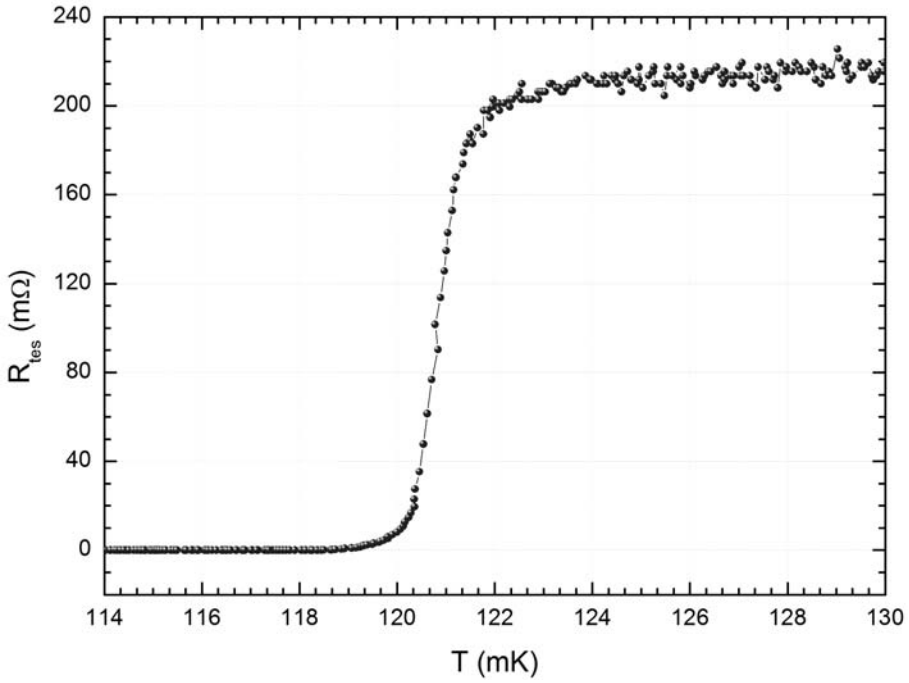

Figure 5.4. TIC critical temperature curve: R_{tes} vs. T [77].

T_c value has been obtained looking at the temperature value corresponding to half R_n, while ΔT_c is the temperature width defined between the 10% and the 90% of R_n; for more details about this measurements we refer to [66].

5.2 Working Point

Fig. 5.5 shows a typical TES-bias current curve of TIC device. When the TES is superconducting the sensor current (I_{tes}) changes rapidly with the applied bias current (I_{bias}) since it is limited only by the parasitic lead resistance (< 1 mΩ for this mounting). When I_{bias} increases and the sensor critical-current (~ 40 μA) is exceeded, the sensor jumps into a resistive state. If I_{bias} is further increased the sensor becomes completely normal ($R_{\mathrm{n}} \sim 220$ μA, for this particular film).

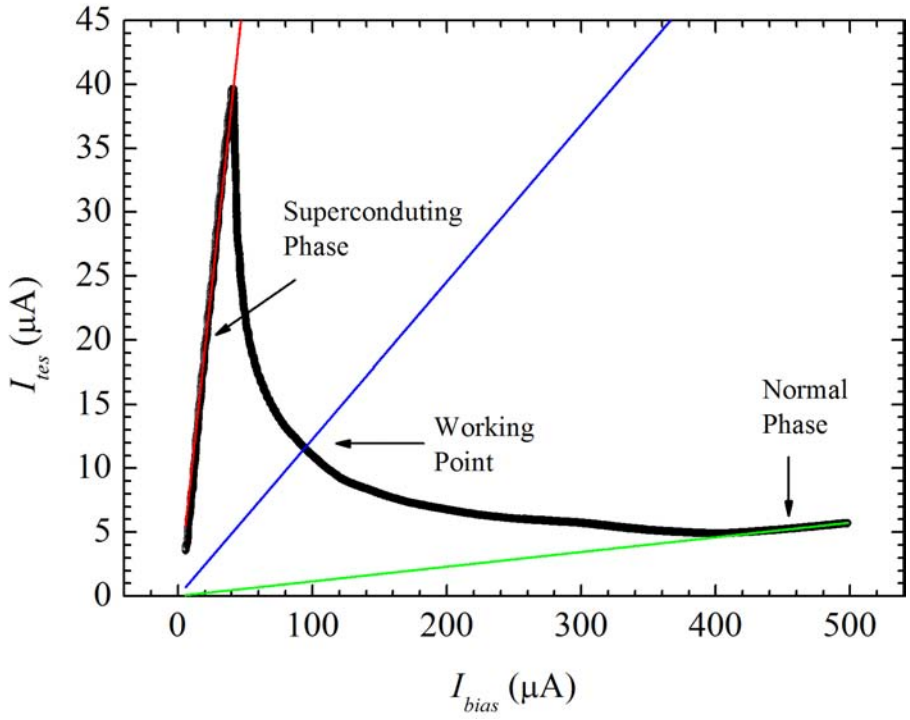

Figure 5.5. TIC bias curve I_{tes} vs. I_{bias} [77]. Red straight line indicates the parasitic lead resistance, less than 1 mΩ, blue straight line the 17 mΩ resistance, corresponding to the working point into the transition region, and the green one the 220 mΩ resistance of the normal phase.

When the sensor is normal, it dissipates power. In this phase, the power dissipation P_d is quadratic in V_{bias} since R_{tes} is constant: $P_d = V_{\mathrm{bias}}^2/R_{\mathrm{tes}}$, where V_{bias} is the voltage across R_{bias} in Fig. 4.8. When the bias voltage is reduced, the sensor enters the superconducting–to–normal transition and the power dissipation becomes constant and independent of I_{bias}. In this phase the sensor resistance is quadratic in V_{bias}: $R_{\mathrm{tes}} = V_{\mathrm{bias}}^2/P_d$. When the bias is further reduced, eventually the sensor resistance becomes comparable in value to R_{bias} until it snaps into the superconducting

state.

Into the transition region, the working point is chosen to optimize the discrimination of photons. To be in a strong electrothermal feedback (Sec. 3.2), where both the effective response and the sensibility of the TES are high, the best condition is when the bath temperature is well below the temperature of the microcalorimeter ($\lesssim T_c/2$).
Since this thermal conditions and considering TIC T_c shown in Fig. 5.4, the dilution refrigerator temperature has been stabilized across 40 mK.

The operating resistance has been chosen as a compromise between the demand for a large value of the parameter $\alpha = (T_0/R_0)(\Delta R/\Delta T)$ and the demand for the voltage bias. With a bias current $I_{\text{bias}} = 95$ μA, a bias resistance $R_{\text{bias}} = 2.38$ mΩ, the choice resulted in the R_0 resistance equal to 17 mΩ ($\sim 8\%$ on R_n).

5.3 Photon Absorption

Once the detector is regulated at the operating point, as previously described and all the unnecessary equipment is disconnected from the dilution refrigerator, the microcalorimeter is exposed to the visible-NIR light.

The electromagnetic radiation comes from the sources described in Chap. 4.4 coupled to a 9 μm core optical fiber, single mode for telecom wavelengths. Before entering the DR, the laser light intensity is reduced to the single photon emission regime, regulating the optical attenuator and mounting some attenuator filters. The optical fiber enters the DR and it is rolled up around the 4 K cold stage. Here the entering fiber is connected to the one coming from the alignment system (Chap. 4.2). This latter one have a smaller cover and it is thermalized around the still, the heat exchanger and the mixing chamber, ending over the TES.

As explained in Chap. 3.2, when a photon impinges the TES surface, the microcalorimeter temperature (maintained in the superconducting phase) increases because of the absorption of the incident energy, with a consequent increment of the its electrical resistance. In the small signal limit approximations, valid for small temperature excursions in which the change in sensor resistance is small if compared with the normal resistance, the current sensor I_{tes} results in a pulse proportional to the incident photon energy. The TES current variation is amplified and converted in a voltage signal ($V_{\text{tes}} \propto G \cdot I_{\text{tes}}$, see Chap. 4.3) by the the SQUID, and red out by the digital oscilloscope.

Fig. 5.6 shows an oscilloscope screenshot of the SQUID signal, in the photon counting regime. The signal coming from the laser photodector (or from the function generator, see Fig. 4.10) triggers the oscilloscope, top trace of the figure. The bottom trace of the same figure is the TES signal, where in the pulse shape is recognizable

both the exponential decay and the rise behavior.

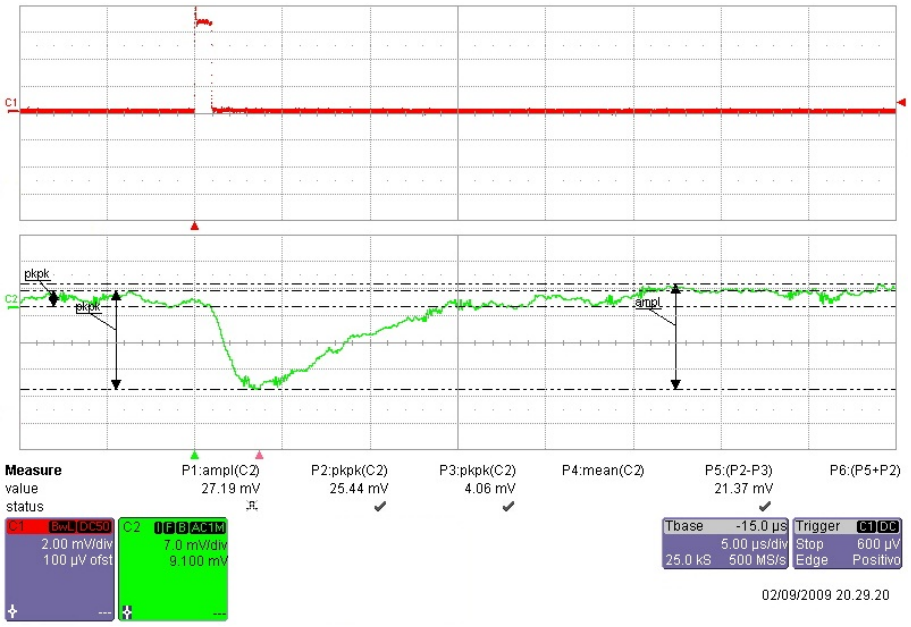

Figure 5.6. Oscilloscope display during the acquisition of V_{tes}: on the top, the photodetector trigger signal from the laser source (red line); on the bottom, the TES signal in photon counting regime (green line) from the SQUID electronics.

Looking at the oscilloscope display, set in this configuration, how many photons are detected and eventually if the TES is working as a bolometric detector or as a calorimetric one is not easily understandable. Of course, an off–line analyses of the acquired pulses provides the accurate information needed to have a qualitative and accurate characterization of the detector. In the next Chapter 6 we will explain how do to it, here we show just a quick way to obtain quantitative information of the TES behavior.

If the irradiated TES works as a photon number resolving detector, on the oscilloscope display, set in 'persistence mode', one can watch a pictures as in Fig. 5.7. By this digital function, the oscilloscope superimposes all the waveforms marking with the same colors the regions where the probability to find the signals is the same: for instance, looking at Fig. 5.7, most of signals through the red region and moving to blue/violet regions the number of waveforms decreases.

Fig. 5.7 is a clear example of a TES works as microcalorimeter in photon counting regime. In both cases the baseline trace is easily distinguishable, generated when no photons hit the TES, and the trace lived by the waveforms of the single photon detection. In the (b) case, one can observe the trace of two photons absorbed at the

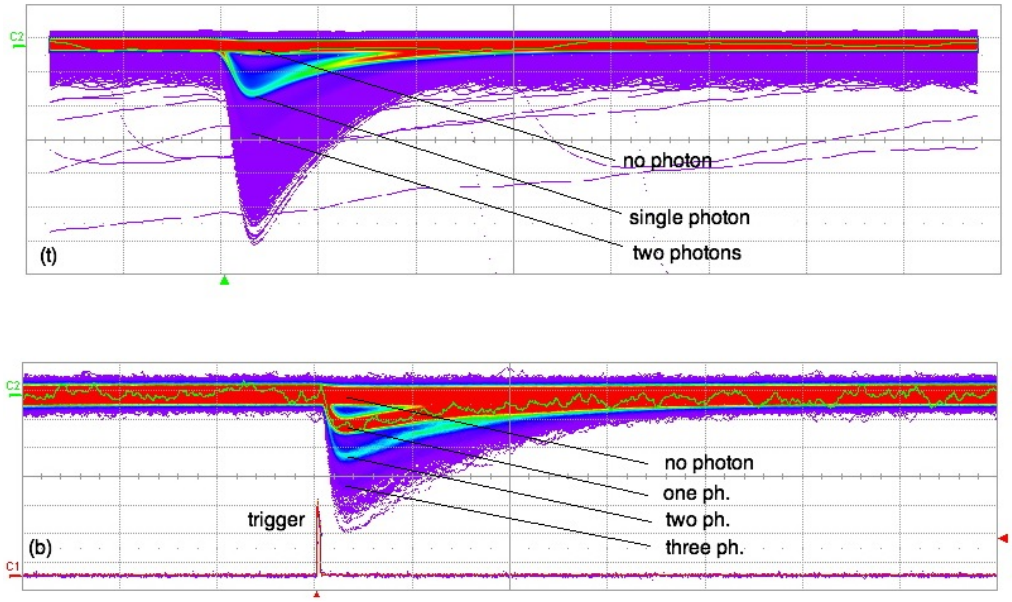

Figure 5.7. Oscilloscope screenshot in persistence representation of a TES in photon counting regime. In (t) case, one can observe the discrimination among the no photon detected waveform, the single photon state and of two photons. In the (b) case, discrimination of the states is up to three photon; also the trigger trace is appreciable.

same time. With some difficulties, the traces of two photons, in (t) case, and three photons, in (b) case, are recognizable too.

Theoretically, the regions between the traces of photon states should be white, i.e. no waveforms should pass through those regions: this is obviously and due to the quantum behavior of the incident light in the photon regime. The presence of waveforms, in those forbidden regions, is the demonstration that the detector is not ideal and the signals to noise ratio is a main theme in the data analyses, that we are going to take into consideration (Chap. 6.1.1).

Linked to this theme is the TES energy resolution, i.e. the detector capability to discriminate the absorbed energy. A fast idea to assess this capability comes from looking at the width of the traces: as the photon state traces are thinner as the TES resolved energy is lower. At the same time, if the waveform number into forbidden region increases, the energy resolution worsens. However, this level of precision is not sufficient to calculate any signals feature and this result is available only in the case the oscilloscope has been preprogrammed to do so. For this reason, since the distribution of the signal amplitude, inside a photon state, follows a gaussian statistics (because of the central limit theorem), it is common knowledge to link the energy resolution to the width of amplitude distribution for the single photon state

[36].

Giving a series of marker to delimit where it is possible to find the trace baseline (mean) and minimum, the digital oscilloscope is able to build the amplitude histogram of Fig. 5.8. Every peak represents the mean amplitude value of the carried photons. Signals carrying no photons can be considered as pure noise, however, since their values are different from a flat line (fixed to 0 mV), their amplitude is distributed around a 0 peak higher than 0 mV. All the peaks follow a Poisson distribution, in according to the emittance of a coherence light source.

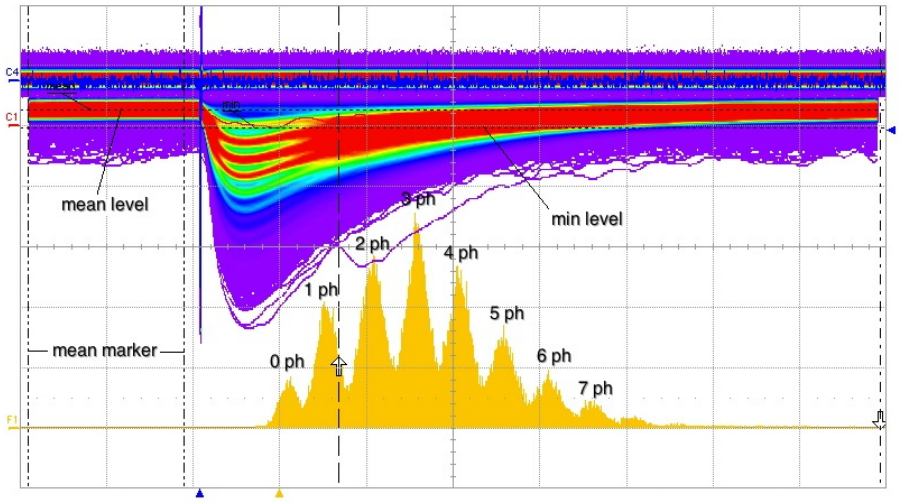

Figure 5.8. Oscilloscope's display during a photon counting acquisition: the screenshot shows the persistence mode superimposing on the corresponding amplitude histogram. The mean (baseline) level and the marker inside the oscilloscope calculates it and minimum waveform level are shown.

Alternatively, to estimate the amplitude of every acquired signal it is necessary to define a baseline as a reference for the measurement [78]. Since these waveforms are triggered, we know when a photon can be detected and, when the trigger fires, time starts from 0 s. Therefore, the signal samples with negative time values represent the baseline, the mean or the noise, because the time interval between two consecutive events has been set long enough to let every previous detected photon to extinguish its tail.

Considering Gaussian the distribution into each photon state and that the baseline can be calculated as the mean of all samples before the trigger (with negative time values), then we can estimate the amplitude of the waveform as the absolute difference between the noisy signal minimum and the baseline. This will be the procedure we are going to use in the data analyses of the next Chapter.

Part III

the prestige

Chapter 6

Photon Number Discrimination

An interesting application of photon detectors is quantum cryptography. Secure systems require detector with single photon sensitivity at telecommunication wavelengths ($\sim$ 1.5 μm) and very low dark counts. Both of these characteristics can be provided by calorimeters designed to operate at visible and near-infrared photon wavelengths.

In this chapter, I present the experimental results from my Ph. D. work: starting with results on TiAu TES discriminates photons at a single wavelength, then there will be shown a wide range of wavelengths to which this kind of calorimeters is sensible; full quantum calibration of the detector is also reported.

6.1 Telecom Wavelength Photon Detection

As already explained in section 5.3 when a photon is absorbed by TES, the device resistance moves from the working point to a higher value proportionally to the incident photon energy E_γ. Consequently a sudden decrease in $I_{\rm tes}$ occurs with an electrical time constant $\tau_{\rm el}$, due to the passive element of the bias circuit (see Fig. 4.8). After photon absorption, the resistance value relaxes to the bias working point with an effective time constant $\tau_{\rm eff}$.

Fig. 6.1 shows this behavior for a triggered single photon noisy signal, obtained irradiating the sample called TIC and acquired by using the LeCroy 44Xi-A WaveRunner oscilloscope. TIC (already presented in chapter 5) is a 20×20 μm^2 TiAu TES, with a critical temperature $T_c \sim 121$ mK and transition width $\Delta T_c \sim 2$ mK. The oscilloscope was setup to show 100 mV full scale (10 mV/div) along the y-axes and 60 μs full scale (10 μs/div) along the x-axes: in this configuration the oscilloscope accuracies are $o_{s,y} = 1.5 \times 10^{-2}$ of the full scale and $o_{s,x} = 10 \times 10^{-6}$ of the read value.

Fig. 6.2 (red line) shows the single photon pulse response, for the same dataset

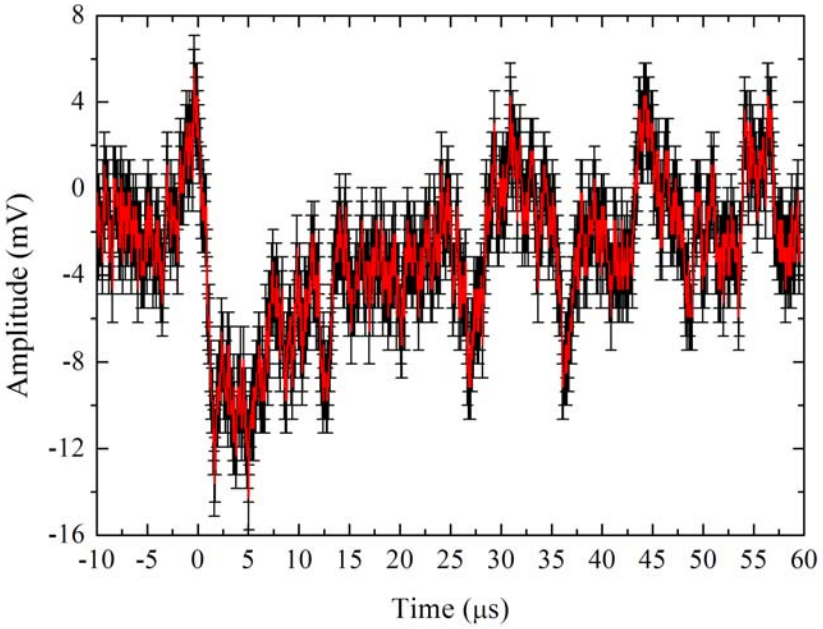

Figure 6.1. Noisy single photon signal at 1570 nm: error bar in black.

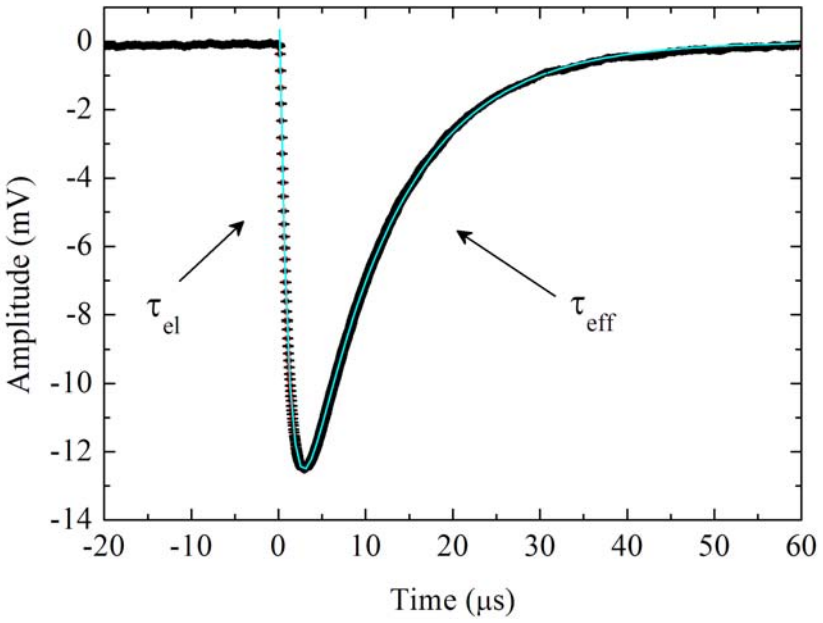

Figure 6.2. Averaged single photon signal (red), at 1570 nm; fit of the pulse (blue) to estimate $\tau_{\mathrm{el}} = (1.106 \pm 0.003)\ \mu$s and $\tau_{\mathrm{eff}} = (10.228 \pm 0.009)\ \mu$s.

from which the pulse of Fig. 6.1 is extracted, averaged over $N = 15480$ acquired signals. This mean pulse is fitted (blue line) by the double exponential function

$$y_{\text{fit}} = A_1 e^{-(t-t_0)/\tau_{\text{el}}} + A_2 e^{-(t-t_0)/\tau_{\text{eff}}} \tag{6.1}$$

where A_1 and A_2 are constant parameters, obtaining for $\tau_{\text{el}} = (1.106 \pm 0.003)$ μs and for $\tau_{\text{eff}} = (10.228 \pm 0.009)$ μs. The uncertainty over these numbers is mainly given by the fit, because the one introduced by the oscilloscope is negligible ($o_{s,x}/\sqrt{N}$).

Other samples have shown lower values [79] both for the rise time ($\tau_{\text{el}} \sim 0.2$ μs) and for effective time ($\tau_{\text{eff}} \sim 3$ μs) constant. This can probably be explained in terms of different bias working points, device critical temperatures and bath temperatures. Nevertheless TIC has an other important property shown below.

For this acquisition, the photon source was the Oclaro LC25WC 157AG-J34 diode laser, at 1570 nm wavelength, pulsed at 9 kHz of repetition rate with a pulse width of 70 ns, well below the response time of our detector, and optically attenuated of 33 dB (see section 4.4): this corresponds to address to the detector, a mean optical power of ~ 36 fW.
The response pulses of TIC, for this incident radiation, are shown in Fig. 6.3, where the averaged traces of up to 6 detected photons are plotted. The first trace (of single event) is the same shown in Fig. 6.2.

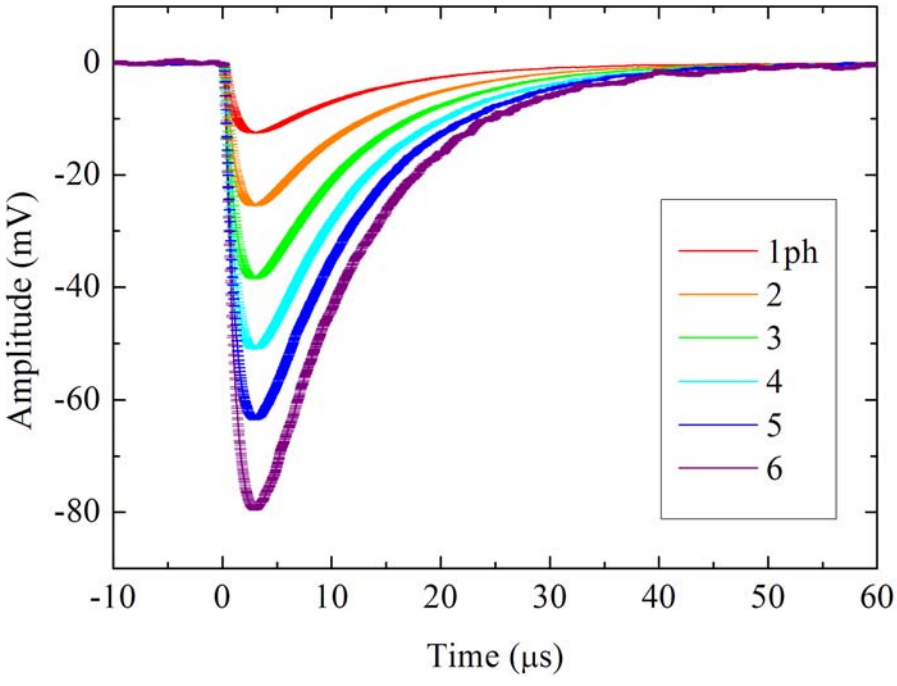

Figure 6.3. Averaged signals of 6 detected photons, at 1570 nm.

To obtain the averaged pulses of this acquisition we started from 50000 traces of triggered noisy pulses monitored and saved in a binary format by means of the digital oscilloscope, without any kind of filtering. In general a collection of pulses of the order of tens of thousands or more traces are typically saved for different experimental conditions, i.e. wavelengths, light intensity and bias point.

Then an off-line analysis of the traces is necessary to improve the most important TES waveform features: the averaging signals were obtained by means of a cross-correlation technique [78]. Here we present the results of an analysis that aims on the single pulse to: obtain the amplitude histogram, estimate the energy resolution (ΔE_γ) and its uncertainty and calculate single photon energy on real signals.

In Chap. 5.3 we have already introduce two methods to build the amplitude histogram. In one case by the oscilloscope, which finds the trace's baseline and minimum in definite regions, and in the other one, considering the triggered waveforms. By this latter condition, we are able to estimate the baseline as the mean of all sample before the trigger (with negative time values) and to build the amplitude histogram as the absolute difference between the noisy signal minimum and the baseline. Applying this amplitude estimation procedure to the entire dataset, from which we have extrapolated previous figures, we have obtained the graph in Fig. 6.4.

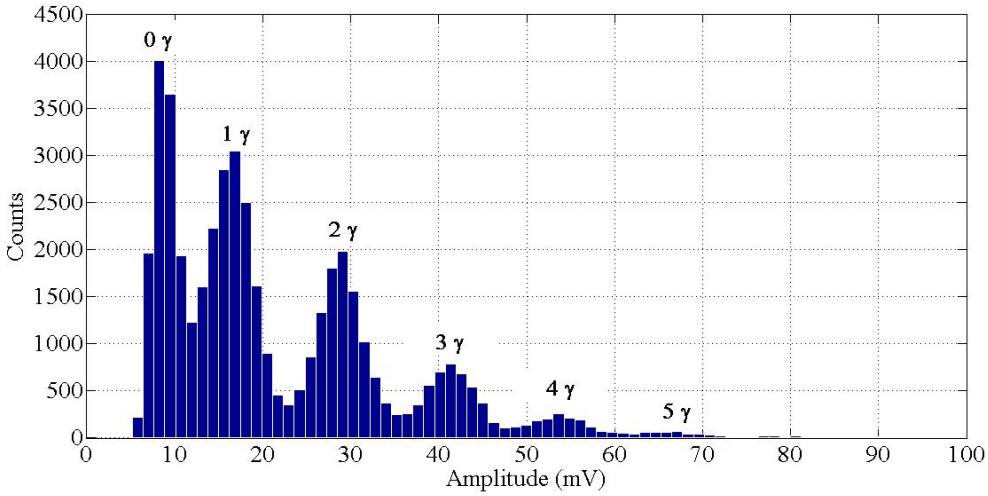

Figure 6.4. TIC noisy signals amplitude histogram and carried photon relating to the count of Fig. 6.2, at 1570 nm wavelength.

6.1.1 Wiener Filtering

The Signal to Noise Ratio (SNR) is a measure that can be used to evaluate the capability of a filter to reduce noise components in a measured signal: as the ratio is higher, as the signal features extraction is easier. Considering that the TES signal is mainly affected by Johnson and phonon noise, a filtering technique is necessary to significantly enhance the most important properties in trigged TES acquisitions, as the energy resolution or to reduce the peak tails superposition in amplitude histograms [82].

Fig. 6.5 reports the histogram based on the same waveforms of Fig. 6.4 after the Wiener filtering. The 0 γ peak has been isolated and neglected using the cross-correlation information. Qualitatively, the differences with respect to the correspondent noisy histogram is evident: now between two consecutive peaks, the counts go to (or closer to) zero, i.e. the peak full widths at half maximum are smaller; as a consequence, the six photon state counts are visible too, while in Fig. 6.4 data, it remained not distinguishable from noisy signals.

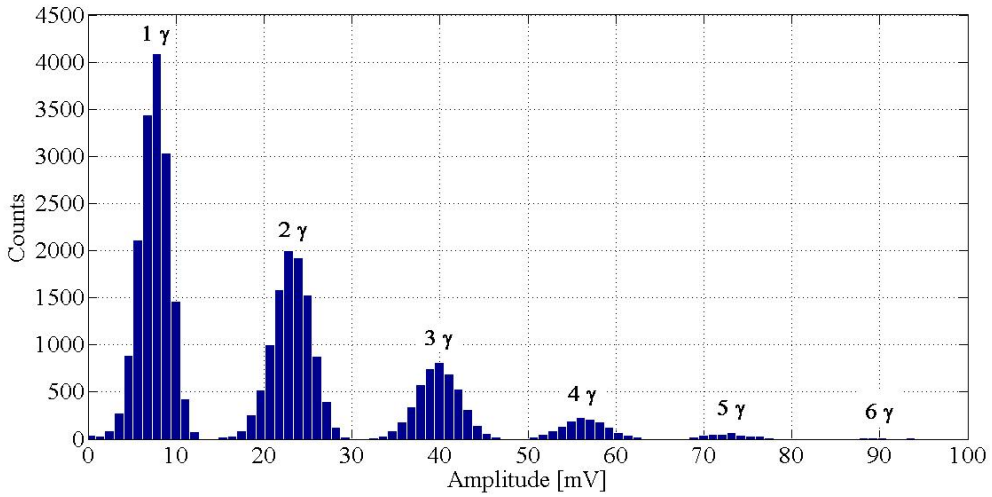

Figure 6.5. TIC Wiener filtered signals amplitude histogram, relating to the count of Fig. 6.4.

Wiener filter is also called the optimal filter in the sense that the filtered output is as close to the original signal as possible, as measured by a least-squares criteria [80]. This filter uses the frequency spectra information to separate the signals. Typically, the signal-to-noise ratio is higher at some frequencies than at others. In the same manner, noise will dominate at other frequencies. The Wiener filter estimates the true signal by assigning a frequency dependent gain that depends on the relative amount of signal and noise and then least-square fitting.

The basic assumption of the Wiener filter is that the signal and noise are stochastic, i.e. they should be uncorrelated.
For the noise, this means that it must be random and stationary in time. This is not a well assumption, as Johnson noise is dependent on the varying resistance of the TES.
For the signal, this means that the detector response is linear with incident photon energy. This condition will be met in Chaps. 6.1.3 & 6.2 and it is discussed in [81]. So all detector pulses could be assumed proportional to a template pulse shape.

More details and an accurate study on both Wiener and Savitzky-Golay filtering procedure are reported in the Ph. D. thesis work [78] of Dr. D. Alberto, who, collaborating with our group, also developed the software to apply the Wiener procedure to our data. For this reason here I considered the optimal filtering process only as a tool of analysis.

Other results are reported in [82], where we analysed different kinds of digital filters to improve the TES energy resolution. Taking into account both time-domain and frequency-domain analysis, we obtained that both the Savitzky-Golay and Wiener filtering elaboration reduce the noise components. Savitzky-Golay filter is a low pass filter that works very well in noise reduction preserving peak amplitude information, while Wiener filter is able to optimize the SNR of every pulse signal waveform. Fig. 6.6 reports a comparison between a noisy signal, a Savitzky-Golay and a Wiener filtered outputs, extracted from the same dataset we are analyzing in this chapter.

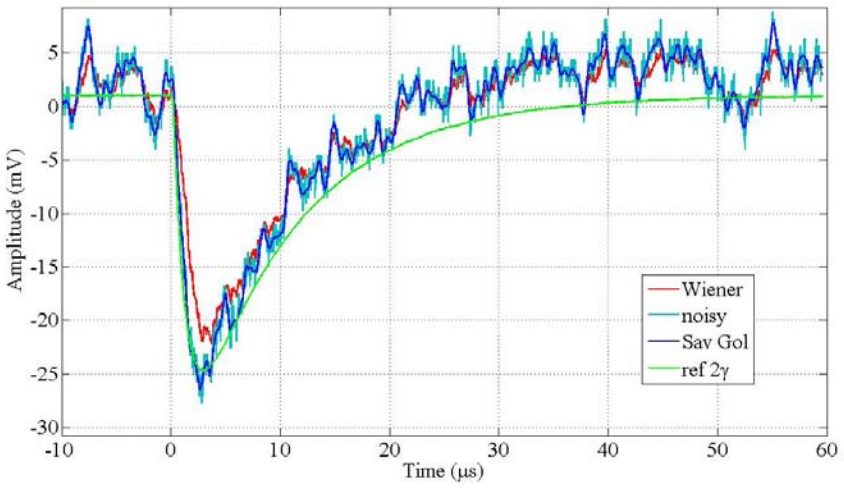

Figure 6.6. Example of two photons response pulse obtained with TIC TES noisy signal (cian), reference signal (green), SG (blue) and Wiener (red) filteres outputs, at 1570 nm.

In a TES signal detection, another important feature is the time jitter. It has been calculated as the time fluctuation (RMS) of time values at half amplitude in a sub-set of waveforms carrying the same number of photons. From the results presented in [82] we concluded that neither Savitzky-Golay nor Wiener reduce the time jitter and that, fixed the filter, the time jitter estimate is only sensitive to the SNR.

However the main advantage that allows to choose one filtering process with respect to the others is that the Wiener elaboration is able to gain up to a factor 2 in the energy resolution [78, 82]. The energy resolution can be calculated from the Wiener filtered signals amplitude histogram.

6.1.2 Energy Resolution

The laser light emission process has fluctuations that can generally be modelized using Poisson distribution, while the signal detection has normal distribution [81]. Therefore we process histogram data (Fig. 6.4) with fit equation that consider a Gaussian function for each peak and a Poissonian trend for the amplitude peaks [79]:

$$y_{\text{fit}} = \frac{Ae^{-\mu}}{\sqrt{2\pi\sigma^2}} \left[exp\left(-\frac{(x-x_0)^2}{2\sigma_0^2} \right) \frac{\sigma}{\sigma_0} + \sum_{i=1}^{n} \frac{\mu^i}{i!} exp\left(-\frac{(x-x_i)^2}{2\sigma^2} \right) \right] \tag{6.2}$$

A constant standard deviation σ for each peak is assumed, except for the first one (0γ) in which we use an appropriate spread (σ_0), corresponding to the case of no-photon detected. A is a normalization factor, μ is the average number of photons detected per pulse of incident light, i is the number of absorbed photons that generate the signal centered on amplitude equal to x_i; the no-photons detected amplitude is obviously x_0.

The free variables to be estimated by the fit are: the mean peak values x_0 and x_i, the normalization factor, A, the average number of detected photons, μ, and the standard deviations, σ_0 and σ. By using this procedure I obtained the plot of Fig. 6.7: Tab 6.1 shows the results of fit procedure.

All mean peak values could be calculated using histogram data and introduced in a fitting program to reduce the free variables to be estimated. Since the importance of this variable in the energy resolution estimation, I preferred using the histogram value only to initialize the fitting program.

In the cases of fitting Wiener histogram data, as in Fig. 6.5, the first exponential of previous equation, related to no carried photons (0γ), is not considered: the first peak of Fig. 6.8 is related to the single photon detected (1γ), while the 0γ

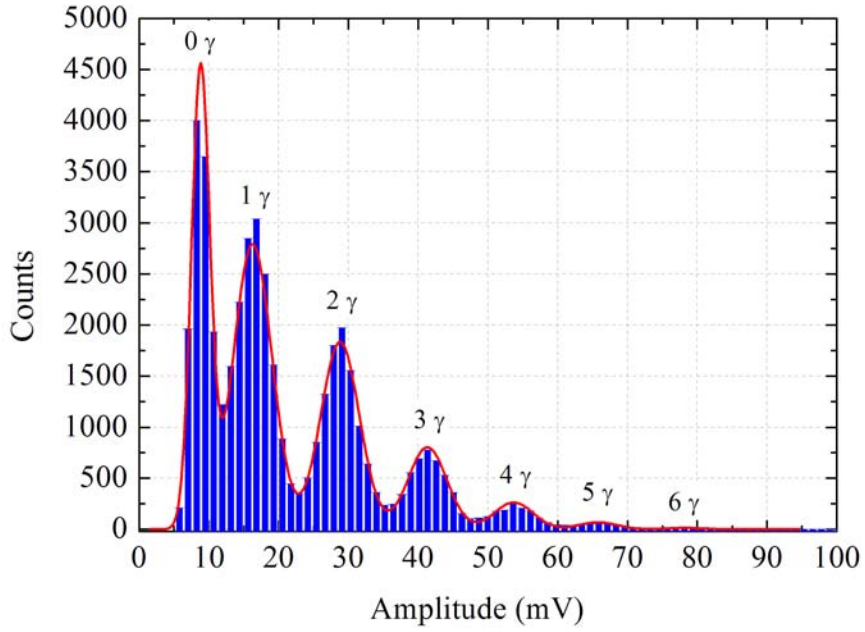

Figure 6.7. Fit over TIC noisy signals amplitude histogram. The energy resolution results ΔE= (0.411±0.006) eV over the single photon of energy $E_\gamma \sim 0.798$ eV. Column bars are plotted with statistical error bars.

histogram bars have been isolated and neglected as described in section 6.1.1. Fit variable estimation is shown in Tab 6.1.

The peak standard deviation σ is related to the energy resolution at Full Width at Half Maximum (ΔE) by the equation:

$$\Delta E = 2\sqrt{2ln2}\ \frac{\sigma E_\lambda}{x_2 - x_1} \tag{6.3}$$

where E_λ, the energy of the incident photon, is equal to 0.789 eV (1570 nm) for the presented dataset, and denominator is the amplitude distance between the first two peaks, representing signals carrying 2 and 1 photons, respectively.

Propagating errors on the ΔE formula, we estimate the uncertainty on the Energy Resolution. Expressing the energy of the incident photon in term of light speed in vacuum c, Planck constant h, laser source wavelength λ and eV energy unit (conversion factor ϵ),

$$E_\lambda = \frac{c\ h}{\lambda\ \epsilon} \tag{6.4}$$

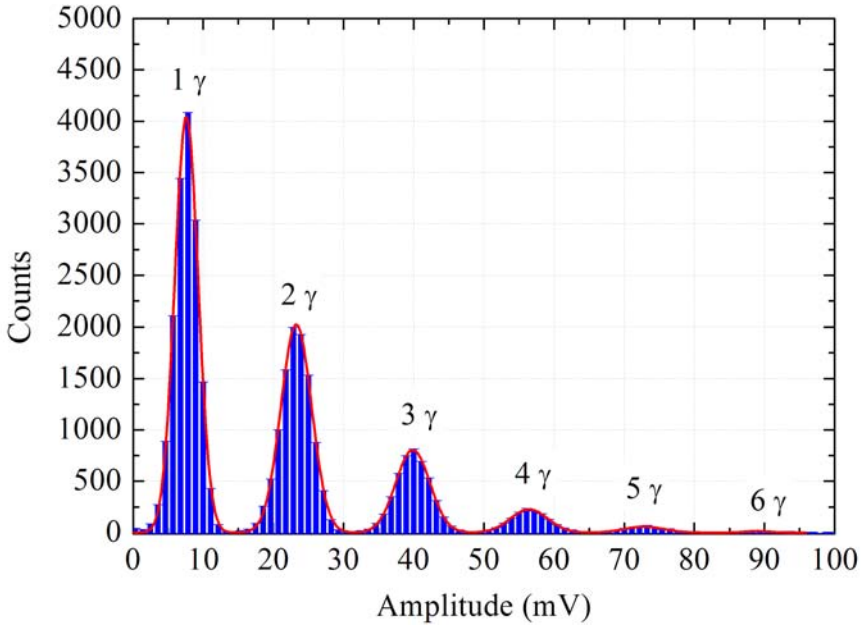

Figure 6.8. Fit over TIC Wiener filtered signals amplitude histogram. The 0γ peak has been isolated and neglected using the cross-correlation information. $\Delta E=$ (0.201 ± 0.003) eV over the single photon of energy $E_\gamma \sim 0.789$ eV. Column bars are shown with statistical error bars.

	Noisy	Wiener
A	$(54.9 \pm 0.6) \times 10^3$	$(70.3 \pm 0.5) \times 10^3$
μ	1.314 ± 0.014	1.25 ± 0.04
x_0 (mV)	8.81 ± 0.03	
x_1 (mV)	16.27 ± 0.07	7.51 ± 0.03
x_2 (mV)	28.80 ± 0.07	23.12 ± 0.05
x_3 (mV)	41.32 ± 0.12	39.80 ± 0.08
x_4 (mV)	53.7 ± 0.2	56.38 ± 0.17
x_5 (mV)	65.8 ± 0.4	72.7 ± 0.3
x_6 (mV)	78.2 ± 0.8	90.0 ± 0.8
σ_0 (mV)	1.31 ± 0.03	
σ (mV)	2.77 ± 0.03	1.71 ± 0.02
χ^2	6.2	5.3

Table 6.1. Fit results over noisy (Fig. 6.7) and Wiener (Fig. 6.8) histogram data. The reduced χ^2, the sum of the square of the residuals divided by the degree of freedom, is used to evaluate the goodness of the fit.

Eq. 6.3 can be rewritten as:

$$\Delta E = \frac{c\ h}{\lambda\ \epsilon} \cdot \frac{\varsigma}{x_2 - x_1} \tag{6.5}$$

where $\varsigma = 2\sqrt{2ln2} \cdot \sigma$ is the Full Width at Half Maximum.
On this equation we propagate the error obtaining for the square uncertainty of ΔE:

$$\begin{aligned}
\sigma^2_{\Delta \mathrm{E}} = & \left|\tfrac{\partial \Delta E}{\partial c}\right|^2 \sigma_c^2 + \left|\tfrac{\partial \Delta E}{\partial h}\right|^2 \sigma_h^2 + \left|\tfrac{\partial \Delta E}{\partial \lambda}\right|^2 \sigma_\lambda^2 + \\
+ & \left|\tfrac{\partial \Delta E}{\partial \epsilon}\right|^2 \sigma_\epsilon^2 + \left|\tfrac{\partial \Delta E}{\partial \varsigma}\right|^2 \sigma_\varsigma^2 + \left|\tfrac{\partial \Delta E}{\partial x_2}\right|^2 \sigma_{x_2}^2 + \left|\tfrac{\partial \Delta E}{\partial x_1}\right|^2 \sigma_{x_1}^2 \\
= & \left|\tfrac{E_\lambda\ \varsigma}{c\ (x_2 - x_1)}\right|^2 \sigma_c^2 + \left|\tfrac{E_\lambda\ \varsigma}{h\ (x_2 - x_1)}\right|^2 \sigma_h^2 + \left|-\tfrac{E_\lambda\ \varsigma}{\lambda\ (x_2 - x_1)}\right|^2 \sigma_\lambda^2 + \\
+ & \left|-\tfrac{E_\lambda\ \varsigma}{\epsilon\ (x_2 - x_1)}\right|^2 \sigma_\epsilon^2 + \left|\tfrac{E_\lambda}{x_2 - x_1}\right|^2 \sigma_\varsigma^2 + \left|-\tfrac{E_\lambda\ \varsigma}{(x_2 - x_1)^2}\right|^2 \sigma_{x_2}^2 + \\
+ & \left|\tfrac{E_\lambda\ \varsigma}{(x_2 - x_1)^2}\right|^2 \sigma_{x_1}^2
\end{aligned} \tag{6.6}$$

These values and their uncertainties have been taken from table 6.1 and from the Particle Physics Booklet [83] and here summarized:

- $c = 2.99792458 \times 10^8$ m/s ;
- $h = (6.6260690 \times 10^{-34} \pm 3 \times 10^{-41})$ J s ;
- $\lambda = (1570 \pm 2)$ nm ;
- $\epsilon = (1.60217649 \times 10^{-19} \pm 4 \times 10^{-27})$ J ;
- $\varsigma_{nois} = 2\sqrt{2ln2} \cdot \sigma_{nois} = (6.52 \pm 0.07)$ mV ;
- $\varsigma_{wien} = 2\sqrt{2ln2} \cdot \sigma_{wien} (4.03 \pm 0.05)$ mV.

For the amplitude uncertainties we have to consider the contribution due to both the fit analysis (σ_x^{fit}) and the oscilloscope accuracy (σ_x^{osc}). The first one is taken from table 6.1; the second one is equal to $o_s/\sqrt{N_{1,2}}$, where $o_s = 1.5 \times 10^{-2}$ mV, from previous section, while $N_1 = 15980$ and $N_2 = 10393$ are respectively the number of signals carrying 1 and 2 photons. This comparison leads to:

- $x_1^{noisy} = (16.27 \pm 0.07)$ mV ;

- $x_2^{noisy} = (28.80 \pm 0.07)$ mV ;
- $x_1^{wiener} = (7.51 \pm 0.03)$ mV ;
- $x_2^{wiener} = (23.12 \pm 0.05)$ mV .

By substituting these values in the development of equation 6.6 we obtain, for noisy signals:

$$\begin{aligned} \sigma^2_{\Delta \mathrm{E_N}} &= 4.2 \times 10^{-16} + 2.7 \times 10^{-7} + \\ &+ 1.1 \times 10^{-16} + 2.0 \times 10^{-5} + 5.5 \times 10^{-6} + 5.4 \times 10^{-6} \\ &= 3.1 \times 10^{-5} \end{aligned}$$

while for Winer filtered signals:

$$\begin{aligned} \sigma^2_{\Delta \mathrm{E_W}} &= 1.0 \times 10^{-16} + 6.8 \times 10^{-8} + \\ &+ 2.6 \times 10^{-17} + 5.7 \times 10^{-6} + 4.7 \times 10^{-7} + 1.8 \times 10^{-7} \\ &= 6.4 \times 10^{-6} \end{aligned}$$

As it can be seen, in both cases the main contributions are due to the FWHM, ς, and to amplitude estimation, x.

Summarizing, by using Eq. 6.3 and its propagation, Eq. 6.6, I estimated that TIC TES detector is able to detect the single photon state in the telecom wavelength (at 1570 nm = 0.789 eV) with an Energy Resolution of:

$$\Delta E_{\mathrm{wiener}} = (0.203 \pm 0.003) \text{ eV}$$

with a gain of a factor grater than 2, with respect to the signals not processed by the Wiener filter:

$$\Delta E_{\mathrm{noisy}} = (0.411 \pm 0.006) \text{ eV}.$$

Now, let's compare these two results with Eq. 3.9 (see Chap. 3.1). In the limit of strong electrothermal feedback, this equation estimates the theoretical value for the energy resolution, knowing C, α and n: respectively the heat capacity, the temperature sensitivity and the exponential that describes the nature of thermal link between TES and thermal bath.
Extrapolating these values ($C \simeq 1 \times 10^{-15}$ J/K, $\alpha \simeq 10$ and $n \simeq 5$) from TIC impedance measurements [63] we evaluated

$$\Delta E_{\mathrm{the}} \approx 0.17 \text{ eV}.$$

The loss in energy resolution can be explained considering the distance between the tip of the fiber and the TES. Due to this distance, the geometrical coupling between the fiber spot and the active area is ca. 60% (see Chap. 4.2): in this situation, photons that irradiate device electrodes would generate noise that reduces the detector resolving capability.

6.1.3 Energy Evaluation and Response Linearity

An important property that can be estimated from real data is the energy associated to the single photon pulse. The difference between the experimental energy computed from the measured pulses E_{exp} and the theoretical energy of the absorbed photons E_{the}, gives another important information about the collection efficiency of the system. Moreover extending this analysis over all the photon states allows to study both the linear behavior in the pulse amplitude response and the collection efficiency ε [84].

To carry out the first analysis let's consider the detector bias circuit with dc-SQUID readout scheme reported in Fig. 6.9 and the 1γ pulse signal of absorbed photon in Fig. 6.2.

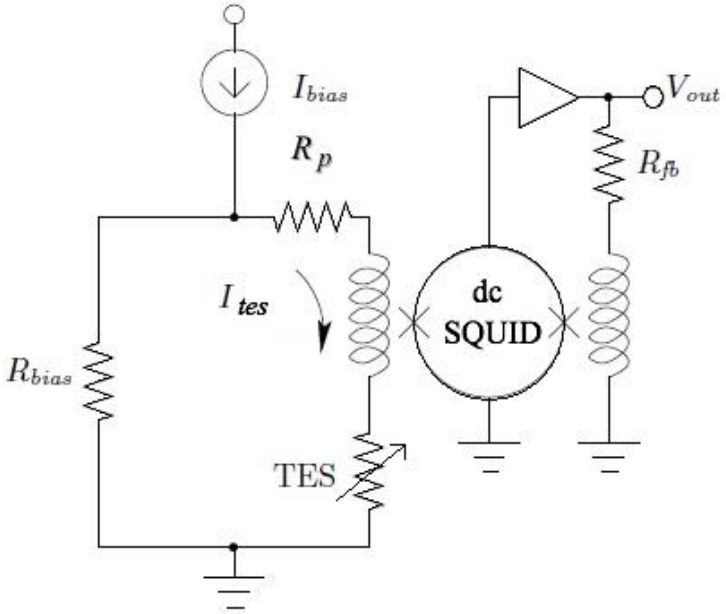

Figure 6.9. TES bias circuit whit dc-SQUID readout.

During a current pulse, the energy removed from a calorimeter by a reduction in the bias power from the steady-state value is

$$E_{\text{exp}} = -\int_{t_0}^{t_f} \mathrm{d}t\ P_{\text{tes}}(t) = -\int_{t_0}^{t_f} \mathrm{d}t\ (V_{\text{tes}}\ \Delta I_{\text{tes}}(t)) \tag{6.7}$$

where the voltage across the TES, by using the Kirchhoff's law, is

$$V_{\text{tes}}(t) = R_{\text{bias}}\ [I_{\text{bias}} - I_{\text{tes}} - \Delta I_{\text{tes}}(t)] - R_{\text{p}}\ [I_{\text{tes}} + \Delta I_{\text{tes}}(t)] + L\ \frac{\mathrm{d}\Delta I_{\text{tes}}(t)}{\mathrm{d}t}$$

Substituting $V_{\text{tes}}(t)$ in Eq. 6.7, the inductive term goes to zero on integration, since the energy stored in the inductor is the same before and after a pulse [36], and the measured photon energy expression becomes:

$$E_{\text{exp}} = -[R_{\text{bias}}\ (I_{\text{bias}} - I_{\text{tes}}) - (R_{\text{p}}\ I_{\text{tes}})] \int_{t_0}^{t_f} \mathrm{d}t\ \Delta I_{\text{tes}}(t) \tag{6.8}$$

$$+(R_{\text{p}} + R_{\text{bias}})\ \int_{t_0}^{t_f} \mathrm{d}t\ \Delta I_{\text{tes}}^2(t)$$

The 1γ voltage waveform of Fig. 6.2 can be converted in the current pulse $\Delta I_{\text{tes}}(t)$, dividing by the amplification gain factor: the trans-resistance G (Eq. 4.2, Sec. 4.3) which depends on the SQUID polarization, obtaining Fig. 6.10.

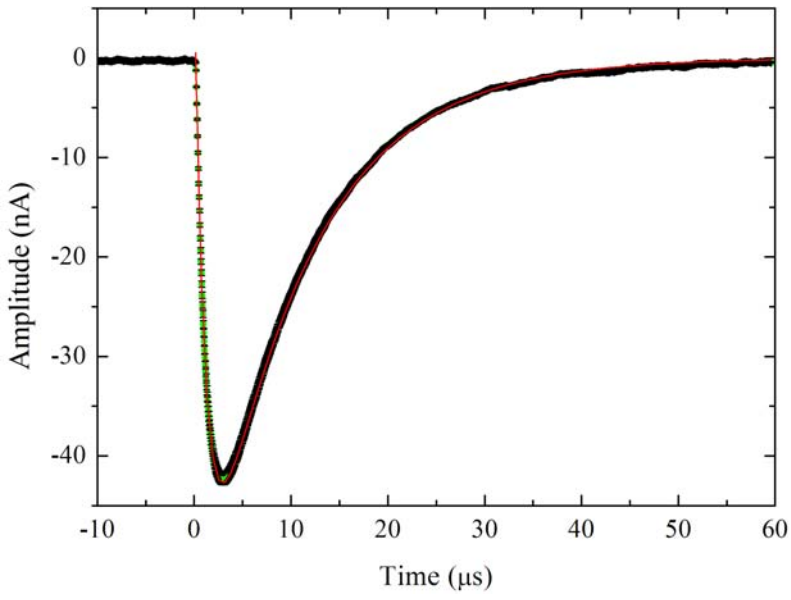

Figure 6.10. Current pulse's single photon state in green, pulse fit in red.

For the dataset proposed in the previous paragraphs, the bias circuit parameters set to obtain the current pulse of Fig. 6.10, were[1]:

- $M_{in}^{-1} = (22.2 \pm 0.4)\ \mu\text{A}/\Phi_0$,
- $M_f^{-1} = (66 \pm 1)\ \mu\text{A}/\Phi_0$,
- $R_{fb} = (100.0 \pm 0.1)\ \text{k}\Omega$,
- $R_{\text{bias}} = (2.38 \pm 0.05)\ \text{m}\Omega$,
- $I_{\text{bias}} = (95.00 \pm 0.06)\ \mu\text{A}$,
- $I_{\text{tes}} = (7.20 \pm 0.04)\ \mu\text{A}$,
- $t_0 = (1.458 \pm 0.002)\ \mu\text{s}$,
- $R_{\text{p}} \ll R_{\text{bias}}$.

Applying Eq. 6.8 to the single photon averaged response pulse (Fig. 6.10), one could estimate the detected single photon energy:

$$E_{\text{exp}}(1\gamma) = (0.76 \pm 0.02)\ \text{eV},$$

Let's remember that for a laser wavelength of 1570 nm, the single photon energy is $E_{\text{the}}(1\gamma) = (0.790 \pm 0.001)$ eV. This difference is mainly due to the energy dispersion towards the substrate and electrodes.

To solve Eq. 6.8, we substitute for $\Delta I_{\text{tes}}(t)$, the exponential Eq. 6.1, which fits current pulse data. Since $R_{\text{p}} \ll R_{\text{bias}}$, in the integral, the terms in R_{p} are negligible. With these hypotheses the energy equation becomes:

$$\begin{aligned} E_{\text{exp}} = \;& R_{\text{bias}}(I_{\text{bias}} - I_{\text{tes}}) \left(\tau_{\text{el}}\ A_1\ e^{-\frac{t-t_0}{\tau_{\text{el}}}} + \tau_{\text{eff}}\ A_2\ e^{-\frac{t-t_0}{\tau_{\text{eff}}}} \right)_{t_i}^{t_f} - \\ - \;& \frac{R_{\text{b}}}{2} \left(A_1^2\ \tau_{\text{el}}\ e^{-2\frac{t-t_0}{\tau_{\text{el}}}} + A_2^2\ \tau_{\text{eff}}\ e^{-2\frac{t-t_0}{\tau_{\text{eff}}}} \right)_{t_i}^{t_f} - \\ - \;& 2\ R_{\text{b}}\ (A_1 A_2)^2 \left(\frac{\tau_{\text{eff}}\ \tau_{\text{el}}}{\tau_{\text{eff}} + \tau_{\text{el}}} \right) \cdot \exp\left(-\frac{(\tau_{\text{eff}} + \tau_{\text{el}})(t-t_0)}{\tau_{\text{eff}}\ \tau_{\text{el}}} \right)_{t_i}^{t_f} \end{aligned} \tag{6.9}$$

where t_i is the pulse start time and t_f is the pulse end time.

Substituting data from fit parameters, the second and the third terms in Eq. 6.9 (corresponding to the $\Delta I_{\text{tes}}^2(t)$ term) result negligible with respect to first one. In

[1] R_{bias} value results from an averaged measurements, at ~ 40 mK, by using the so called '4-wires' method and a resistance bridge.

such a way to estimate the uncertainty, on photon energy evaluation, it could be enough to propagate only the first term of Eq. 6.9, obtaining:

$$\begin{aligned}\sigma^2_{E_{\rm exp}} \simeq & \left|\frac{\partial E_{\rm exp}}{\partial R_{\rm bias}}\right|^2 \sigma^2_{R_{\rm bias}} + \left|\frac{\partial E_{\rm exp}}{\partial I_{\rm bias}}\right|^2 \sigma^2_{I_{\rm bias}} + \left|\frac{\partial E_{\rm exp}}{\partial I_{\rm tes}}\right|^2 \sigma^2_{I_{\rm tes}} + \\ + & \left|\frac{\partial E_{\rm exp}}{\partial \tau_{\rm el}}\right|^2 \sigma^2_{\tau_{\rm el}} + \left|\frac{\partial E_{\rm exp}}{\partial \tau_{\rm eff}}\right|^2 \sigma^2_{\tau_{\rm eff}} + \left|\frac{\partial E_{\rm exp}}{\partial t_0}\right|^2 \sigma^2_{t_0} + \\ + & \left|\frac{\partial E_{\rm exp}}{\partial t_i}\right|^2 \sigma^2_{t_i} + \left|\frac{\partial E_{\rm exp}}{\partial t_f}\right|^2 \sigma^2_{t_f} + \left|\frac{\partial E_{\rm exp}}{\partial A_1}\right|^2 \sigma^2_{A_1} + \left|\frac{\partial E_{\rm exp}}{\partial A_2}\right|^2 \sigma^2_{A_2}\end{aligned}$$

Where only the first three addenda have the same magnitude order and only these terms contribute to the uncertainty on the single photon energy evaluation. The main contribute is due to $R_{\rm bias}$, given by the SQUID developer. In the others two ($I_{\rm tes}$ and $I_{\rm bias}$), the accuracy to measure both the voltage through the TES and to bias the device and the accuracy to estimate the trans-resistance, which links the voltage to the current, play the fundamental roles.
From this consideration, the square of the single photon energy standard deviation results:

$$\sigma^2_{E_{\rm exp}}(1\gamma) \approx 4 \times 10^{-4}$$

By Eq. 6.7 we can also estimate the measured energies of the signals carrying 2 to 6 photons. Reporting in graph $E_{\rm exp}$ as a function of $E_{\rm the}$ for all the 6 photon states (Fig. 6.11), we are able to study the linearity of the pulse response and the collection efficiency ε [84].

The slope, of the linear fit over this latter plot, leads to $\varepsilon = 0.949 \pm 0.007$. This result means that almost all the energy of the incident photons is detected.
The plot also shows that TIC TES has a linear behavior in the pulse response: within the first 6 photon states the linearity is inside the 2.5% and there is no saturation on the response, so the computed energy of the measured pulse response can be considered proportional to the incident quantum state.

6.1.4 Quantum Detection Efficiency

As for any other detector, Quantum Detection Efficiency (DE) is another important parameter necessary to characterize the device. It represents the number of detected photon with respect to the number of incident photon emitted by a source.

In our case we have to consider as the detector, not only the TES device, but the system composed by the fiber optics inside the Dilution Refrigerator that irradiates the TES and the TES itself. This is necessary because we are able to calibrate (i.e. to know the photon emitted number) the source system up to the last optical fiber outside the DR. So the calibrated source system (see also Chap. 4.4) is composed by the pulsed laser and, in cascade, the optical attenuators and fiber optics.

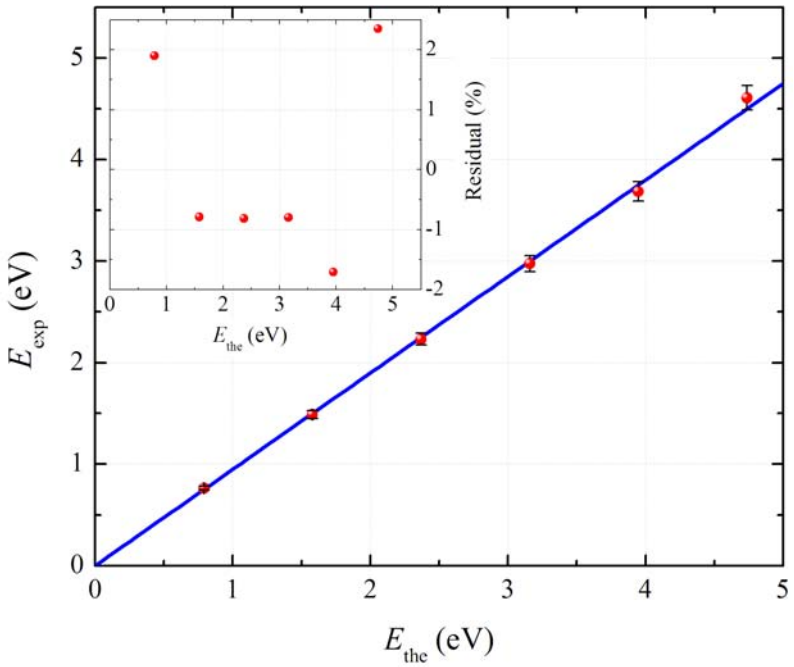

Figure 6.11. TIC energy response has a linear behavior with respect to the incident quantum states. The linearity, inside the 2.5% (inset residual), is within the first 6 detected photons.

After this brief clarification let's consider the photon statistics of the TES device and compare its response distribution to that of the incident source, as we have already reported in [21].

The photon distribution of a pulsed coherent light source, which emits μ mean photons per pulse, follows the Poissonian distribution:

$$P_{\mathrm{k,inc}} = \frac{\mu^k}{k!} e^{-\mu^k} \tag{6.10}$$

where k is the number of photon states. The response of an ideal detector to such incident photon distribution is described by

$$P_{\mathrm{n,det}}(\eta) = \sum_{k=n}^{+\infty} \binom{k}{n} \eta^n (1-\eta)^{k-n} P_{\mathrm{k,inc}} \tag{6.11}$$

where η is the overall DE that we want to estimate for TIC TES. Substituting, Eq. 6.10 in 6.11 we obtain the detector response photon distribution for a coherent light source [5]:

$$P_{\mathrm{n,det}}(\eta) = \frac{(\eta\mu)^n e^{-\eta\mu}}{n!} \tag{6.12}$$

For data of Fig. 6.8, the estimation of the incident photon is obtained by measuring the emitted power from the source system with the variable optical attenuator (see Chap. 4.4) set to 0 dB and then calculating the corresponding power for the attenuation applied: the mean photon number emitted per pulse $\mu \approx 31$.

Fig. 6.12 is shows the photon occurrences histogram as the total number of detected signals, in each photon state, normalized to the overall number of signals of the acquisition, ca. 50000. Fitting this dataset by using Eq. 6.12 with $\mu = 31$, we obtain an overall detection efficiency $\eta \approx 4.2$ %.

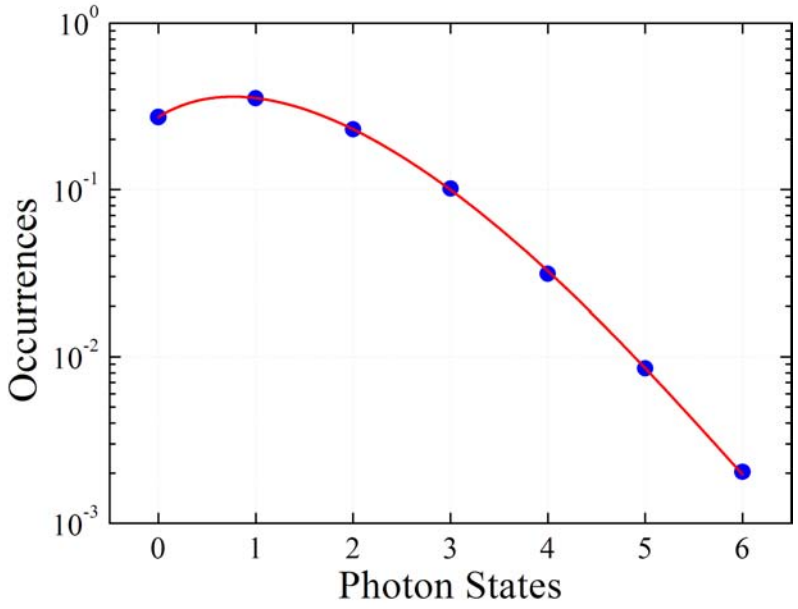

Figure 6.12. Occurences for a mean photon number emitted per pulse of ca. 31, which leads an overall detection efficiency of ca. 4.2 %.

The efficiency loss is due to the geometrical and optical coupling inside the refrigerator: in Chap. 7.2, we could see the same material TES with an improved detection efficiency due to only a different alignment system, which performs the geometrical coupling. Anyway, this η value is in agreement with the absolute calibration measurement on TIC devices [85], explained in the following Chap. 6.3, even if it results very low with respect TES device DE values of literature [20].

6.2 Working Spectral Range

The TESs developed up to now present the reflection losses [86] due to the Ti metallic layer that is about 50 % in the visible range. This fact limits the overall DE, but allows to apply our TES over a broad spectral range. In particular we irradiate TIC TES with laser sources from visible to infrared: 406 nm, 690 nm, 1310 nm and already shown 1570 nm.

This paragraph will briefly show the counting obtained with the violet source, to compare with one of the previous section. At the end an outline will summarize the main goals by using the other sources and also other samples characterized during my Ph. D. work.

A first comparison between the signal at 1570 nm and at 406 nm in shown in Fig. 6.13, where is easily distinguishable the pulse response difference.

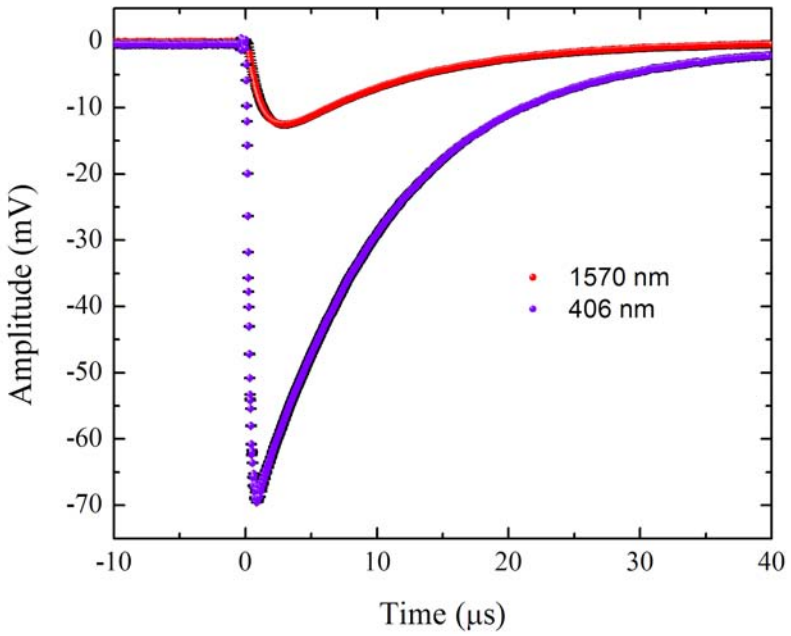

Figure 6.13. Averaged single photon signal at 406 nm, in violet, and at 1570 nm, in red (error bars in black).

While fitting the pulse shape, reported in Fig. 6.14, we obtain the same time constants: $\tau_{\text{el}} = (0.241 \pm 0.001)\ \mu$s and $\tau_{\text{eff}} = (10.420 \pm 0.010)\ \mu$s. The confirmation of these parameters doesn't depend on E_γ but on device characteristics.

The 406 nm source is a Coherent CUBE diode laser system, pulsed at 40 kHz with a pulse duration of 85 ns: Fig. 6.15 shows the acquisition of 50 thousand

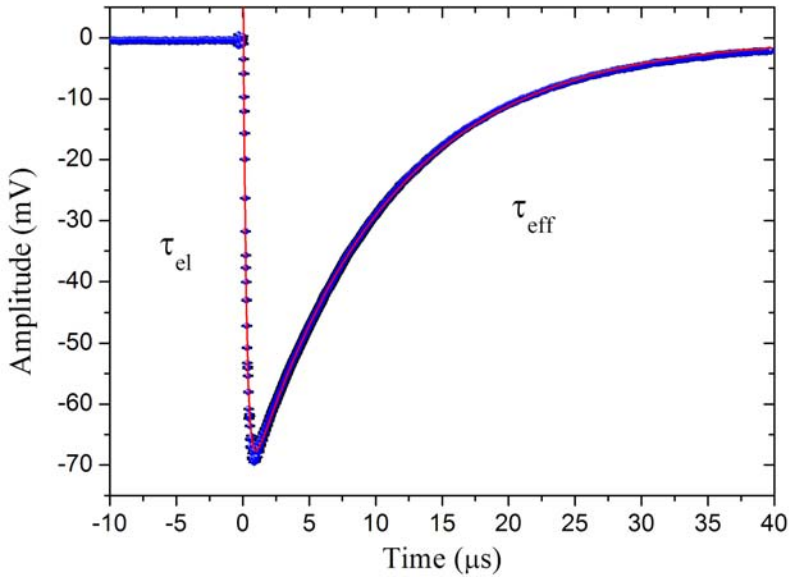

Figure 6.14. Averaged single photon signal (blue), at 406 nm; fit of the pulse (red) estimates $\tau_{\rm el} = (0.241 \pm 0.001)$ μs and $\tau_{\rm eff} = (10.420 \pm 0.010)$ μs.

averaged signals, in which it is possible discriminate up to 10 photons. The single photon signal, of the previous picture, has been extrapolated from this latter plot.

Let's consider that at this wavelength E_γ is 3.05 eV ($\pm$ 0.04 eV) and the discriminated photons are 10. So our TiAu TIC device is able to work in a wide spectral range, starting from about 0.7 eV (near infrared) up to ca. 30 eV (extreme ultraviolet).
The "soft" saturation energy [36] of this kind of calorimeter, i.e. the pulse energy that drives TES completely normal, is $E_{\rm sat} \approx C\ T_{\rm c}/\alpha$: for TIC detector should be about 100 eV, so in principle we could extend the working range up to soft X-rays. After that, when the pulse energy exceeds $E_{\rm sat}$, the energy resolution is degraded but the energy of the pulse can still be estimated, as higher-energy photons lead to pulses that are saturated for longer periods of time.

Coming back to the averaged pulses of Fig. 6.15 we processed them following the same filter analysis of the previous section acquisition. Applying the Wiener filter over the noisy traces to build the 'clean' amplitude histogram of Fig. 6.16 and then to calculate the Full Width at Half Maximum energy resolution $\Delta E = (0.390 \pm 0.006)$ eV.

To estimate the uncertainty over this value the same procedure of Eq. 6.6 has been applied. However, while one of the main error contributions is still due to the

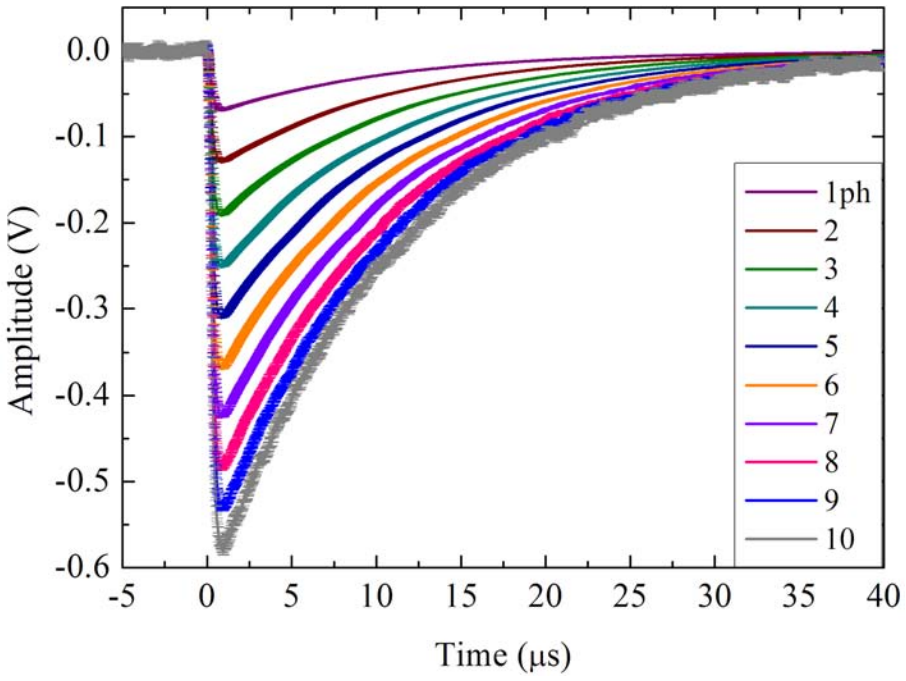

Figure 6.15. From 1 to 10 detected photons (averaged signals) at 406 nm by TIC device.

FWHM, this time, the other one is due to the laser wavelength, instead of to the amplitude estimations.

This ΔE value is larger than the one obtained with the source at 0.789 eV and it would seem a lost of the detector resolution capacity. In fact if one compare the resolving power, i.e. the ratio $E_\gamma/\Delta E$, he would observe a decrease, which is consistence with the Kozorezov theory [87]. He presented a model for optical superconducting TES and STJ (superconducting tunnel junction), to explain the resolution limitation due to a loss of high energy phonons, into the substrate, during the downconversion stage. This behavior can be observed plotting the resolving power as a function of photon energy, the data points follow the model:

$$\frac{E_\gamma}{\Delta E} \propto \frac{E_\gamma}{\sqrt{\kappa^{-1}E_\gamma + j\ E_\gamma}}$$

where k and j are related to the photon and phonon downconversions. Unluckily, in our case, even using all the four available sources, data don't cover a sufficient large range to accurately estimate j or the trend shown in the model.

Another important consideration about this NIR–optical spectral range is the

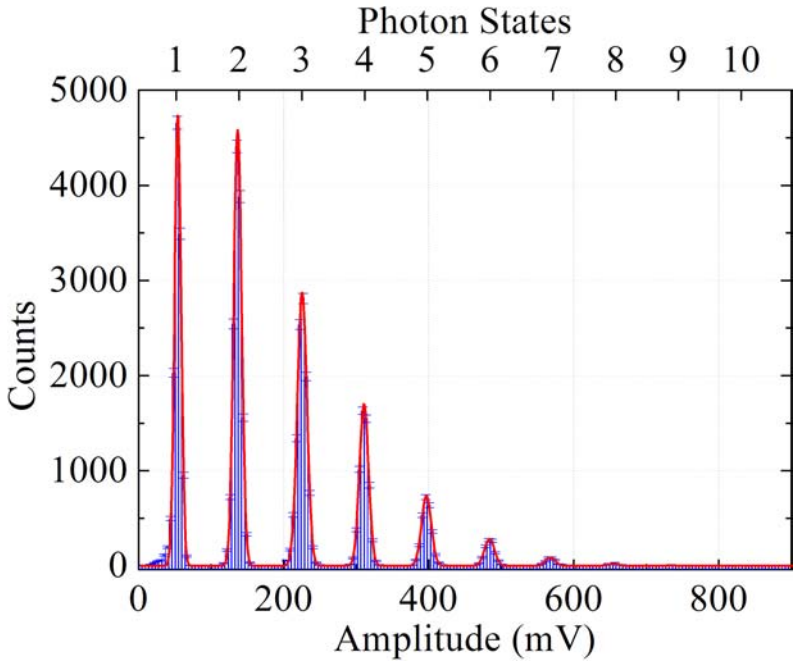

Figure 6.16. Wiener amplitude histogram to discriminate photon number at 406 nm. By fit process we have obtained $\Delta E = 0.390$ eV ($\pm$ 0.006 eV).

pulse response's behavior. For the case of 1570 nm source I have shown the proportionality between the computed energy from pulse response and the photon energies, Fig. 6.11.

Now, we are going to look upon the measured single photon energy of the four sources, with respect to their theoretical energy, to extrapolate the collection efficiency ε of this brad spectral range.
This comparison can be done because we acquired photon counting by using both the same device (TIC) and the optical set up; moreover, both the squid and the TES were maintained at the same bias working point.
Fig. 6.17 shows E_{exp} as function of E_{the} and by the fit we can conclude that, over the wide spectral range, the linear relation is still present with $\varepsilon = 0.96 \pm 0.02$.

Finally, Tab. 6.2 summarizes the main results obtained by TIC and by another detector at the discussed different wavelengths during last three years.

The most important result is the capability to discriminate up to 29 photon states at 1570 nm, Fig. 6.18 with an energy resolution of $\Delta E \simeq 0.32$ eV. Until now, such count represents the biggest amount of photons discriminated by single photon detectors without reaching the device saturation [21].

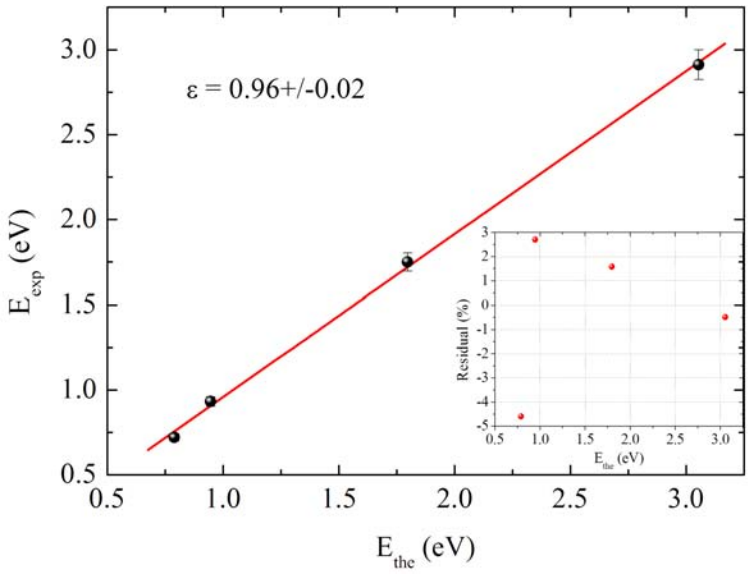

Figure 6.17. Overall collection efficiency estimated from measured single photon energy at different wavelengths: 1570 nm, 1310 nm, 690 nm and 406 nm.

wavelength (nm)	$E_{\rm exp}(1\gamma)$ (eV)	ΔE (eV)	ph. num.
406	2.91	0.39	10
690	1.750	0.31	6
1310	0.932	0.26	9
1570	0.764	0.203	6
1570	([1])	0.32	**29**
1570	([2])	**0.18**	3

Table 6.2. Main results obtained in TES development [21]. ([1]): this acquisition has been obtained discriminating from 2 to 29 photon states, so it has not been possible to estimate $E_{\rm exp}(1\gamma)$. ([2]): in this case the TES active area was 10 μm$\times$ 10 μm, we expected the smaller active area (smaller heat capacity) improves the energy resolution.

Over this count we also investigated the amplitude behavior, finding that the TES amplitude response is linear in the first 15 photons within 2%, Fig. 6.19.

A preliminary improvement on discrimination efficiency, shown in Fig. 6.20, has been obtained irradiating a 10 $\times$ 10 μm^2 active area TES, we expected a better energy resolution due to the smaller device heat capacity (Eq. 3.9). An intrinsic

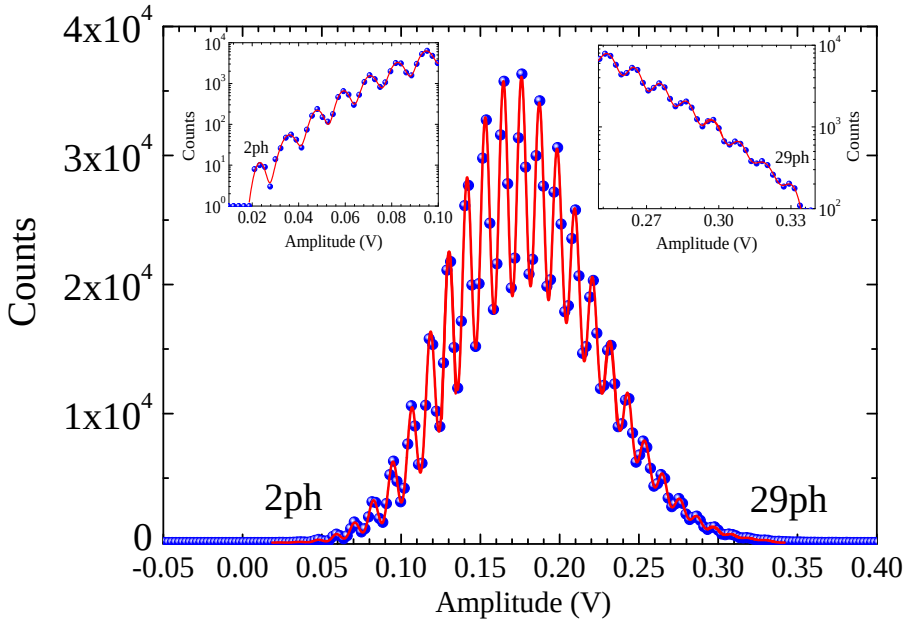

Figure 6.18. Discrimination of up to 29 photons at 1570 nm, $\Delta E \simeq 0.32$ eV. In the insets the magnifications of the first and last 7 photons.

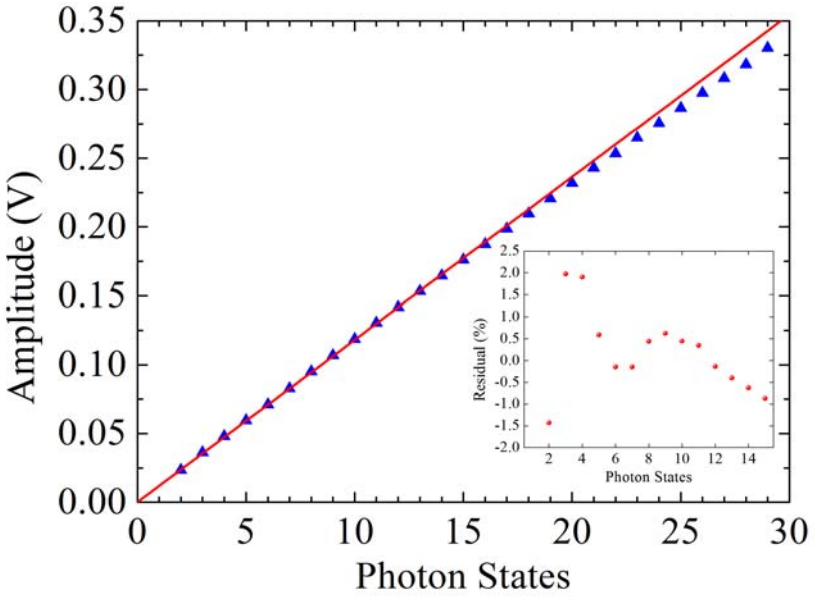

Figure 6.19. The fit (red line) shows the linearity in the amplitude response up to 15 photons within 2%; residual graph in the inset.

device resolution $\Delta E \simeq 0.18$ eV was reached at 1570 nm.

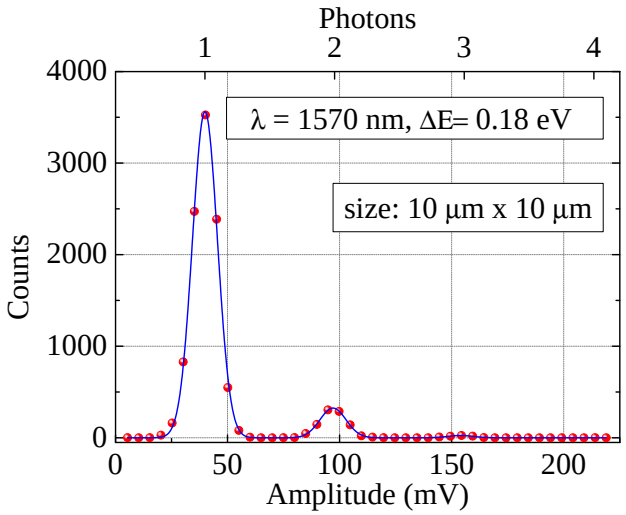

Figure 6.20. Histogram of photon counting, $E_\gamma \simeq 0.79$ eV, $\Delta E \simeq 0.18$ eV and 3 detected photons.

Both of these results have been recently published in [21]. Fig. 6.21 concludes this section with a plot of the amplitude histograms acquired by TIC at different wavelengths and summarized in Tab. 6.2.

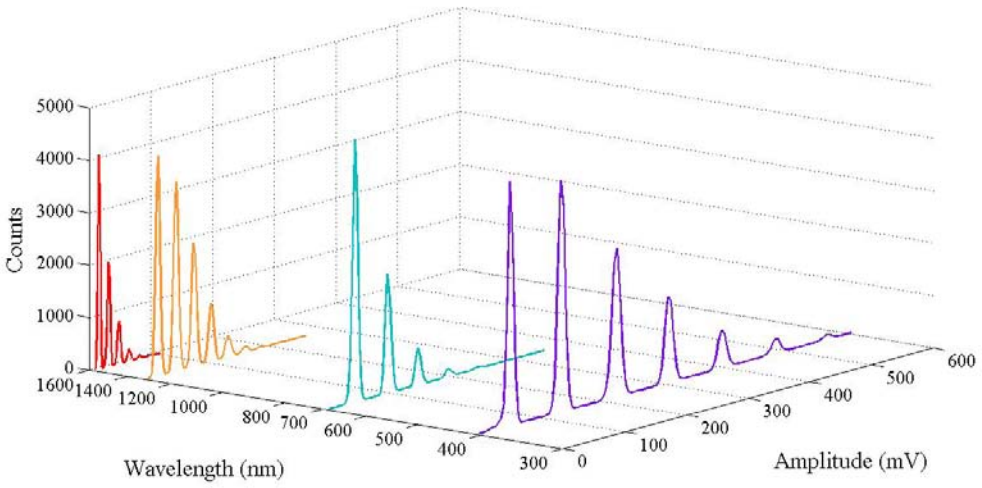

Figure 6.21. Comparison between the counting histograms obtained at 406 (violet), at 690 nm (cyan), at 1310 nm (orange) and 1570 nm (red).

6.3 TES Absolute Calibration

For practical application of these detectors it is fundamental a their appropriate characterization. In particular, one of the most important figures of merit to be characterized is the detection efficiency, already estimated for TIC detector in Chap. 6.1.4 and defined as the overall probability of detecting a single photon impinging on the detector.

An efficient solution to measure detection efficiency in the photon counting regime is given by Klyshko's absolute calibration technique [88], even if it has only been deeply studied in the case of single photon click–no-click detectors. In this recent work [85] developed thanks to the collaboration with the INRIM quantum optics group (led by Dr. M. Genovese), we have proposed and demonstrated an absolute technique for measuring quantum efficiency, based on a parametric down conversion (PDC) heralded single photon source [88], exploiting all the information obtained from the output of the TES and without requiring reference standards.

More details about this absolute calibration method are clearly described in [85], so only an overview, to explain the experiment and to discuss the result, is pointed out here.

Let's define the probabilities of observing i photons per heralding count in the presence and in the absence of the heralded photon: $\mathcal{P}_{\mathcal{H}}(i)$ and $\mathcal{P}_{\mathcal{A}}(i)$ respectively. Being ξ the probability of having a true heralding count, i.e. not due to stray light and dark counts, and $\gamma = \tau\eta$ the TES total quantum efficiency, where τ is the optical and coupling losses from the crystal to the fiber end and η is the quantum efficiency of the TES detector as accounted in Chap. 6.1.4.

By these definitions, the PNR detector probability of observing no photons is the probability of no-detection of the heralded photons multiplied by the probability of having no accidental counts in the presence of a true heralding count, plus the probability of having no accidental counts in the presence of a heralding count due to stray light or dark counts:

$$\mathcal{P}_{\mathcal{H}}(0) = \xi(1-\gamma_0)\mathcal{P}_{\mathcal{A}}(0) + (1-\xi)\mathcal{P}_{\mathcal{A}}(0) \tag{6.13}$$

While, the probability of observing i counts consists of three addenda: the probability of no-detection of the heralded photons and the probability of having i accidental counts, plus the probability of detection of the heralded photons and the probability of having $i-1$ accidental counts both in the presence of a true heralding count, and the probability of having i accidental counts in the presence of a heralding count due to stray light or dark counts

$$\mathcal{P}_{\mathcal{H}}(i) = \xi(1-\gamma_i)\mathcal{P}_{\mathcal{A}}(i) + \xi\gamma_i\mathcal{P}_{\mathcal{A}}(i-1) + (1-\xi)\mathcal{P}_{\mathcal{A}}(i) \tag{6.14}$$

with $i = 1,2,...,n$. From Eq. 6.13 the efficiency is

$$\gamma_0 = \frac{\mathcal{P}_{\mathcal{A}}(0) - \mathcal{P}_{\mathcal{H}}(0)}{\xi \mathcal{P}_{\mathcal{A}}(0)} \tag{6.15}$$

and analogously from Eq. 6.14

$$\gamma_i = \frac{\mathcal{P}_{\mathcal{H}}(i) - \mathcal{P}_{\mathcal{A}}(i)}{\xi(\mathcal{P}_{\mathcal{A}}(i-1) - \mathcal{P}_{\mathcal{A}}(i))} \tag{6.16}$$

Since TES has linear response range as shown both in Chap. 6.1.3 and [81], we will expect $\gamma_0 = ... = \gamma_n$ at least for few detected photons. This is one of the advantage of using a PNR detector with respect to a click – no-click single photon one, in our case for each value of i we obtain a estimation for γ allowing a test of consistency for the estimation model.

The calibration is performed using an heralded single photon source based on pulsed non–collinear degenerate PDC (Fig. 6.22). The heralding photon at 812 nm, is spectrally selected by means of an interference filter 1 nm FWHM (IF1) and detected by a single photon detector DET1. The heralding signal from DET1 announces the presence of the conjugated photon that is coupled into the single mode optical fiber and sent towards the TES (DET2) after spectral filtering (IF2 centered at 812 nm with 10 nm FWHM). The filter in front of the TES is just inserted to reduce the background counts while the spectral selection is determined by the trigger detector.

One of the advantages of using a pulsed heralded PDC is the possibility of evaluating the events counted by the TES in the presence of and in the absence of an heralding signal, providing an estimate of the probabilities $\mathcal{P}_{\mathcal{H}}(i)$ and $\mathcal{P}_{\mathcal{A}}(i)$ in terms of events $\mathcal{C}_{\mathcal{H}}(i)$ and $\mathcal{C}_{\mathcal{A}}(i)$. Respectively, these parameters are the number of events observed by the TES counting i photons in the presence of and in the absence of the heralding photon, such as

$$\mathcal{P}_{\mathcal{H}}(i) = \mathcal{C}_{\mathcal{H}}(i) / \sum_i \mathcal{C}_{\mathcal{H}}(i) \qquad \mathcal{P}_{\mathcal{A}}(i) = \mathcal{C}_{\mathcal{A}}(i) / \sum_i \mathcal{C}_{\mathcal{A}}(i)$$

The oscilloscope readout is triggered only when both the pump laser trigger and the heralding detector DET1 clicks are present. The time base is set in order to record on the trace two subsequent laser pulses. In such a way we are able to measure the events containing the heralded photon announced by the contemporary two trigger signals (left pulses in Fig. 6.23) and the subsequent ones not containing the heralded photons (right pulses in Fig. 6.23).

As described in previous chapters we can build the histogram of the amplitudes of the pulses in the presence of (inset (a) of Fig. 6.23) and in the absence of heralding photons (inset (b) Fig. 6.23). In this case we take interest in the integrals of

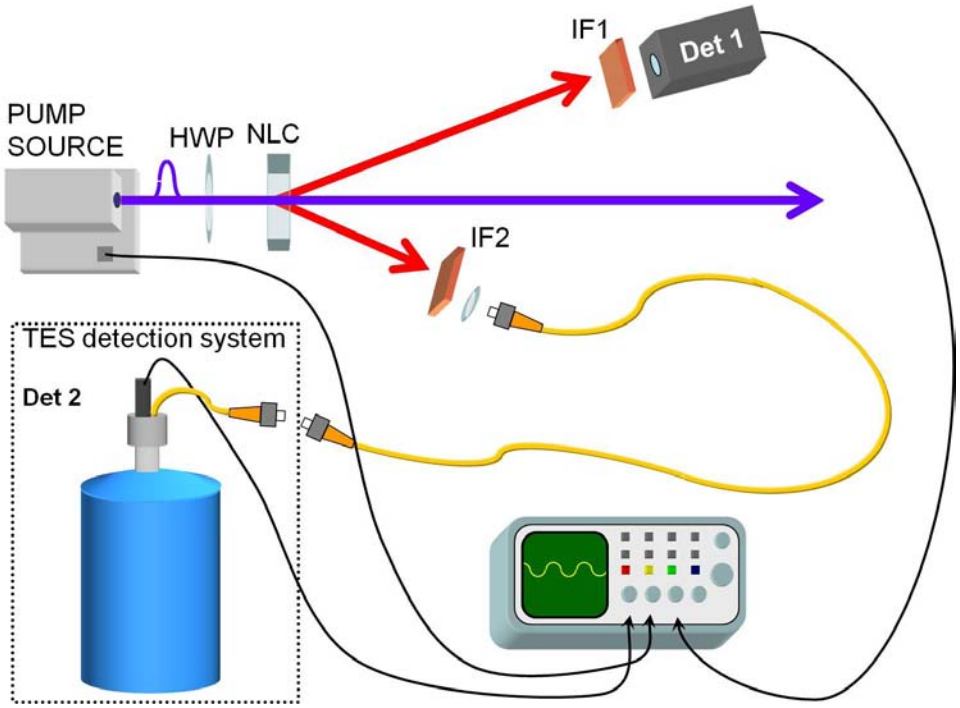

Figure 6.22. Experimental setup [85]: the heralded single photon sources based on non-collinear degenerate PDC pumped by 406 nm pulsed laser. The heralding signal from DET1 announces the presence of the conjugated photon that is coupled in the single mode optical fiber and sent towards the TES based detector DET2, starting from the fiber.

the gaussian curves fitted to the histogram peaks to provide an estimate for the parameters $\mathcal{C}_{\mathcal{H}}(i)$ and $\mathcal{C}_{\mathcal{A}}(i)$.

The probability of having true heralding counts is obtained as $\xi = 1 - n_{\mathrm{OFF}}/n_{\mathrm{ON}}$, where n_{ON} and n_{OFF} are the number of events triggered by the laser pulses and counted by DET1 in the presence and in the absence of PDC emission, respectively. They correspond in one case to true heralded counts, or stray light and dark counts, while in the other case only to stray light and dark counts and they are obtained by means of pump polarization rotation.

According to Eqs. 6.15 & 6.16, with $\xi = 0.98793 \pm 0.00007$, the different estimated values for the total quantum efficiencies are

$$\gamma_0 = (0.709 \pm 0.003)\% \qquad \gamma_1 = (0.709 \pm 0.003)\% \qquad \gamma_2 = (0.65 \pm 0.05)\%$$

The uncertainty contributions in the measurement of γ_0, γ_1 and γ_2 are calculated as in the previous chapter, starting from the peak fit parameters and propagating the uncertainty.

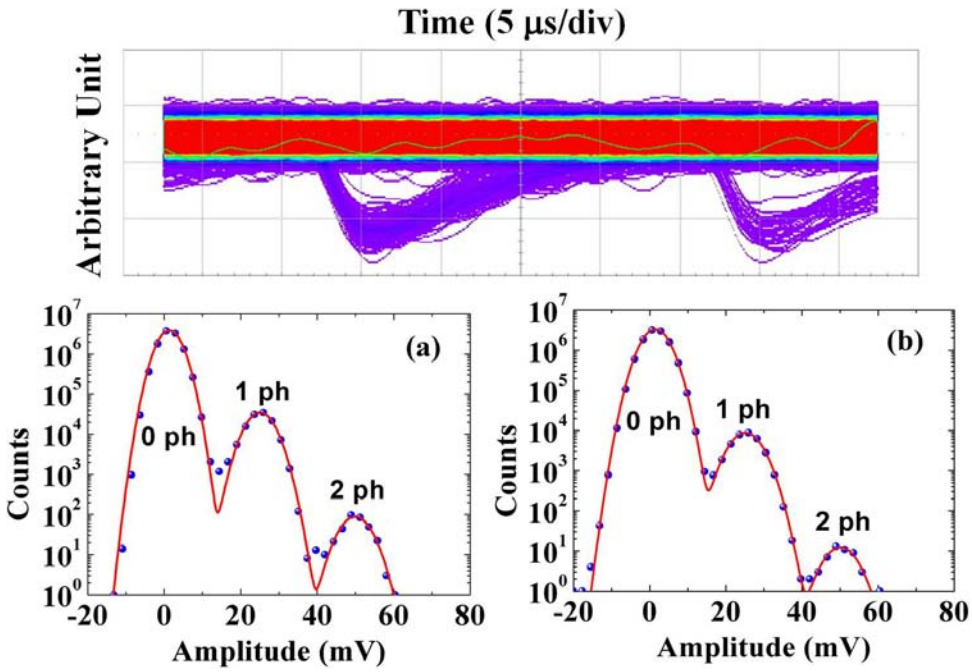

Figure 6.23. Experimental data [85]: oscilloscope screen–shot with traces of the TES detected events. The group of traces on the left (right) is obtained in the presence (absence) of heralding signals. Insets (a) and (b) present the histogram of the amplitudes of the pulses in the presence and in the absence of heralding photons, together with their gaussian fits.

Each measurement was five hours long, corresponding to million of heralding counts. The system was very stable during this long run of measurements. Because of the very good quality of the PDC system as single photon source, we obtained a poor statistic in the estimation of γ_2: this is essentially the reason of the different uncertainty on γ_2 value. For the same reason, it was impossible to obtain estimates of γ for $i > 2$.

To validate this absolute calibration technique, we compared the total averaged efficiencies ($\bar{\gamma}$), obtained as a standard weighted mean of γ_i, with that obtained following the well developed Klyshko's technique [89]. By this method the photon discrimination capability of the TES detector is disregarded because it is considered as a click – no-click detector. By using the same experimental data used for the evaluation of the γ_i, we evaluated the total efficiency in $\gamma_K = (0.707 \pm 0.003)\%$, resulting in total agreement with $\bar{\gamma} = (0.709 \pm 0.002)\%$.

On the basis of the used material we estimated the parameter $\tau \approx 10\%$, corresponding to a quantum detection efficiency $\eta \approx 7\%$. This η evaluation is consistent with that estimated in Chap. 6.1.4, because the DE value was obtained working at a

wavelength of 1570 nm, instead of 812 nm as here, and where we already justify the lower value of η (with respect to the literature's) due to the geometrical coupling and optical losses inside the refrigerator.

Chapter 7

Fast Response TES

In order to improve Ti/Au TES performances, until now shown, we present in this chapter the results reached sharing our knowledges with those of the optical TES Japan team, led by Dr. D. Fukuda and addressed into the AIST (Advanced Industrial and Science Technology) research center.
Leaving for awhile the more metrological qu-candela project, the improvement direction chosen for this collaboration looks at the 'telecom' side of the TES applications: faster response device with a higher detection efficiency.

7.1 Experimental Set Up

To explain how to produce TES with a faster response, we have to recall some information expressed in Chap. 3.2.
Let's remember that the effective response time constant in its approximation of strong ETF regime ($T_b << T_c$ and $\alpha >> 1$) is given by Eq. 3.6:

$$\tau_{\text{eff}} \simeq \frac{n}{\alpha}\,\tau_{\text{th}}$$

The same chapter defines the thermal recovery time as $\tau_{\text{th}} = C_e/G$, where C_e is the electronic heat capacity of the superconducting material and $G = nkT_0^{n-1}$ is the dominant thermal conductance, i.e. the conductance $g_{e,ph}$ in Fig. 3.1.

When the dominant thermal model is the electron-phonon decoupling, n has a value in the range $4-6$ [58]. This means that Eq. 3.6 becomes

$$\tau_{\text{eff}} \propto \frac{C_e}{G} \propto T_0^{-3}$$

whit $n = 5$. As the equation shows, τ_{eff} strongly depends on the operating temperature T_0, instead that on the sensor volume. This means that to speed up the detector response it is necessary to work at higher temperatures, i.e. Ti/Au TES with higher T_c. Since titanium bulk has a critical temperature around 400 mK, increasing the top Ti layer thickness (see Chap. 5.1) allows to produce a TES with $T_c \simeq 300$ mK, $\Delta T_c \simeq 1$ mK and $R_n \simeq 0.6\ \Omega$ (red dots of Fig. 7.1).
Still with reference to Fig. 7.1, a lower critical temperature curve is reported (blue dots) as comparison with the higher one: $T_c \simeq 75$ mK, $\Delta T_c \simeq 6$ mK, $R_n \simeq 0.8\ \Omega$.

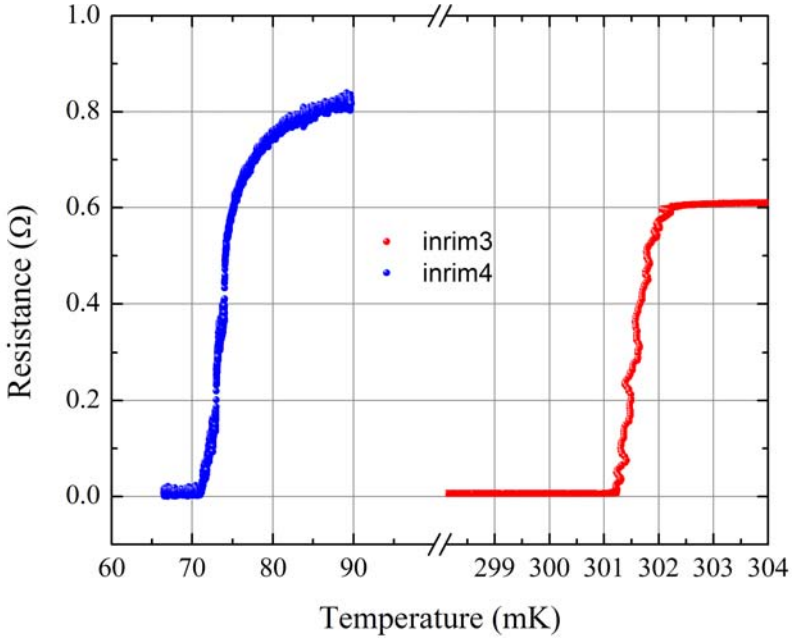

Figure 7.1. Plot of the resistance vs. temperature: comparison between a lower and a higher T_c Ti/Au TES. The inrim3 device (in red) has $T_c \simeq 300$ mK, $\Delta T_c \simeq 1$ mK and $R_n \simeq 0.6\ \Omega$; the inrim4 device (in blue) has $T_c \simeq 75$ mK, $\Delta T_c \simeq 6$ mK and $R_n \simeq 0.8\ \Omega$.

On the other hand, the theoretical energy resolution given by Eq. 3.9 is:

$$\Delta E \approx \sqrt{4\ k\ T_0^2\ \frac{C_e}{\alpha}\sqrt{\frac{n}{2}}} \propto T_0^{3/2}$$

a better ΔE is obtained with lower working temperature T_0. To reduce this handicap we chose to work with a $10 \times 10\ \mu\text{m}^2$ active area TES. A smaller volume means a lower heat capacity and so a bit improvement in the energy resolution. Anyway, a

worsening of ΔE is present as aspected. In Chap. 7.2, we will see that inrim3 device, the faster Ti/Au TES with smaller active area, will have a worse energy resolution than the one shown in Fig. 6.20, of a TES with lower critical temperature and same active area.

With respect to the experimental apparatus used in the INRIM laboratory (Chap. 4), the one exploited in the AIST lab differs for the refrigeration system and the alignment technique of the fiber over the TES. To cool down the experiment we used an Adiabatic Demagnetization Refrigerator (ADR): some information about the working process are pointed out in the next Chap. 7.1.1. The fiber-TES alignment system will be described in Chap. 7.1.2.

Where not specified, we intend that the experimental setup is the same or the differences are negligible for the intended results. For instance to read out the TES signals, we still use a PTB dc-SQUID and a Magnicom room temperature electronics. What is changed is the way to dispose TESs and dc-SQUID inside the ADR.

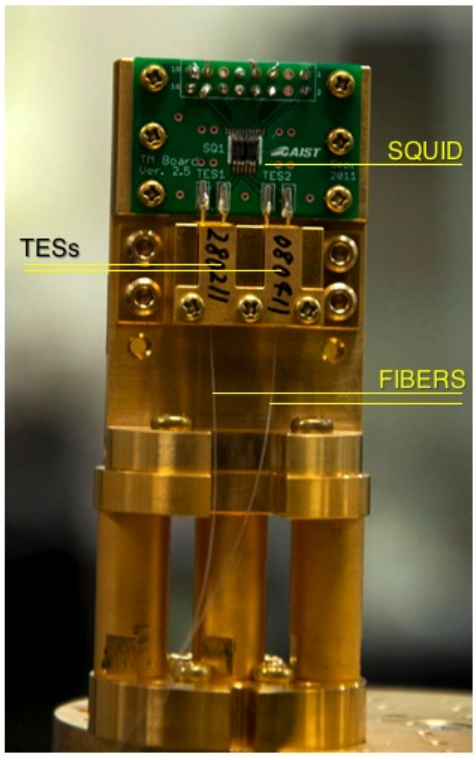

Figure 7.2. Experimental apparatus mounted over the coolest plate of an ADR: two TESs are aligned at the tips of the fibers, inside the copper holder; the dc-SQUID chip is visible.

With reference to Fig. 7.2, two TESs of active area 10×10 μm^2 are cut from the chip of Fig. 5.2 and glued in two different metal holders. Both the TES holders and metal structure are made of OFHC copper covered by a thin gold layer, to reduce oxidation process of the copper. The dc-SQUID is over the TESs, instead of on the bottom of the TES chip, as in Fig. 4.3. All the structure is mounted over the cooler plate of the ADR, inside magnetic shields.

7.1.1 Adiabatic Demagnetization Refrigerator

Instead of a Dilution Refrigerator, AIST laboratory is provided of an Adiabatic Demagnetization Refrigerator (ADR). This kind of helium-free refrigerator has been historically the first method which allowed to reach temperatures below 1K (in 1962) [91], and nowadays ADRs can reach temperatures around 2 mK. The one used at AIST can reach a minimum temperature of about 70 mK.

The working process is based on the properties of a paramagnetic salt whose ions have electronic magnetic moment μ. At the temperatures reachable from this type of refrigerator, the interaction energy among the moments and of the moments with with an external magnetic field is small compared with the thermal energy kT. At those temperatures, the magnetic entropy (few J/mole) is larger with respect to the other entropies of the system. If we cool down the salt, at a certain temperature, the order of magnitude of μ becomes comparable with kT, and a spontaneous magnetic alignment takes place.

Applying an external magnetic field B, it interacts with the magnetic moments and partially orients them along the field direction. This means that at fixed temperature, the field reduces the magnetic entropy cooling the system.

In Fig. 7.3 the entropy vs. temperature for a paramagnetic salt is reported. To explain the working principle, let's start the refrigeration process from point A where the external magnetic field $\mathbf{B}$ is switched on. The line AB represents an isothermal magnetization. The heat produced along AB is delivered to the thermal bath: in our case produced by a mechanical pulse tube refrigerator system [91] reached 4 K temperature. After thermal isolation (through a thermal switch), the crystal is adiabatically demagnetized (line BC). The system warms up along the entropy curve at the final magnetic field, which theoretically is zero. The cooling power is given by the shaded area. The limit of the process is the temperature T_c at which a spontaneous magnetic ordering takes place. The performance of a refrigerator based on paramagnetic salts depends on the starting field and temperature and on the type of salt. Typical values for the field are 0.1 T – 1 T and 0.1 K – 1 K for the initial temperature.

In most cases, however, the use of a DR is preferred because it is not a 'one shot' refrigerator and for absence of magnetic fields. For the one used at AIST institute, after reached the lower temperature ($\sim$ 90 mK), the system spends about 2 hours

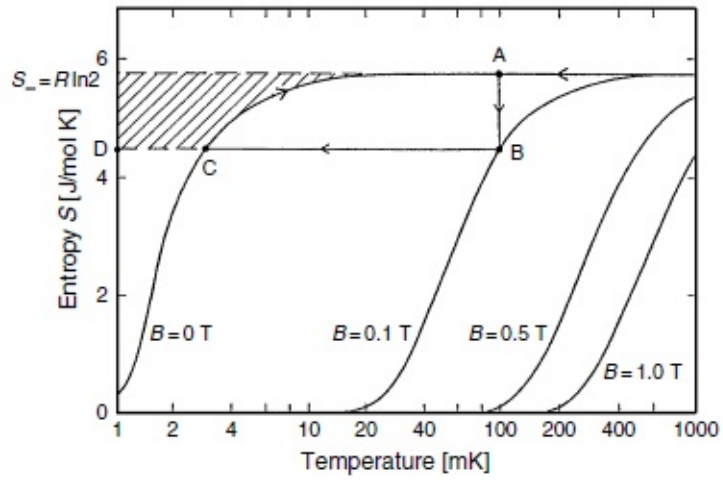

Figure 7.3. Molar entropy of a single crystal of the paramagnetic salt vs. temperature for magnetic fields applied along the crystallographic axis. The refrigeration process starts from A. The line AB represents an isothermal magnetization. The heat produced along AB is delivered to a heat sink (DR). After thermal isolation, the crystal is adiabatically demagnetized (line BC).

to continuously increase its temperature of 10 mK.

Fortunately, because the inrim3 T_c is high, with respect to the working temperature range (90 mK $\div$ 110 mK), the electrothermal feedback condition is still satisfied ($T_b << T_c$, Chap. 3.2). In fact, looking at Fig. 7.4, where inrim3 I_{tes} as a function of I_{bias} is shown, we notice that the curve acquired at 90 mK has a good overlap with that at 107 mK: as a demonstration temperature variation of T_b doesn't influence the TES behavior yet.

7.1.2 Light Coupling Technique

To improve the detection efficiency it is necessary to reduce the losses due to the fiber–TES coupling. The standard core diameter of a single mode optical fiber for 1.5 μm wavelength is 9 μm. As discussed in Chap. 4.2, assuming a Gaussian profile for the fundamental mode of propagation in the fiber, the diameter of the $1/e^2$ irradiance contour at the plane where the waveform is flat exited from the fiber tip, at ca. 100 μm from the TES surface, is spread to ~ 20 μm. Thus a part of the light will be lost due to the discrepancy between the beam diameter and the TES size. Considering a TES with an active area of 10×10 μm^2, to avoid these losses we have to fix the fiber in the center of the detector and in contact with the TES.

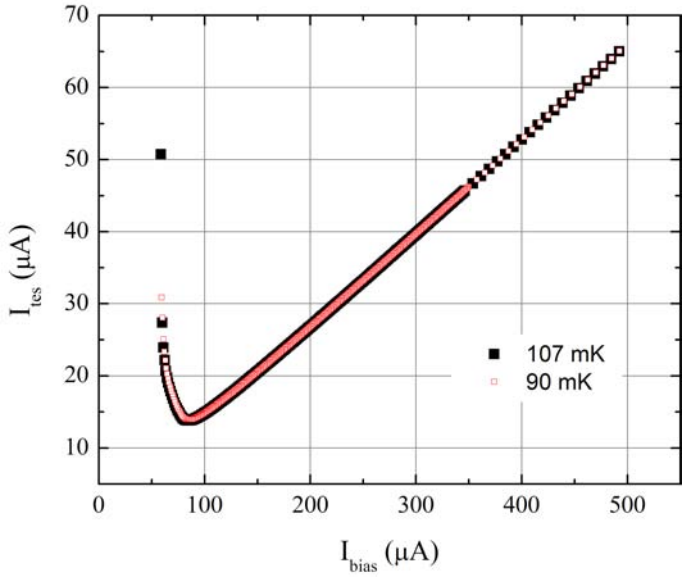

Figure 7.4. inrim3 device current vs. bias current at two different bath temperatures: 90 mK and 107 mK; the two curves present a good overlap.

To reach this goal at AIST institute an 'infrared-scope' has been developed. Following the scheme of Fig. 7.5 the system is composed by an inverted optical microscope, with 50× magnification, an infrared camera connected to a screen, a 1.5 μm laser and an IR lamp. Hence, we exploit the material optical properties for substrate, wirings and detector, in the NIR wavelength range: the Si substrate presents a good transmittance, in contrast with the transmittance of the metal of both wirings and TES [92].

The first step starts looking through the optical microscope and aligning both TES and fiber over a little hole (smaller than the TES chip size) placed on the sample holder plate of the microscope itself. Then we switch on both the lamp, to illuminate the substrate, and the laser source, to observe where the fiber's spot is. Hence, we look through the substrate, by using the camera. Moving the fiber by a 3-axis stage, controlled by DC stepper motor, and watching on the screen we can observe the movements of the fiber over the TES chip and center over the detector.

Before putting in contact the fiber's tip with the TES a drop of an epoxy glue is put on the sensor to fix the fiber position. The glue is chosen to be transparent at the telecom wavelengths but, at the same time, becomes hard if exposed to a UV radiation[1].

[1]The exposition under the UV lamp requires 8 hours.

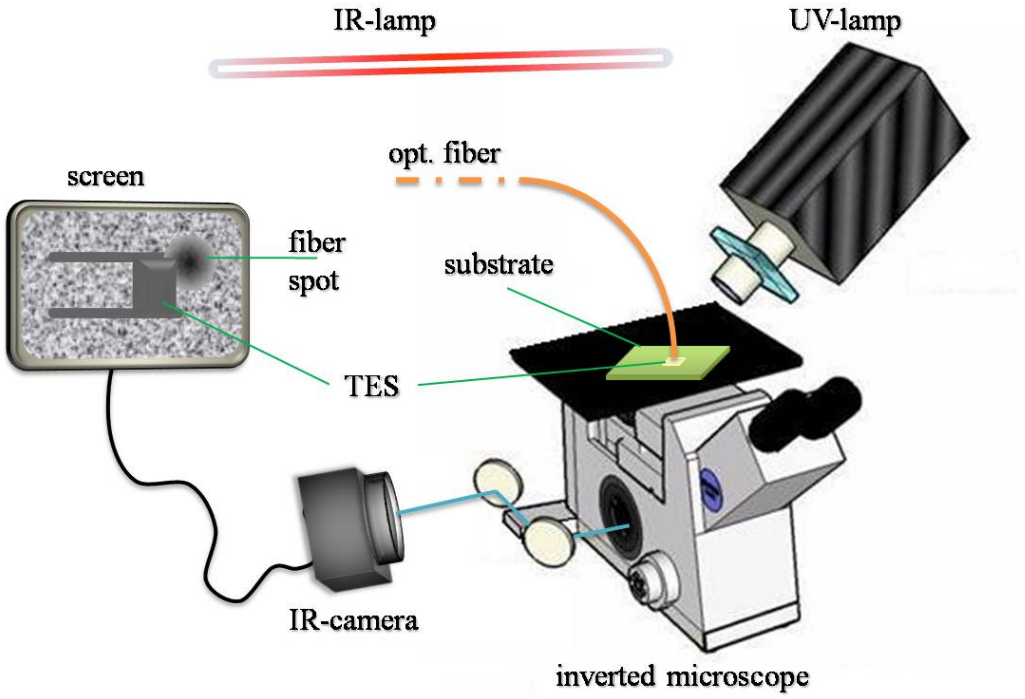

Figure 7.5. Scheme of the TES-fiber coupling system developed at AIST. Imagines are not in scale. It shows the TES substrate on the sample plate of an inverted optical microscope, with the fiber over the device; by using the microscope and an IR camera it is possible to observe the movements of the fiber through the substrate.

7.2 Obtained Results

The first proposed goal, a faster TES, has been easily reached. The device presented in Fig.7.3 and called 'inrim3' has been irradiated by using a pulsed diode laser[2]. With reference to Fig. 7.6 it is possible to observe the different response times with respect to one of Fig. 6.13 at 1570 nm and 407 nm.

The pulse of Fig. 7.6 has been obtained averaging 19745 waveforms of single photon pulse. Eq. 6.1 (Chap. 6.1) fits the averaged pulse and gives an estimation of the electrical time constant $\tau_{\rm el} = (145 \pm 2)$ ns and of the effective time constant $\tau_{\rm eff} = (229 \pm 4)$ ns; even in this case, the uncertainty over these numbers is mainly given by the fit procedure.
The quantitative analysis confirms the faster response of inrim3 device obtained producing a TES with a higher critical temperature, $T_c \simeq 300$ mK. TIC device, whose performances are shown in previous chapter, is characterized by $\tau_{\rm el} \simeq 1.106$ μs,

[2] an Hamamatsu Photonics product with 1535 nm (±3 nm) wavelength.

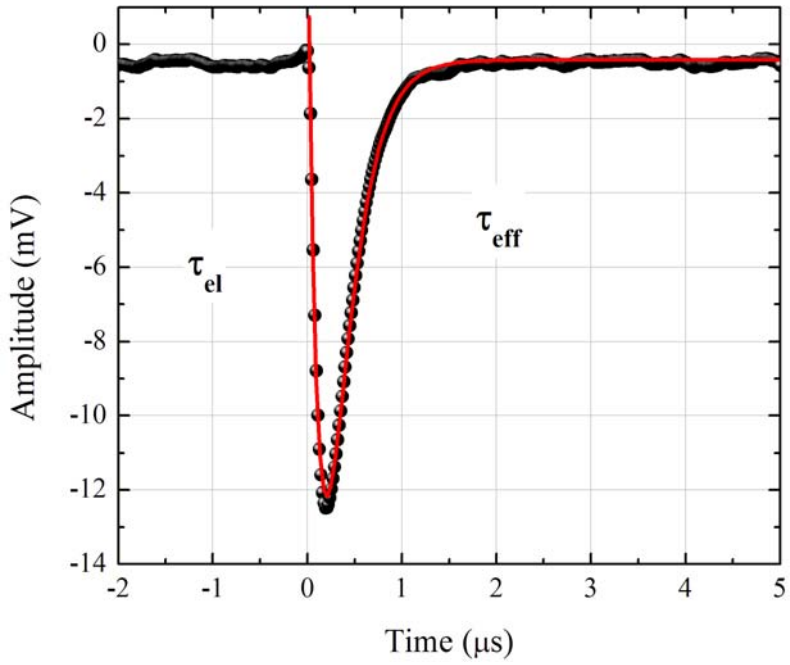

Figure 7.6. Averaged single photon signal at 1535 nm (in black) obtained with TES inrim3; pulse fit (in red) shows an electrical time constant $\tau_{\mathrm{el}} \simeq 145$ ns and effective time constant $\tau_{\mathrm{eff}} \simeq 229$ ns.

$\tau_{\mathrm{eff}} \simeq 10.2$ μs and $T_c \simeq 121$ mK.

The next goal to check is the detection efficiency improvement. To do this, we have to analyze the entire dataset of waveforms from which the pulse of Fig. 7.6 has been extrapolated, and build the distribution of the photon states.

The first step is to apply the Wiener filtering procedure of Chap. 6.1.1 to the 30000 noisy waveforms of the dataset and, the second, to build the amplitude histogram of the filtered signals to estimate the detector intrinsic energy resolution via Equations 6.2 & 6.3: the result is shown in Fig. 7.7. By the fit analysis the energy resolution of inrim3 detector is $\Delta E = (0.263 \pm 0.006)$ eV, where the single photon energy, at 1535 nm ,is $E_\gamma \simeq 0.81$ eV.

The uncertainty over ΔE is estimated by following the same procedure expressed in Chap. 6.1.2. Now, remembering the result of Fig. 6.20 – three photon states at 1570 nm, discriminated by a $\Delta E \simeq 0.18$ eV by using a 10×10 μm^2 active area TES – we notice, as already explained, a worsening in the energy resolution due to the increase of the working temperature.

Evaluating now the number of signals for each photon state and normalizing them by the overall number of acquired signals, it is possible to build the detection

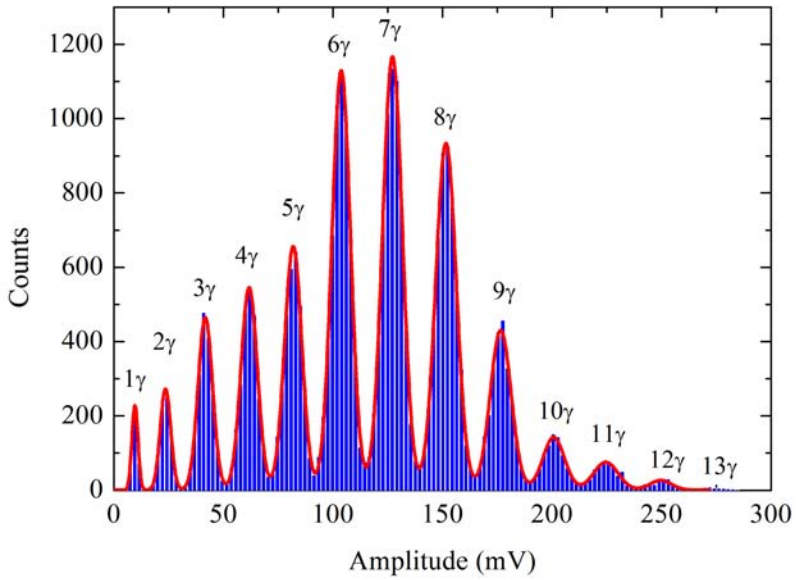

Figure 7.7. Amplitude histogram of Wiener filtered waveforms: by the fit (red line) over the thirteen photon states, the estimated energy resolution of the single photon state (1γ) is $\Delta E = 0.26$ eV (the single photon energy is $E_\gamma \simeq 0.81$ eV).

probability histogram of Fig. 7.8. Since laser sources follow Poissonian emission distribution (as explained in Chap. 6.1.4), fitting the probability photon state histogram by the function of Eq. 6.12 allows to estimate the discriminated mean photon number, $\mu_d = \eta\mu \simeq 7.3$: where μ is the mean photon number emitted by the source and η is the TES detection efficiency we want to estimate.

The laser source was optical attenuated to the single photon counting regime until the mean emitted photon number was $\mu \sim 14$. Substituting this number in Eq. 6.12 for the data of Fig. 7.8, the fit results $\eta \simeq 0.50$ as overall detection efficiency. Because the attenuated laser emission wasn't so stable, we decided to acquire photon counting at several optical attenuations: averaging the obtained η values, we estimate an overall detection efficiency of

$$\eta = 50\% \pm 5\%$$

We want to underline the difference between this result and the values shown in Chapters 6.1.4 & 6.3. The improvement is due to the better TES-fiber coupling system between the one developed at AIST and the one until now used at INRIM. Consider also that neither the low speed devices nor those with faster response present neither antireflection coating nor optical cavity. Such as the obtained detection efficiency value shows agreement with the reflection of metal titanium (and titanium oxide presents) for this wavelength [92].

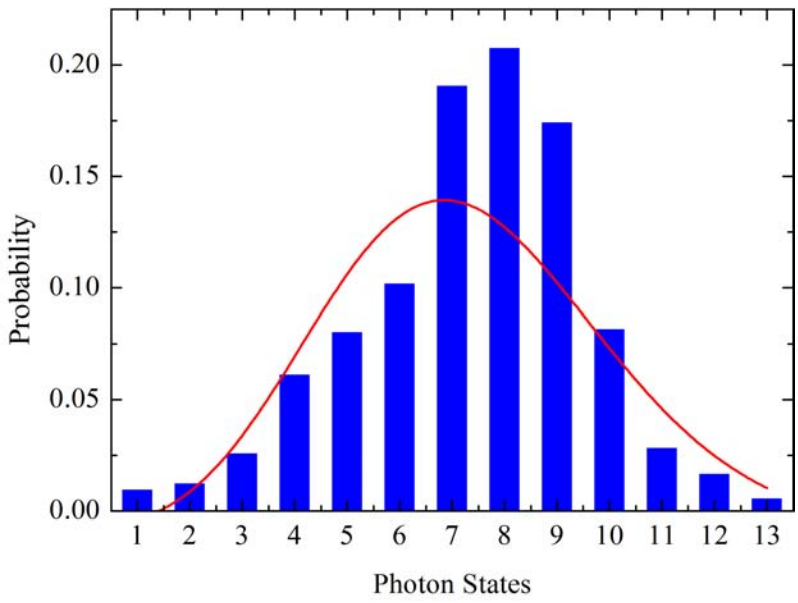

Figure 7.8. Occurences for a mean photon number emitted per pulse of ca. 14, which leads to an overall detection efficiency of ca. 50 %.

Part IV

the bow

Chapter 8

Conclusions

During the three years of Ph.D. school a lot of effort has been applied to improve the TES detectors developed at INRIM and we passed from preliminary counting obtained at 690 nm of wavelength, irradiating a 20×20 μm^2 Ti/Au TES, to develop detectors with a low response time, ca. 200 ns (Chap. 7.2, Fig. 7.6).

During this period we demonstrated also that our TESs work in a broad spectral range (from visible to NIR) with a linear behavior in the energy response (Chap. 6.2, Fig. 6.17). We are able to fabricate and align detector with a smaller active area (10×10 μm^2) which can detect 0.79 eV photons with an energy resolution of about 0.18 eV (Chap. 6.2, Fig. 6.20) and an energy loss of only 0.03 eV into the detection process (Chap. 6.1.3).

It has presented the importance of using an appropriate digital filtering process to improve the signal-to-noise ratio (Chap. 6.1.1, Fig. 6.6), and shown the capability of resolving up to 29 photons (Chap. 6.2, Fig. 6.18) at 1570 nm, and 10 photons at 406 nm (Fig. 6.15), both without the device saturation: until now these photon countings are the best available in literature.

New technique, based on a parametric down conversion single photon source, for the absolute calibration of photon number resolving detectors, to estimate the detection efficiency without the use of reference device, has been presented in Chap. 6.3. At the end, it has also been shown how a good coupling technique (Chap. 7.1.2) can improve the value of this important detector figure of merit (Fig. 7.8), closing to the main limit due to the metal reflectivity.

With reference to Chap. 1, one of the aim obtained inside the qu-candela project was to cover, in the low photon flux regime, the range between 10^3 and 10^0 photons/s by a TES and to superimpose this range with the one covered by a SPAD ($10^6 \div 10^3$ photons/s).
Looking at Fig. 6.18, the mean photon number per pulse is $\mu \simeq 12$ at 9 kHz of repetition rate: that results in a photon flux of about 10^5 photons/s. While from

Fig. 6.16, $\mu \simeq 2$, at 40 kHz of repetition rate: that means $\sim 8 \times 10^4$ photons/s. Hence, the possibility of having a detector able to work from low photon flux regime, 1 photons/s, to flux measurable by conventional semiconductor device, is clearly demonstrated. Even if we would work at 555 nm: the wavelength corresponding to 540×10^{12} Hz of the candela definition.

However for telecommunication applications (quantum cryptography, information, computation ...) these speeds are too slow and the results shown in Chap. 7.2 (detectors able to work at 500 kHz of repetition rate) are a first step in the right direction to develop sensors suitable for such field of research.

In order to improve the quantum detection efficiency, it is necessary to work with an optimized fiber-TES alignment system (as described in Chap. 7.1.2), to avoid losses due to geometrical coupling. To reduce the absorption limit due to the metal reflectivity, we need to develop an antireflection coating or an optical cavity optimized for specific wavelengths, as already reported in literature [20], where a detection efficiency of 98 % has been demonstrated

This dissertation is yield of results obtained in these last three years whose have allowed contributions to international conference and the following scientific publications: [21, 27, 63, 64, 65, 67, 70, 77, 79, 82, 85].

Appendix A

Optical Characterizations

This chapter has been appended after the bulk of this dissertation because it considers only optical analysis on TES material.
In fact here, investigations on optical properties of the titanium/gold film as base for TES detector, obtained by a spectroscopy ellipsometer technique, are shown. The aim of the measurements is knowing the optical constants of the superconductive sensor film, to build a structure able to reduce the metal reflection in the visible-NIR wavelengths, f.i. an antireflection layer as announced in Chap. 8.

Ellipsometry is an optical measurement technique that characterizes light reflection (or transmission) from samples [93]. The key feature of ellipsometry is that it measures the change in polarized light upon light reflection on a sample (or light transmission by a sample).

Basic principles of ellipsometry were established more than 100 years ago, but ellipsometry had been perceived as an 'unproductive instrument' until recently. Light has been used for thickness measurements since 1700s, when scientists looking at thin transparent layers, observed colors that were the result of interference. Brewster noted that these observations "are of extensive use and may be regarded as presenting us with a micrometer for measuring minute thicknesses of transparent bodies by their colors, when all other methods would be inapplicable'' [95].

In the early 1800s, the concept of polarized light was developed and Drude used the phase shift induced between mutually perpendicular components of polarized light to measure film thicknesses down to few tens of angstroms [94]. When the mutually perpendicular components of polarized light are out of phase, the light is said to be "elliptically polarized''. Hence the technique that evolved from Drude's early measurements comes from the fact that polarized light often becomes 'elliptical' upon light reflection: so the name 'ellipsometry' [96].

An important development that led the ellipsometry from random scientific measurements to an analytical technique, for modern surface and thin film technique,

was the availability of digital computers, in the 1960s. In fact, a modern personal computer was adequate for virtually process all the typical ellipsometry calculations and simulations.

The first ellipsometers were built with only a single wavelength. After the half of the 1900s, spectroscopic ellipsometry has evolved significantly, and single-wavelength ellipsometry has now been relegated to tasks such as fast real-time studies on well-understood samples.
In the meanwhile, the application area of spectroscopic ellipsometry has also expanded drastically. In spectroscopic ellipsometry, process diagnosis including thin-film growth can be performed in real time by employing light as a measurement probe. More recently, feedback control, in which complicated device structure is controlled in real time, has been carried out using spectroscopic ellipsometry [96].

A.1 Introduction to Spectroscopic Ellipsometry

Ellipsometry measures the two values Ψ and Δ. These are related to the amplitude ratio Ψ and phase difference Δ between incident and refractive light waves.
In spectroscopic ellipsometry, Ψ and Δ spectra are measured by changing the wavelength of light. In general, the spectroscopic ellipsometry measurement is carried out in the UV-visible region, but measurement in the infrared region has also been performed widely.

In the optical model shown in Fig. A.1, the two ellipsometry parameters (Ψ, Δ) are defined by the following equation [96]:

$$\tan\Psi \cdot e^{(i\Delta)} = \rho(N_0,\, N_1,\, N_2,\, d,\, \theta_0) \tag{A.1}$$

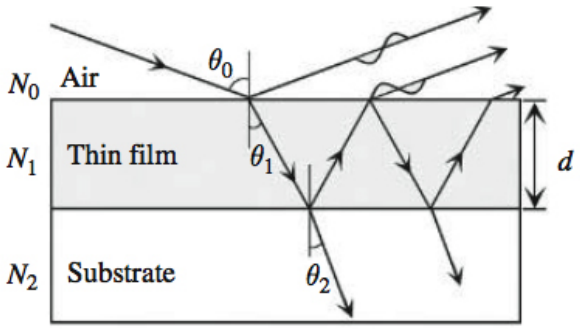

Figure A.1. Optical model consisting of an air/thin film/substrate structure.

Where N_0, N_1 and N_2 denote the complex refractive index of air, thin film and substrate, respectively. A complex refractive index is defined by $N \equiv n - \mathrm{i}k$: n is the real part, that determines the propagation of electromagnetic waves, and k is the extinction coefficient and describes light absorption by opaque media (non-transparent).
The transmission angles θ_1 and θ_2 can be calculated from the incident angle θ_0 by applying Snell's law [93, 94, 96, 97], even for a complex refractive index: $N_0 \sin\theta_0 = N_1 \sin\theta_1$.

In ellipsometry, as in general in optics, the light is classified into p- and s-polarized light waves depending on the oscillatory direction of its electric field. In p-polarization, the electric fields of incident and reflected waves oscillate within the same plane, called plane of incidence. In s-polarization the electric fields oscillate orthogonal to the plane of incidence and parallel to the sample surface.

Optical constants and film thickness of the sample are measured from the differences between p- and s-polarization of incident and reflected waves onto a sample, at the Brewster angle[1]. Fig. A.2 illustrates the measurement principle of ellipsometry.

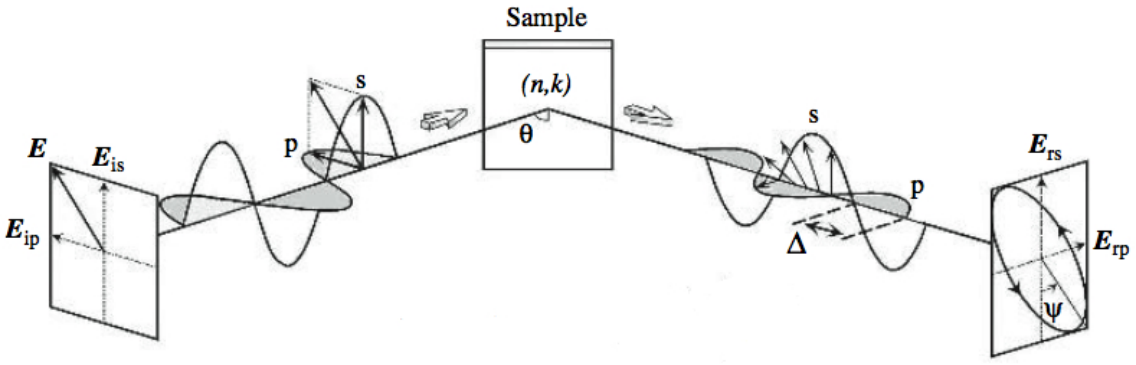

Figure A.2. Measurement principle of ellipsometry [96].

The incident light is linear polarization oriented at +45° relative to the component of electric field parallel to p-polarization, E_{ip} axis. In particular, $E_{\mathrm{ip}} = E_{\mathrm{is}}$ holds for this polarization since the amplitudes of p- and s-polarizations are the same and the phase difference between the polarizations is zero.

[1] It is an angle of incidence at which light with an opportune polarization is perfectly transmitted through a transparent dielectric surface, with no reflections. When unpolarized light is incident at this angle, the light that is reflected from the surface is therefore perfectly polarized. The Fresnel equations predict that light with the p-polarization will not be reflected if the angle of incidence is $\theta_B = \arctan(n_1/n_0)$

Upon light reflection on a sample, p- and s-polarizations show different changes in amplitude and phase. In ellipsometry, therefore, the variation of light reflection with p- and s-polarizations is measured as the change in polarization state. As shown in Fig. A.2, ellipsometry measures the two values Ψ and Δ whose express the amplitude ratio and phase difference between p- and s-polarizations, respectively.

When the sample has a simple structure, the amplitude ratio Ψ is characterized by the refractive index n, while Δ represents light absorption described by the extinction coefficient k. In this case, the two values n and k can be determined directly from the two ellipsometry parameters Ψ and Δ obtained from a measurement by applying the Fresnel equations.

Still with reference to Fig. A.2, the amplitude reflection coefficients for the two polarization can be expressed as in [96] by Fresnel law [97]:

$$r_{\mathrm{p}} \equiv \frac{E_{\mathrm{rp}}}{E_{\mathrm{ip}}} = \frac{n_t \cos\theta_i - n_i \cos\theta_t}{n_t \cos\theta_i + n_i \cos\theta_t} \qquad r_{\mathrm{s}} \equiv \frac{E_{\mathrm{rs}}}{E_{\mathrm{is}}} = \frac{n_i \cos\theta_i - n_t \cos\theta_t}{n_i \cos\theta_i + n_t \cos\theta_t} \tag{A.2}$$

Those follow from the boundary condition, for the incident ($_i$), reflected ($_r$) and transmitted ($_t$), for $\mathbf{E}$ and $\mathbf{B}$ fields onto a sample surface, given by:

$$E_{\mathrm{ip}} \cos\theta_i - E_{\mathrm{rp}} \cos\theta_r = E_{\mathrm{tp}} \cos\theta_t \qquad \text{and} \qquad B_{\mathrm{ip}} + B_{\mathrm{rp}} = B_{\mathrm{tp}}$$

$$E_{\mathrm{is}} + E_{\mathrm{rs}} = E_{\mathrm{ts}} \qquad \text{and} \qquad -B_{\mathrm{is}} \cos\theta_i + B_{\mathrm{rs}} \cos\theta_r = -B_{\mathrm{ts}} \cos\theta_t$$

The relation in Eq. A.1 measured from ellipsometry and defined from the ratio of the amplitude reflection coefficients for p- and s-polarizations, can now be expressed, by using the definitions of Eq. A.2, as[2]:

$$\rho \equiv \tan\Psi \; e^{(i\Delta)} \equiv \frac{r_{\mathrm{p}}}{r_{\mathrm{s}}} \equiv \left(\frac{E_{\mathrm{rp}}}{E_{\mathrm{ip}}} \cdot \frac{E_{\mathrm{is}}}{E_{\mathrm{rs}}} \right) \tag{A.3}$$

In the case of Fig. A.2, Eq. A.3 can be simplified to $\rho = \tan\Psi \exp(\mathrm{i}\Delta) = E_{\mathrm{rp}}/E_{\mathrm{rs}}$, since $E_{\mathrm{ip}} = E_{\mathrm{is}}$. Hence, in the case of Fig. A.2, Ψ represents the angle determined from the amplitude ratio between reflected p- and s-polarization, while Δ expresses the phase difference between reflected p- and s-polarizations.

Analogously, if we measure light transmission instead of light reflection, Ψ and Δ can be defined as

$$\rho = \tan\Psi \exp(i\Delta) = \frac{t_{\mathrm{p}}}{t_{\mathrm{s}}} \tag{A.4}$$

[2] The above equations correspond to the ones when the definition of $N \equiv n - \mathrm{i}k$ is used. Consequently for $N \equiv n + \mathrm{i}k$, Eq. A.3 should be rewritten as $\rho = \tan\Psi \exp(-\mathrm{i}\Delta)$.

If we use polar coordinates to represent the amplitude reflection (or transmission) coefficients – i.e. to interpret light reflection in terms of variations in amplitude and phase (δ) – r_p and r_s could be rewritten as:

$$r_\mathrm{p} = |r_\mathrm{p}| \exp(i\delta_\mathrm{rp}) \qquad r_\mathrm{s} = |r_\mathrm{s}| \exp(i\delta_\mathrm{rs})$$

It follows that Eq. A.3 becomes:

$$\tan\Psi = \frac{|r_\mathrm{p}|}{|r_\mathrm{s}|} \qquad \text{and} \qquad \Delta = \delta_\mathrm{rp} - \delta_\mathrm{rs} \tag{A.5}$$

The reflectance R obtained in conventional measurements is defined by the ratio of the reflected light intensity (I_r) to incident light intensity (I_i). Since the light intensity of electromagnetic waves is proportional to the square of the electric field [96], the reflectances for p- and s-polarized waves are expressed by

$$R_\mathrm{p} \equiv \frac{I_\mathrm{rp}}{I_\mathrm{ip}} = \left|\frac{E_\mathrm{rp}}{E_\mathrm{ip}}\right|^2 = |r_\mathrm{p}|^2 \qquad \text{and} \qquad R_\mathrm{s} \equiv \frac{I_\mathrm{rs}}{I_\mathrm{is}} = \left|\frac{E_\mathrm{rs}}{E_\mathrm{is}}\right|^2 = |r_\mathrm{s}|^2 \tag{A.6}$$

Applying Eqs. A.6 in Eqs. A.5 it is easy to obtain the below expression for Ψ and Δ [93]:

$$\begin{aligned} \Psi = &\quad \tan^{-1}(|\rho|) = \tan^{-1}\left(|r_\mathrm{p}|/|r_\mathrm{s}|\right) = \tan^{-1}\left(\sqrt{R_\mathrm{p}/R_\mathrm{s}}\right) \\ \Delta = &\quad \arg(\rho) = \begin{cases} \tan^{-1}\left[\Im(\rho)/\Re(\rho)\right] & \text{if} \quad \Re(\rho) > 0 \\ \tan^{-1}\left[\Im(\rho)/\Re(\rho)\right] \pm 180^\circ & \text{if} \quad \Re(\rho) < 0 \quad \text{and} \quad \Im(\rho) \lesseqgtr 0 \end{cases} \end{aligned} \tag{A.7}$$

In order to complete the second half of Eq. A.1, let's neglect the complicated formula to show Ψ and Δ as functions of d, θ_0 and N_j (where $j = 1, 2, \ldots$ is the number of the considered layer), while it is more useful to express clearly $\rho = \rho(N_0, N_1, N_2, d, \theta_0)$.

From geometrical optics, let's remember the optical interference in a simplest example, ambient air/sample. In other words, it is assumed a sample composed of a substrate with infinite thickness only: f.i. looking at Fig. A.1, the layer with refractive index N_2 is completely negligible. In this case, remembering Fresnel equations for p- and s-polarized waves [97] and using Eqs. A.2 and A.3, we can express

$\rho = \tan\Psi \exp(\mathrm{i}\Delta)$ as below:

$$\rho = \frac{r_\mathrm{p}}{r_\mathrm{s}} = \left(\frac{N_1\cos\theta_0 - N_0\cos\theta_1}{N_1\cos\theta_0 + N_0\cos\theta_1}\right)\left(\frac{N_0\cos\theta_0 - N_1\cos\theta_1}{N_0\cos\theta_0 + N_1\cos\theta_1}\right)^{-1} \tag{A.8}$$

Substituting Eq. A.8 in Eqs. A.7 it is possible to explicit (Ψ, Δ) as functions of N_0, N_1, and θ_0 and of the measurable values R_p, R_s.

When a sample structure is simple, variations in Ψ and Δ can be attributed to changes in refractive index n and extinction coefficient k, respectively. In general, metals have a small n and a large k: thus, metals show very high reflectance [96, 98]. In particular, Ψ of metals generally becomes $\sim 45°$, independent of θ_0, since R_p is almost the same as R_s. However, Δ varies drastically versus θ_0 due to the continuous changes of δ_rp and δ_rs with θ_0 [98].

In the case of a bulk material, the equations derived for a single reflection can be directly inverted to provide the "pseudo" optical constants ($\langle n\rangle$ and $\langle k\rangle$) from the ellipsometry measurement. In fact it is possible to obtain the pseudo complex dielectric function $\langle\epsilon\rangle$ from [98]

$$\langle\epsilon\rangle = \sin^2\theta_0\left[1 + \tan^2\theta_0\left(\frac{1-\rho}{1+\rho}\right)^2\right] \tag{A.9}$$

Where the complex dielectric function is defined by the Kramers-Kronig relation and it is related the complex optical constant by:

$$\epsilon \equiv \varepsilon_1 - i\varepsilon_2 \qquad \text{such that } \epsilon = N^2 = (n - ik)^2$$

The term "pseudo" is due because Eq. A.9 assumes that there are no surface layers of any type. However, in any bulk material, typically there is a surface oxide or roughness, and the direct inversion would include these as part of the bulk optical constants.

Consider now a more difficult example, an ambient/thin film/substrate structure as reported in Fig. A.1. Eq. A.8 becomes more complicate and $\rho = \tan\Psi\exp(\mathrm{i}\Delta)$ can be expressed as in [96] by:

$$\rho = \frac{r_\mathrm{p}}{r_\mathrm{s}} = \left(\frac{r_{01,\mathrm{p}} + r_{12,\mathrm{p}}\exp(-i2\beta)}{1 + r_{01,\mathrm{p}}r_{12,\mathrm{p}}\exp(-i2\beta)}\right)\left(\frac{r_{01,\mathrm{s}} + r_{12,\mathrm{s}}\exp(-i2\beta)}{1 + r_{01,\mathrm{s}}r_{12,\mathrm{s}}\exp(-i2\beta)}\right)^{-1} \tag{A.10}$$

where β represents the so called film phase thickness, given by $\beta = 2\pi d N_1\cos\theta_1/\lambda$. From β definition even the layer thickness d is now a parameter and we can also exploit the effects due to the variation in incident wavelength λ. In the case of

transparent films, we obtain $N_1 = n_1$ since $k = 0$; thus nd product is generally called the optical thickness.

In Eq. A.10, 2β represents the phase shift of light traveling inside a thin film. When $2\beta = 2\pi$ the phase shift of a secondary beam becomes exactly one wavelength and the thickness period d_i in optical interference is expressed by $d_i = \lambda/2n_1 \cos\theta_1$. The conditions under which the phase shift between the primary and secondary beams becomes zero is:

$$\frac{2dn_1 \cos\theta_1}{\lambda} = m \ (m = 1, 2, 3..) \tag{A.11}$$

In spectral ellipsometry the changes in (Ψ, Δ) are observed in spectra in which the wavelength λ varies with a constant film thickness d. When the refractive index of a thin film (n_1) is known, the m minima in the interference fringes of $\Psi(\lambda)$ indicate the wavelengths (or the corresponding photon energies) whose satisfied Eq. A.11. Nevertheless, the evaluation of a refractive index from a known film thickness is rather difficult.

Until now we have just pointed out the optical rules necessary to link the ellipsometry parameters Ψ and Δ with the optical properties of simple structures: complex refractive index N, layer thickness d and reflectance R. In order to evaluate the optical constants and thickness of samples from spectroscopic ellipsometry, it is necessary to perform ellipsometry data analysis that consists of three major parts: dielectric function modeling, the construction of an optical model, and fitting to measured (Ψ, Δ) spectra.

The complexity and the vastness of this research argument cannot be sufficiently explained in a thesis appendix, it should require an own dissertation. Hence I prefer to remind to literature works (f.i. [94, 96, 98]-[100]) that treat deeply all the parts of an ellipsometry data analysis, while showing here only the Ψ and Δ data of the titanium/gold bilayer (as presented in Chap. 5.1), the optical model and the fit to estimate the refractive index and the extinction coefficient.

A.2 Instrument

The instrument available at INRIM institute is a Vertical Variable Angle Spectroscopic Ellipsometry (V-VASE) produced by J.A. Woollam Co., Inc. The V-VASE (picture of Fig. A.3) covers a wavelength range from 250 nm to 1700 nm and incident angle range from 15° to 90°: it is not possible to observe the back reflection because the minimum angle is limited to 15°, but in case of transparent structure the instrument is able for transmission measurements with beam orthogonal to the

sample surface (90° angle). The beam spot is about 1.8 mm of diameter or can be focused in 200 μm.

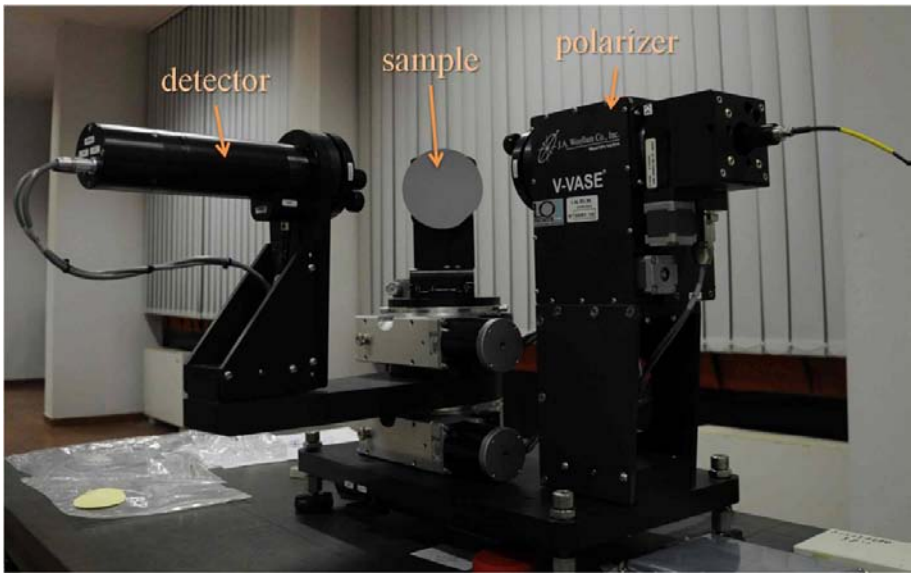

Figure A.3. V-VASE picture: the polarization generator, the sample and detector branch are indicated.

The primary tools for collecting ellipsometry data include the light source, the polarization generator, the sample holder, the polarization analyzer, and the detector [101]. The light source is a monochromator with three different gratings to select the wavelength. The polarization generator and analyzer are built with optical components that manipulate the polarization: polarizers, compensators, and phase modulators. Common ellipsometer configurations include rotating analyzer (RAE), rotating polarizer (RPE), rotating compensator (RCE), and phase modulation (PME). The RAE configuration is shown in Fig. A.4.

A light source produces unpolarized light which is then sent through a polarizer. The polarizer allows light of selected electric field orientation to pass. The polarizer axis is oriented between the p- and s- planes (the incident plane and the one parallel to the sample surface), such that both polarization components arrive to the sample surface.
The linearly polarized light reflects from the sample surface and becomes elliptically polarized. The wave travels through a continuously rotating polarizer and presents in the detector branch. The amount of light allowed to pass depends on the polarizer orientation relative to the elliptic electric field coming from the sample.
The detector converts light intensity to electronic signal to determine the reflected

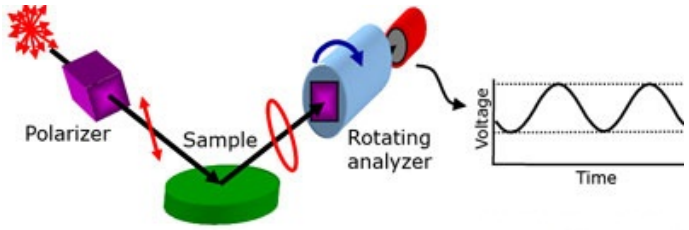

Figure A.4. Rotating analyzer ellipsometer configuration uses a polarizer to define the incoming polarization and a rotating polarizer after the sample to analyze the outgoing light. The detector converts light to a voltage whose dependence yields the measurement of the reflected polarization [101].

polarization. This information is compared to the known input polarization to evaluate the polarization change caused by the sample reflection. This is the ellipsometry measurement of Ψ and Δ.

A.3 Optical Constants of TES film.

With reference to Chap. 5.1, the same film used to produce TES detector has been investigated by the V-VASE, to extract the optical constants and the reflectance of the bilayer. Fig. A.5 reports Ψ and Δ measurements of Ti/Au/Ti film deposited on SiN substrate structured as in Fig. 5.1.

The measurement are performed under the incidence angle of 60°, 65°, 70°, around the Brewster angle. Fig. A.5 reports data only for two angles since the similar behavior of the other one. The spectroellipsometric data for the three incidence angles are fitted simultaneously taking in consideration the model of layer's structure of Tab. A.1.

#	material	thickness
4	TiO_2	(6 ± 3) nm
3	Ti	(31 ± 5) nm
2	Au	(42 ± 4) nm
1	Ti	(5 ± 3) nm
0	substrate	0.5 mm

Table A.1. Model of the TES film structure and layer thicknesses obtained by fit parameters.

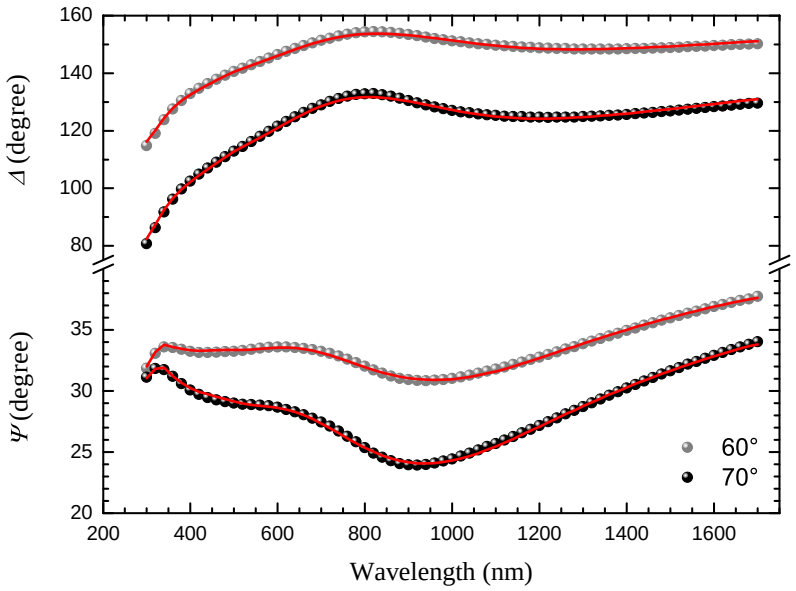

Figure A.5. Ψ and Δ measurements (dots) of Ti/Au film, at incidence angles of 60° and 70°, into the wavelength range 250 nm – 1700 nm. The data fits (red lines) are also reported.

The thickness values of Tab. A.1 are obtained fitting measured data with opportune optical models corresponding to the structures we were analyzing. We proceeded in four steps following the fabrication process. In the first one, only the SiN substrate has been characterized, starting from Si literature data [102] and building an opportune model to describe the double polished Si wafers covered on both sides by 500 nm thick SiN layer.
In the second step, we have considered the thin Ti film over the substrate; then, the thicker gold layer over the thinner titanium. In the last one the complete structure (Ti/Au/Ti) has been measured, finding a natural oxide layer over the top Ti.

In all the steps, the quasi-free fit parameters were the thicknesses of the considered layers and their optical constants. The term "quasi" means that for the thickness we had an estimation of the value from the fabrication process, while for the optical constants we started from literature data [103] of the considered material: for titanium layers we used the polycrystalline form.

The uncertainties over those values are provided by the analysis software [101]; we notice that for layer number 1 and 4 the relative uncertainties suffer the thin depth to estimate.

The optical constant n and the extinction coefficient k obtained by the fit on spectroellipsometric data, of the TES film with optical model given in Tab. A.1, are shown in Fig. A.6. These values differ from literature data of polycrystalline

titanium, due to the thin film fabrication process.

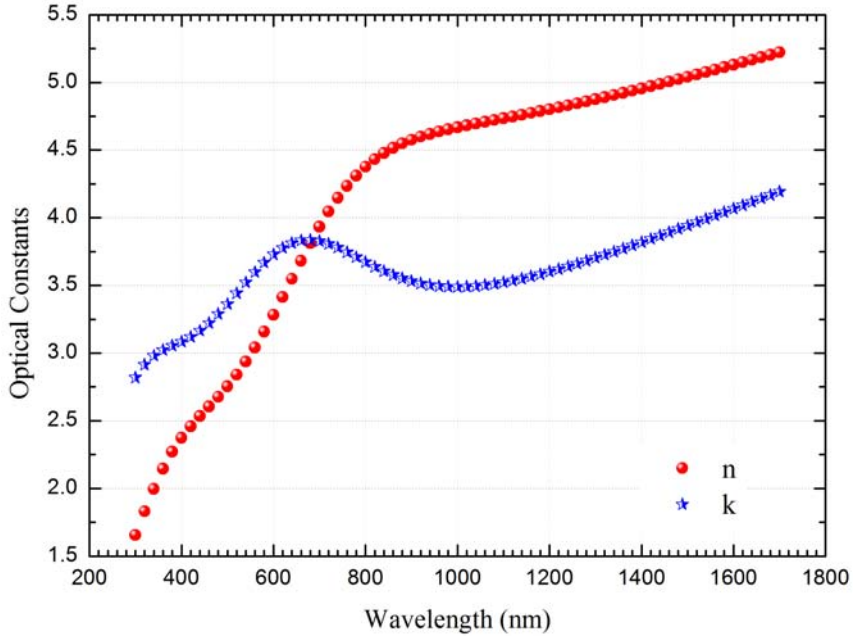

Figure A.6. Optical constant n (dots in red) and the extinction coefficient k (stars in blue) of a TES film.

From the optical model of Tab. A.1, the ellipsometer software is able to extrapolate the reflectance of the TES film for incidence beam orthogonal to the sample surface: the result is shown in Fig. A.7. In the telecom wavelengths range, comparing these reflectance values with TES detection efficiency estimations, results that the reflectance is higher than for high T_c devices (Chap. 7.2), while it is in agreement with low T_c detectors (Chap. 6.3). An explanation could be that the film analyzed by the ellipsometer was fabricated in parallel with low T_c TESs and we did not expect a different behavior due to fabrication process; while for the high T_c TESs the film thicknesses are different.

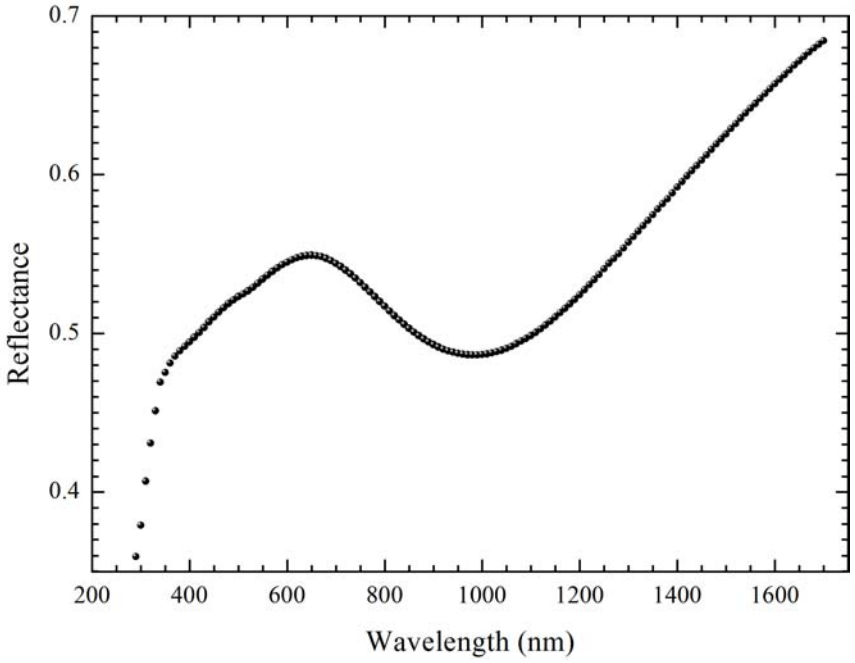

Figure A.7. Extrapolation of TES reflectance, from the optical model, for orthogonal incidence beam.

Bibliography

[1] 16e CGPM *Comptes Rendus* (1979).

[2] T.J. Quinn, "Redefinition of the kilogram, ampere, kelvin and mole: a proposed approach to implementing CIPM recommendation 1 (CI-2005)'', *Metrologia*, vol. 31 (1995), p. 515–527.

[3] I.M. Mills et al, "Redefinition of the kilogram, ampere, kelvin and mole: a proposed approach to implementing CIPM recommendation 1 (CI-2005)", *Metrologia*, vol. 43 (2006), p. 227–246.

[4] J.C. Zwinkels et al, "Photometry, radiometry and 'the candela': evolution in the classical and quantum world", *Metrologia*, vol. 47 (2010), p. R15–R32.

[5] S. Scheel, "Single-photon sources–an introduction", *J Mod Optic*, vol. 56, n. 2-3 (2009), p. 141–160.

[6] www.quantumcandela.org

[7] M.L. Rastello, "Candela: Towards quantum-based photon standards", *final publishable JRP report*, T1-J2.3 (2011).

[8] J. Geist et al, "Prospects for improving the accuracy of silicon photodiode self-calibration with custom cryogenic photodiodes'', *Metrologia*, vol. 40 (2003), p. 132–135.

[9] R.H. Hadfield, "Single-photon detectors for optical quantum information applications", *Nature Photonics*, vol. 3 (2009), p. 696–705.

[10] P. Colling et al, "Low energy X-ray detection in cryogenic detectors with tungsten thermometers'', *Nucl Instrum Meth A*, vol. 354 (1995), p. 408–416.

[11] K.D. Irwin et al, "A self-biasing cryogenic particle detector utilizing electrothermal feedback and a SQUID readout'', *IEEE Trans Appl Supercond*, vol. 5 (1995), p. 2690–2693.

[12] K.D. Irwin et al, "X-ray detection using a superconducting transition-edge sensor microcalorimeter with electrothermal feedback", *Appl Phys Lett*, vol. 69 (1996), p. 1945–1947.

[13] D. A. Wollman et al, "High resolution, energy-dispersive microcalorimeter spectrometer for x-ray microanalysis", *J Microsc*, vol. 188 (1997), p. 196–223.

[14] B. Cabrera et al, "Detection of single infrared, optical, and ultraviolet photons using superconducting transition edge sensor", *Appl Phys Lett*, vol. 73 (1998),

p. 735–737.

[15] R.W. Romani et al, "First Astronomical Application of a Cryogenic TES Spectrophotometer", *Appl Phys Lett*, vol. 521 (1999), p. 153–156.

[16] M.P. Bruijn et al, "Development of an array of transition edge sensors for application in X-ray astronomy", *Nucl Instrum Meth A*, vol. 520 (2004), p. 443–445.

[17] D. Rosenberg et al, "Low-temperature optical photon detectors for quantum information applications", *Phys Rev Lett*, vol. 98 (2007), p. 010503.

[18] A.E. Lita et al, "Counting near-infrared single-photons with 95% efficiency", *Opt Express*, vol. 16 (2008), p. 3032–3040.

[19] A.E. Lita et al, "High-Efficiency Photon-Number-Resolving Detectors based on Hafnium Transition-Edge Sensors'', *AIP Conf Proc*, vol. 1185 (2009), p. 351-354.

[20] D. Fukuda et al, "Titanium superconducting photon-number-resolving detector", *IEEE Trans Appl Supercond*, vol. 21, n. 3 (2011), p. 241–245.

[21] L. Lolli et al, "Ti/Au TES to discriminate single photons'', *J Low Temp Phys*, (2012) DOI: 10.1007/s10909-012-0473-2.

[22] E.L. Dereniak & D. Crowe, *Optical Radiation Detector*, Wiley, New York (1984); W. Becker, "Advanced time-correlated single photon counting techniques", *Springer*, Chap. 2 (2005).

[23] M.A. Nielsen & I.L. Chuang, "Quantum computation and quantum information", *Cambridge Univ Press* Chap. 1 (2000).

[24] A. Kuhn et al, "Deterministic Single-Photon Source for Distributed Quantum", *Phys Rev Lett*, vol. 89, n. 6 (2002) p. 067901.

[25] R. Lettow et al, "Realization of two Fourier-limited solid-state single-photon sources", *Opt Express*, vol. 15 (2007), p. 15842.

[26] T. Gaebel et al, "Stable single-photon source in the near infrared", *New J Phys*, vol. 6 (2004),p. 98–105.

[27] W. Schmunk et al, "Photon Number Statistics of NV-Centre Emission", *Metrologia* [accepted to] (2012).

[28] Z.L. Yuan et al, "Electrically Driven Single-Photon Source'', *Science*, vol. 295, n. 5552 (2002), p. 102–105.

[29] C.K. Hong & L. Mandel, "Experimental realization of a localized one-photon state'', *Phys Rev Lett*, vol. 56 (1986), p. 58–60.

[30] P.R. Norton, "Handbook of optics", *McGraw-Hill, Inc*, ed. M. Bass (1995), Chap. 15.

[31] C. Silberhorn, "Detecting quantum light", *Contemp Phys*, vol. 48 (2007), p. 143-156.

[32] J. Cheung et. al, "Single-photon sources, detectors, applications and measurement methods", *J Mod Opt*, vol. 56 (2009), p. 139–140.

[33] T. Peacock et al, "Recent developments in superconducting tunnel junctions for ultraviolet, optical & near infrared astronomy'', *Astron Astrophys, Suppl Ser*, vol. 127 (1998), p. 497.

[34] J. Baselmans, "Kinetic Inductance Detectors'', *J Low Temp Phys*, (2012) DOI: 10.1007/s10909-011-0448-8; P.K. Day et al, "A broadband superconducting detector suitable for use in large arrays'', *Nature*, vol. 425, n. 6960 (2003), p. 817–821.

[35] M.D. Eisaman et al, "Invited Review Article: Single-photon sources and detectors'', *Rev Sci Instrum*, vol. 82 (2011), p. 071101.

[36] K.D. Irwin & G.C. Hilton, "Cryogenic Particle Detection", *Springer Topics in Applied Physics*, ed. C. Enss, vol. 99 (2005), Chap. 3.

[37] http://jp.hamamatsu.com/; http://www.burle.com/index.html

[38] H. Kume et al, "Ultrafast microchannel plate photomultipliers", *Appl Opt*, vol. 27 (1998), p. 1170–1178.

[39] J. Blazej, "Photon number resolving in Geiger mode avalanche photodiode photon counters", *J Mod Opt*, vol. 51 (2004), p. 1491–1498.

[40] L.A. Jiang et al, "Photon-number-resolving detector with 10 bits of resolution" *Phys Rev A*, vol. 75 (2007), p. 062325.

[41] D. Achilles et al, "Fiber-detection with photon-number resolution", *Opt Lett*, vol. 28 (2003), p. 2387–2389.

[42] A.P. Vandevender, "High efficiency single-photon detection via frequency up-conversion", *J Mod Opt*, vol. 51 (2004), p. 1433–1445.

[43] H. Takesue et al, "Differential phase shift quantum key distribution experiment over 105 km fibre", *New J Phys*, vol. 7 (2005)p. 232–243.

[44] J. Kim et al, "Multiphoton detection using visible light photon counter", *Appl Phys Lett*, vol. 74 (1999), p. 902–904.

[45] G.N. Gol'tsman et al, "Picosecond superconducting single-photon optical detector", *Appl Phys Lett*, vol. 79 (2001), p. 705–707.

[46] E.A. Dauler et al, "Photon-number-resolution with sub-30-ps timing using multi-element superconducting nanowire single photon detectors", *J Mod Opt*, vol. 56 (2009), p. 364–373.

[47] H.W. Li et al, "Quantum dot resonant tunneling diode for telecommunication wavelength single photon detection", *Appl Phys Lett*, vol. 91 (2007), p. 073516.

[48] E.J. Gansen et al, "Photon-number-discriminating detection using a quantum-dot, optically gated, field-effect transistor", *Nature Photon*, vol. 1 (2007), p. 585–588.

[49] B.E. Kardinal et al, "Photon number resolving detector based on a quantum dot field effect transistor", *Appl Phys Lett* vol. 90 (2007), p. 181114.

[50] A. Peacock et al, "Single optical photon detection with a superconducting tunnel junction'', *Nature*, vol. 381 (1996), p. 135–137.

[51] R.A. Hijmering et al, "Direct position resolution measurement with droids at optical wavelengths,'', *J Low Temp Phys*, vol. 151 (2008), p. 298–303.
[52] D.C. Mattis & J. Bardeen, "Theory of the anomalous skin effect in normal and superconducting metals'', *Phys Rev*, vol. 111 (1958), p. 412–417.
[53] B.A. Mazin, "A superconducting focal plane array for ultraviolet, optical, and near-infrared astrophysics'', *Optics Express*, vol. 20, n. 2 (2012), p. 1503–1511.
[54] E. Figueroa Feliciano, "Theory and development of position-sensitive quantum calorimeters'', *Stanford University Ph.D. Thesis*, Stanford (2001).
[55] M. Galeazzi, "An external electronic feedback system applied to a cryogenic microcalorimeter", *Rev Sci Instrum*, vol. 69 (1998), p. 2017–2023.
[56] K.D. Irwin, "An application of electrothermal feedback for high resolution cryogenic particle detection", *Appl Phys Lett*, vol. 65, n. 15 (1995), p. 1998–2000.
[57] O. Meier et al, "Active thermal feedback for massive cryogenic detectors", *Nucl Inst & Meth A*, vol. 444 (2000), p. 350–352.
[58] J.R. Hook and H.E. Hall, "Solid State Physics", *John Wiley & Sons Ltd*, second edition (1994).
[59] K.D. Irwin, "Phonon-Mediated particle detection using superconducting Transition-Edge Sensors", *Stanford University Ph.D. Thesis*, Stanford (1995).
[60] S. Nam, "Development of Phonon-Mediated cryogenic particle detectors with electron and nuclear recoil discrimination", *Stanford University Ph.D. Thesis*, Stanford (1998).
[61] A.J. Miller, "Development of a broadband optical spectrophotometer using superconducting Transition-Edge sensors", *Stanford University Ph.D. Thesis*, Stanford (2001).
[62] W.S. Boyle & K.F. Rodgers, "Performance characteristics of a new low-temperature bolometer", *J Opt Soc Am*, vol. 49 (1959), p. 66.
[63] E. Taralli et al, "Impedance measurements on a fast transition-edge sensor for optical and near infrared range", *Trans Appl Supercond*, vol. 21, n. 10 (2010).
[64] E. Taralli et al, "Impedance measurements for near infrared-optical Ti/Pd and Ti/Au Transition-Edge Sensors", *Eur Phys J Plus*, vol. 127, n. 2 (2012).
[65] L. Lolli et al, "Operation of a MINIDIL OD70 -30 mK Dilution Refrigerator", *Technical Report n. 5/2010*, INRIM, Torino, 2010.
[66] E. Taralli, "Transition-Edge Sensor characterization for the development of single photon detectors", *Politecnico di Torino Ph. D. Thesis*, Dept. of Physics, Torino (2006).
[67] L. Lolli et al, "Ti/Au Transition Edge Sensors Coupled to Single Mode Optical Fibers Aligned by Si V-Groove", *IEEE Trans Appl Supercond*, vol. 23 (2011), p. 215–218.
[68] www.ozoptics.com.
[69] www.epotek.com/ssedocs/datasheets/H20E.PDF.

[70] E. Taralli et al, "Optical bench for multiple optical fibers coupling to light detectors", *Technical Report n. 6/2010*, INRIM, Torino, 2010.
[71] D. Marcuse, "Gaussian approximation of fundamental modes of graded fibers", *J Opt Soc Am*, vol. 68, (1978), p. 103–109.
[72] J.C. Gallop, "SQUIDs, the Josephson Effects and Superconducting Electronics", *Adam Hilger* (1991).
[73] D. Drung et al, "Highly Sensitive and Easy-to-Use SQUID Sensors", *IEEE Trans Appl Supercond*, vol. 17, n. 2 (2007), p. 699–704.
[74] D. Drung, "High-T_c and low-T_c dc-SQUID electronics", *Supercond Sci Technol*, vol. 16 (2008), p. 1320-1336.
[75] "High performance dc SQUID Electronics", *Magnicom GbR handbook*
[76] C. Portesi et al, "Fabrication of Au/Ti TESs for Optical Photon Counting", *J Low Temp Phys*, vol. 151, n. 1–2 (2008), p. 261–265.
[77] L. Lolli, "Ti/Au TES as photon-number resolving detector", *Il Nuovo Cimento C*, vol. 34, n. 5 (2011) p. 209–214.
[78] D. Alberto, "Digital Signal Processing applied to Physical Signals", *Cern-Thesis-2011-008*, Politecnico di Torino, Torino (2011).
[79] L. Lolli et al, "Ti/Au TES as superconducting detector for Quantum Technologies", *Int J Quantum Inf*, vol. 9, n. 1 (2011), p. 405–413.
[80] T.J. Bay, "Advanced in the optical imaging Transition-Edge Sensor array", *Stanford University Ph.D. Thesis*, Dept. of Physics, Stanford (2007).
[81] G. Brida et al, "Full quantum characterization of superconducting photon counters", http://arxiv.org/abs/1103.2991 (2011).
[82] D. Alberto et al, "Optical Transition-Edge Sensors Single Photon Pulse Analysis", *IEEE Trans Appl Supercond*, vol. 21 (2011), p. 285–288.
[83] K. Nakamura et al, "Review of particle physics", *J Phys G*, vol. 37, n. 075021 (2010).
[84] M. Rajteri et al, "Photon-number discriminating superconducting transition-edge sensor", *Metrologia*, vol. 46 (2009), p. S283–S287.
[85] A. Avella et al, "Self consistent, absolute calibration technique for photon number resolving detectors", *Optics Express*, vol. 19, n. 23 (2011), p. 23249–23257.
[86] M. Rajteri et al, "How to avoid reflection losses in superconducting light source", *J Mod Optic*, vol. 56, n.2–3 (2009), p. 385–389
[87] A.G. Kozorezov et al, "Resolution limitation in superconducting transition edge photon detectors due to downconversion phonon noise", *Appl Phys Lett*, vol. 89, n. 22 (2006), p. 223510-1–3.
[88] G. Brida et al, "Twin-photon techniques for photo-detector calibration", *Laser Physics Lett*, vol. 3 (2006), p. 115–123 and ref.s therein.
[89] S.V. Polyakov and A.L. Migdall, "High accuracy verification of a correlated-photon-based method for determining photoncounting detection efficiency",

Opt Express, vol. 15 (2007), p. 1390–1407.

[90] F. Pobell, "Matter and Methods at low temperatures", *Springer-Verlag Berlin*, Chap. 3 (1992).

[91] L. Risegari & G. Ventura, "The Art of Cryogenics", *Elsevier* Chapters 5 & 7, (2007).

[92] M. Wakaki et al, "Physical Properties and Data of Optical Materials", CRC Press, Taylor & Francis Group (2007).

[93] R.M.A. Azzam & N.M. Bashara, "Ellipsometry and Polarized Light'', *North-Holland*, Amsterdam (1977).

[94] H.G. Tompkins & E.A. Irene, "Handbook of Ellipsometry'', *William Andrew, Inc* Norwich (2005).

[95] D. Brewster, "Treatise on Optics'', *Longman, Rees, Orme, Brown, Green, & Taylor*, London (1831), p. 108.

[96] H. Fujiwara, "Spectroscopic Ellipsometry: Principles and Applications'', *John Wiley & Sons, Ltd*, New York (2007).

[97] E. Hecht, "Optics'', *Addison Wesley*, San Francisco (2002).

[98] H.G. Tompkins, "WVase32 Software Training Manual'', *J.A. Wollam Co, Inc*, (2006).

[99] H.G. Tompkins & W.A. McGahan, "Spectroscopic Ellipsometry and Reflectometry: A User's Guide'', *John Wiley & Sons, Ltd*, New York (1993).

[100] M. Schubert, "Infrared Ellipsometry on Semiconductor Layer Structures: Phonons, Plasmons and Polaritons'', *Springer*, Heidelberg (2004).

[101] "Guide to Using WVase32'', *J.A. Wollam Co, Inc*, (2008).

[102] C.M. Herzinger et al, "Ellipsometric determination of optical constants for silicon and thermally grown silicon dioxide via a multi-sample, multi-wavelength, multi-angle investigation", *J Appl Phys*, vol. 83, n. 6 (1998), p. 3323–3336.

[103] E.D. Palik, "Handbook of Optical Constants of Solids", *Academic Press*, San Diego (1998).